Cal Poly

Caltech

SCEC
AN NSF+USGS CENTER

UC Irvine

UCLA

UC Santa Barbara

USC

Regional Analysis of Spatially Distributed Ground Failure Displacement Hazards in California

Jonathan P. Stewart
University of California, Los Angeles

Domniki Asimaki and Grigorios Lavrentiadis
California Institute of Technology, Pasadena, CA

Ellen M. Rathje and Olaide Ojomo
University of Texas, Austin

Pengfei Wang*
Old Dominion University, Norfolk, VA

Paolo Zimmaro*
University of Calabria, Italy

*Formerly University of California Los Angeles

A report on research conducted with support from the California Energy Commission, Pacific Gas and Electric Company, and California Department of Transportation

Report GIRS-2023-03

DOI: 10.34948/N3V88J

University of California, Los Angeles (headquarters)

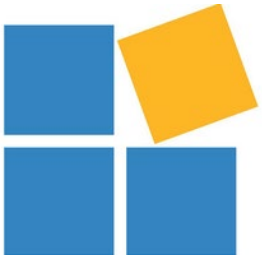

Natural Hazards Risk & Resiliency Research Center

B. John Garrick Institute for the Risk Sciences

Regional Analysis of Spatially Distributed Ground Failure Displacement Hazards in California

Jonathan P. Stewart (UCLA)

Domniki Asimaki (Caltech)

Ellen M. Rathje (University of Texas)

Grigorios Lavrentiadis (Caltech)

Olaide Ojomo (University of Texas)

Pengfei Wang (Old Dominion University)

Paolo Zimmaro (University of Calabria, Italy)

A report on research conducted with support from the California Energy Commission, Pacific Gas & Electric Company, and California Department of Transportation.

Report GIRS-2023-03

DOI: 10.34948/N3V88J

Natural Hazards Risk and Resiliency Research Center

B. John Garrick Institute for the Risk Sciences

University of California, Los Angeles (Headquarters)

August 2023

Table of Contents

Abstract

Seismic risk for spatially distributed infrastructure is driven mainly by ground failure, defined as permanent ground displacements from mechanisms such as landslides, liquefaction, and seismic compression. Most forms of ground failure are a consequence of soil responses to ground shaking, which should be evaluated on a hazard-consistent scenario basis to represent spatial correlations of intensity measures. A companion report describes a methodology for identifying hazard-consistent event scenarios.

Seismic ground failure responses are evaluated based on regionally-accessible information on geology, groundwater hydrology, and terrain. Given these inputs, liquefaction and landslide displacements are predicted point-by-point on a 10 m grid using customized analysis procedures and logic trees for each ground failure type. For each point, these analyses provide probabilities that the hazard exists, probabilistic distributions (accounting for epistemic uncertainties) of related displacements, and displacement directions (azimuths). Series of points expected to move together (e.g., in a single lateral spread) are grouped into polygons. Ground failure features (landslides, lateral spreads) of varying sizes may occur within these polygons. The output of these analyses are feature locations, sizes, displacement amounts, and displacement azimuths, which can be applied in subsequent fragility and risk analysis of distributed infrastructure systems.

The report presents the data considered in the regional geo-hazards assessments, the methodologies for liquefaction and landslide displacements analyses and the grouping thereof into polygons, and the results of these analyses for an example region in southern California for scenario events.

Acknowledgments

Support for this research project was provided by the California Energy Commission, Pacific Gas & Electric Company, and California Department of Transportation. The support of these organizations is greatly appreciated.

The opinions, findings, conclusions, or recommendations expressed in this publication are those of the authors and do not necessarily reflect the views of the study sponsors, the Natural Hazards Risk and Resiliency Research Center, or the Regents of the University of California.

1 Introduction

1.1 Project Overview

Seismic ground failure from liquefaction, landslides, and related phenomena are substantial sources of earthquake hazards to people and infrastructure. Procedures for the assessment of these hazards [e.g., Youd et al. 2001, Blake et al. 2002] are largely derived for application to individual sites, such as a building where seismic design is to be performed. As such, these procedures are conditioned on relevant geotechnical parameters as would be derived from a site-specific geotechnical investigation (i.e., soil stratigraphy, ground water level, penetration resistance, shear strength, etc.). Moreover, the ground motions used with these procedures are typically derived from location-specific probabilistic seismic hazard analyses.

Studies of seismic risk to distributed infrastructure systems challenge the traditional paradigm for ground failure analysis in two key respects: (1) the infrastructure can occur across a large spatial domain, potentially involving many different geological and terrain conditions associated with different types and levels of ground failure hazards; (2) seismic ground motion hazards derived for a single site, or for a collection of sizes along the system at a consistent hazard level, fail to accurately describe the distribution of shaking demands that the distributed infrastructure systems may experience. This report describes analysis procedures developed to address the first of these issues and presents results for an example region in southern California. The focus here is on two specific forms of seismic ground failure – seismically-induced landslides and liquefaction-induced settlement and lateral spreading. The second issue above was addressed in contemporaneous research and is described in a companion report [Wang et al. 2023].

The specific application for which the present work was performed is natural gas storage and distribution infrastructure in California (Figure 1.1). The authors are part of a larger team developing a tool to evaluate the risk to this infrastructure system from earthquake hazards. This tool will have modules that characterize various hazards, infrastructure component fragilities, and system level risk.

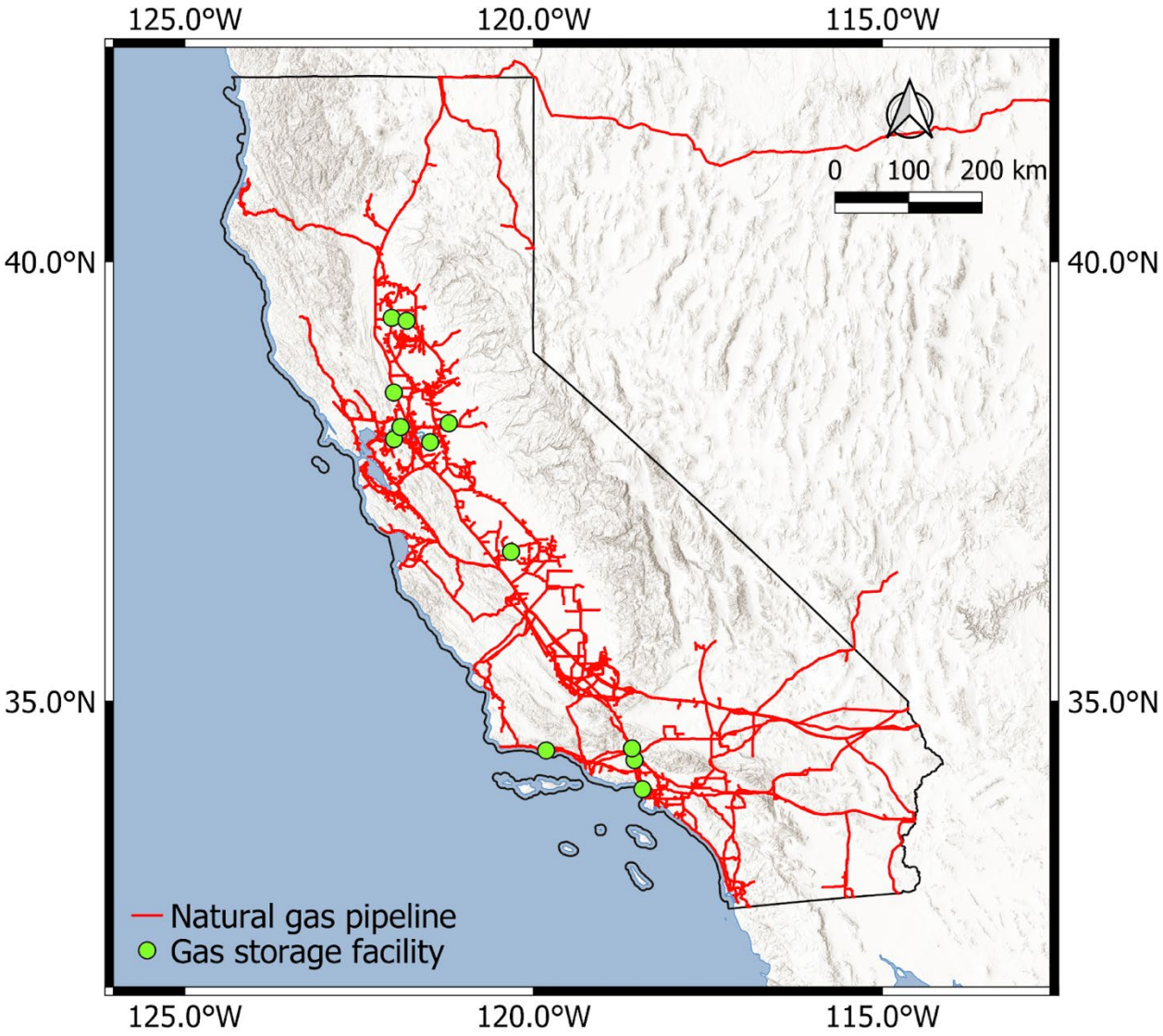

Figure 1.1. Natural gas pipelines and gas storage facilities from the California Geological Survey (CGS) within the State of California.

1.2 Overview of Analysis Framework

The proposed analysis framework takes as input the following information:

1. Scenario ground motions with realistic spatial distributions of ground shaking that are consistent with one or more relevant ground motion hazard levels [Wang et al. 2023].
2. Regional information on surface geology that is mapped in a consistent manner across the study area, which in the present case is the entire State of California. We use geologic maps prepared by the California Geological Survey [Wills et al. 2015].

3. Information on ground water depth from a global model [Fan et al. 2013], updated based on local well data [California Water Board, 2020].
4. Digital elevation models at 10 m horizontal resolution, as provided by the USGS [2018].

Liquefaction and landslide displacement estimates conditioned on the above information carry large epistemic uncertainties because the information on site conditions (from 2-4) does not directly provide the information required to assess these ground failure hazards. Instead, we estimate the relevant soil properties from applicable databases conditioned on location-specific surface geology; the uncertainties associated with these soil property estimates are referred to as parametric. Moreover, once applicable ranges of those properties are defined, alternate methods of analysis can be applied, which is a separate source of epistemic uncertainty known as modeling uncertainty. These uncertainties are considered using logic tree frameworks, as described in Chapters 3 and 4.

The direct outcomes of both the landslide and liquefaction models are attributes of displacements for a particular ground motion scenario on a 10 m grid spacing, as schematically illustrated in Figure 1.2. At each grid point, the following information is provided:

1. Probability that ground failure from a particular mechanism (landslide or liquefaction) occurs; in the landslide case, this is taken as the probability that a certain displacement level is exceeded, whereas for liquefaction, it is the probability of both liquefaction-susceptible soils being present and liquefaction triggering having occurred;
2. If the ground failure hazard exists, a distribution of displacement levels is provided such that a conditional probability density function can be derived;
3. Azimuth of displacement, which is generally taken as the horizontal direction of maximum slope from the 10 m digital elevation model.

As shown in Figure 1.2, grid-point displacements are grouped into polygons. This grouping takes into account geomorphic features of the area as described in Chapter 3 and 4. Within the polygons, individual ground failure features (i.e., landslides or lateral spreads) of varying sizes may occur, which are estimated using empirical models. Additionally, ranges of displacement amounts and azimuths may occur within the polygons that are broader than those from (2-3) above. Within the context of the present gas infrastructure risk study, the information provided for subsequent fragility analyses are polygon locations, distributions of feature sizes within polygons, and displacement amounts and directions within polygons. As described in Chapters 3-4, in the development of the logic trees, checks are made to ensure that the cumulative sizes of features relative to the overall area of study regions are consistent with observed rates of ground failure in past earthquakes.

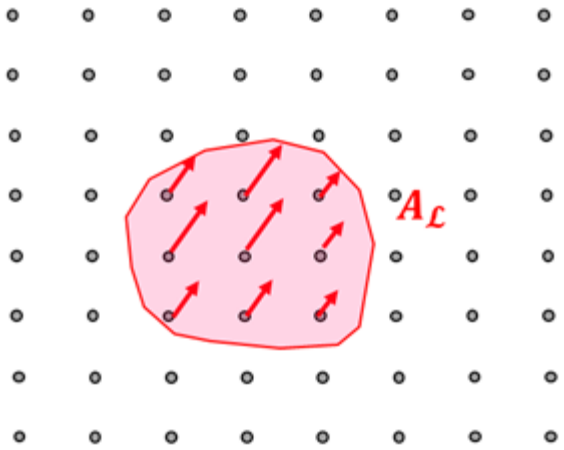

Figure 1.2. Schematic showing grid locations where displacements are computed. Arrows at grid points indicate displacement amounts and azimuths, which are uncertain (i.e., the amount depicted would represent a particular percentile as derived from logic tree analyses). The polygon depicted by the area marked as A_L indicates a zone where landslides or lateral spreads of varying sizes may occur.

1.3 Organization of Report

Following this introduction, Chapter 2 presents the data sources considered in our regional geo-hazards analyses. Chapters 3 and 4 present the framework for the analysis of probabilities of ground failure at grid points, displacement amounts at grid points and their uncertainties, and grouping of computed displacements into polygons for the purpose of providing displacement features that are reasonably consistent with empirical models in terms of their sizes and pervasiveness. Chapter 5 presents example results.

2 Statewide Data Sources

Analyses and models presented in this report rely upon State-wide resources and databases. Our compilation of such resources includes published information and data available from the California Geologic Survey (CGS) upon request. There are three main categories of information: (1) geology maps, (2) digital elevation models, (3) groundwater, (4) cone penetration test (CPT) soundings, and (5) shear strength data from laboratory tests.

2.1 Geology Maps

This project uses the statewide geologic map developed by Wills et al. (2015) to assign regional-scale geotechnical parameters (e.g., shear strength for landslides) to each geologic unit in California as described in Chapters 3 and 4. This map defines various bedrock units and Quaternary sediments based on age and depositional environment (e.g., separating alluvial fans from lake/marine deposits into fifteen geologic units across the state as shown in Figure 2.1. This map provides a consistent representation of the spatial distribution of geologic units at a scale of 1:1,500,000. Although developed to assign values of shear wave velocity (Vs30) state-wide, the geologic groupings are also considered appropriate for assigning other geotechnical parameters.

Although the Wills et al. (2015) map provides a consistent geologic representation across the state, there are regional differences between Northern and Southern California with respect to the shear strength characterization within the different geologic units. While the boundary between the two regions is not well defined, this study utilizes the boundary marked at the base of Coast Ranges, Sierra Nevada and Basin and Range in Figure 2.2 for strength assignment purposes.

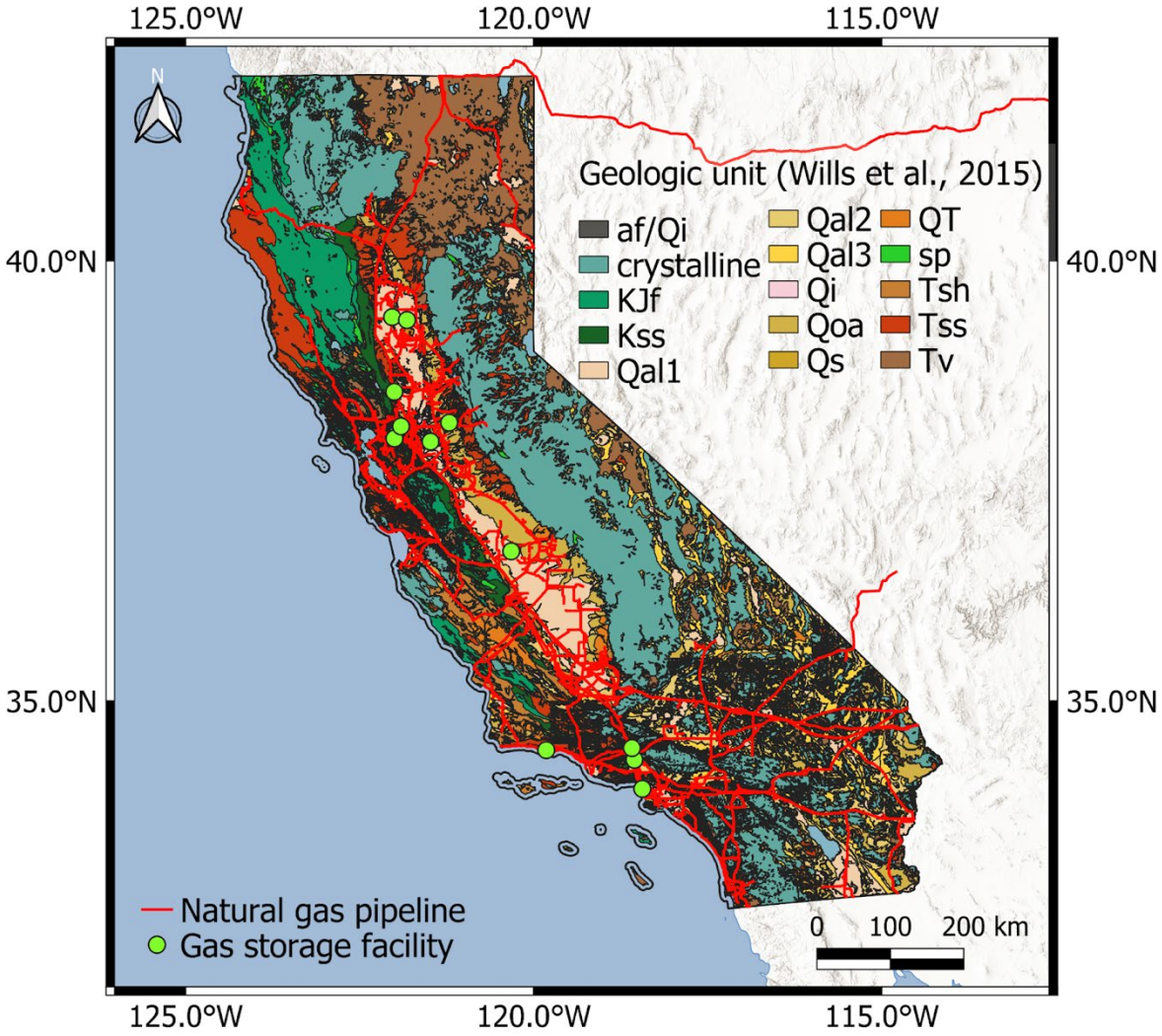

Figure 2.1. Geologic units from Wills et al. (2015), along with natural gas pipelines, and gas storage facilities within California (adapted from Zimmaro et al., 2021).

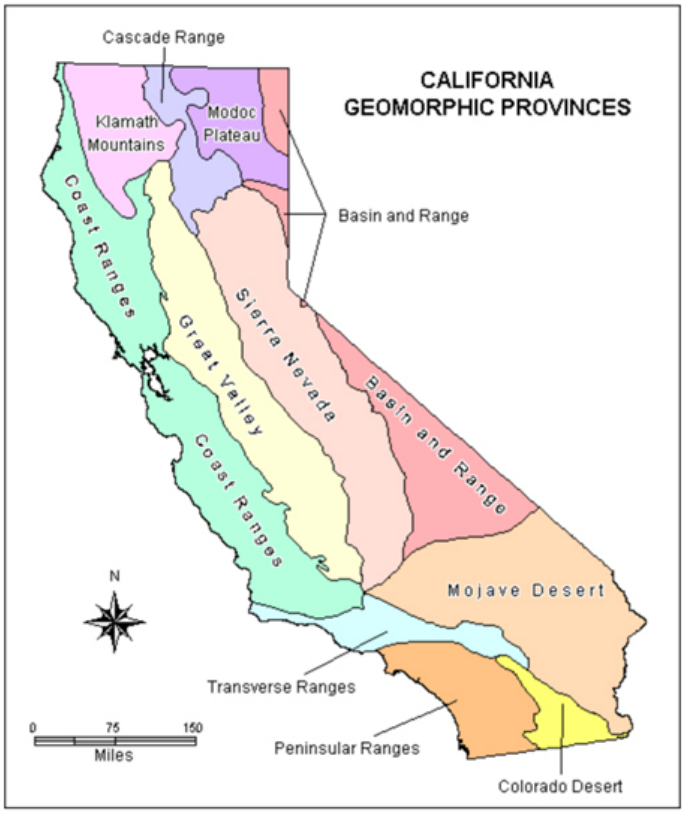

Figure 2.2. Geomorphic provinces of California (https://www.conservation.ca.gov/cgs/california-geotour)

Because landslides are not expected to occur on flat slopes, the scope of this study is limited to only 10 of the 15 units defined by Wills et al. (2015) that comprise areas with slopes steeper than 10°. These units are the older alluvium units associated with relatively steeper slopes (Qal3, Qoa and QT), Tertiary units (Tsh, Tss, Tv), Cretaceous units (sp, Kss, KJf), and crystalline units (Table 2.1). Eight of the ten geologic units listed in Table 2.1 are present in both Northern and Southern California, while sp and KJf are only found in Northern California.

Table 2.1: California geologic units considered in this study with percentage of state covered by each geologic unit. General descriptions taken from Wills et al. (2006, 2015).

Map Symbol	Geologic Unit Description	% Area Covered	Hazard
Qi	Intertidal Mud, including mud around the San Francisco Bay and similar mud in the Sacramento/San Joaquin delta and in Humboldt Bay	0.3	Liquefaction
af/qi	Artificial fill over intertidal mud around San Francisco Bay	0.1	Liquefaction
Qal1	Quaternary (Holocene) alluvium in areas where it is known to be predominantly fine	8.2	Liquefaction
Qal2	Quaternary (Holocene) alluvium in areas where the alluvium (Holocene and Pleistocene) is more than 30 m thick	6.6	Liquefaction
Qal3	Quaternary (Holocene) alluvium on slopes steeper than 2%	10.2	Liquefaction/Landslide
Qoa	Quaternary (older Pleistocene) alluvium	10.3	Liquefaction/Landslide
Qs	Quaternary (Pleistocene) sand deposits, such as the Merritt Sand in the Oakland area	0.1	Liquefaction
QT	Quaternary to Tertiary alluvial deposits such as the Saugus Formation of Southern California, Paso Robles Formation of central coast ranges, and the Santa Clara Formation of the Bay Area	2.3	Landslide
Tsh	Tertiary shale and siltstone units such as the Repetto, Fernando, Puente, and Modelo Formations of the Los Angeles area	3.3	Landslide
Tss	Tertiary sandstone units such as the Topanga Formation in the Los Angeles area and the Butano sandstone in the San Francisco Bay area	8.3	Landslide
Tv	Tertiary volcanic units including the Conejo Volcanics in the Santa Monica Mountains and the Leona Rhyolite in the East Bay Hills	11.0	Landslide
sp	Serpentine, generally considered part of the Franciscan complex	1.0	Landslide
Kss	Cretaceous sandstone of the Great Valley Sequence in the central Coast Ranges	2.3	Landslide
KJf	Franciscan complex rock, including melange, sandstone, shale, chert, and greenstone	6.4	Landslide
crystalline	Crystalline rocks, including Cretaceous granitic rocks, Jurassic metamorphic rocks, schist, and Precambrian gneiss	28.7	Landslide

Table 2.1 shows that the geology of California consists largely of Crystalline rocks present in the Sierra Nevada mountains followed by Tertiary Volcanics prevalent in the upper part of Northern California. Weakly cemented sedimentary rocks such as Tertiary Shale (Tsh) and Tertiary Sandstones (Tss) are materials known to be highly susceptible to landslides based on their lithology (Wills et al., 2005). Tsh is a fine-grained material consisting mostly of claystone, mudstone and shale, while Tss is coarse-grained consisting primarily of sandstone and conglomerate.

2.2 Digital Elevation Model

Terrain and elevation-related data and maps were developed using the national elevation dataset (USGS, 2018), which is a high resolution (10-m grid points) Digital Elevation Model (DEM) derived from light detection and ranging (LIDAR) data and made available to us by CGS. DEMs are used to obtain elevations that are considered in groundwater estimates. Ground slopes computed from DEMs are used in landslide displacement analyses and in empirical models for prediction of lateral spread displacements.

2.3 Groundwater

Groundwater hydrology was defined using the California well database (California Water Board, 2020; Figure 2.3) and a global model reliant upon climate, terrain, and sea level data (Fan et al., 2013). We had access to 31,359 unique well locations, and 1,045,240 water table depth measurements taken between 1914 and 2015. On average, there were 33 measurements per well. Figure 2.4 summarizes the measurements per well, and Table 2.2 summarizes the number of wells and measurements by geologic unit.

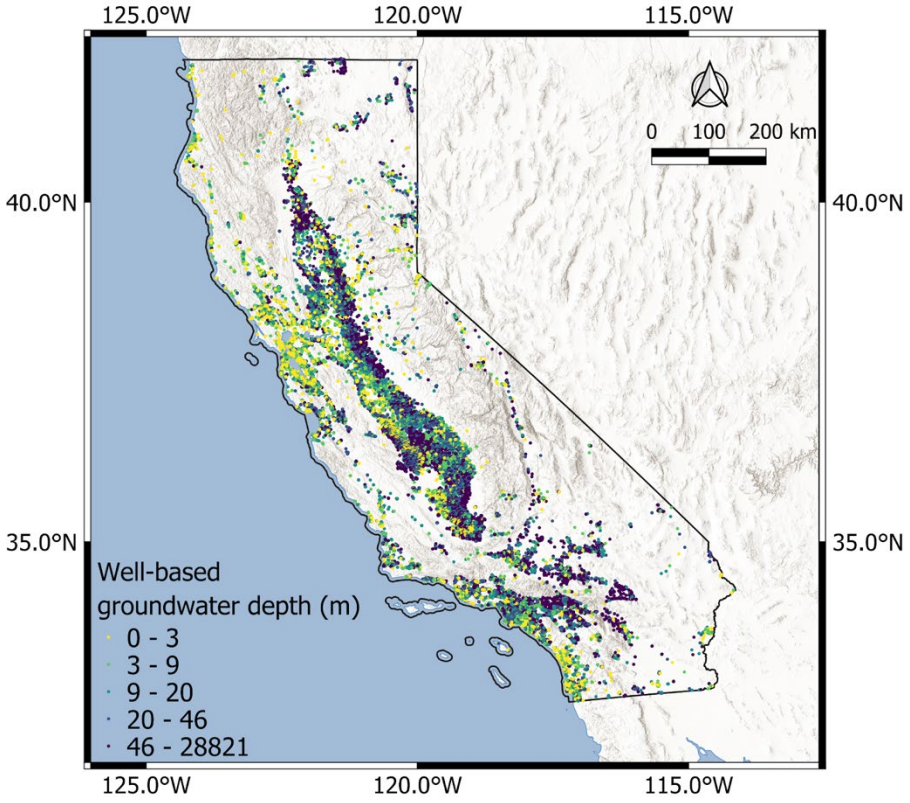

Figure 2.3. California well database (data from the California Water Board, 2020) (adapted from Zimmaro et al., 2021)

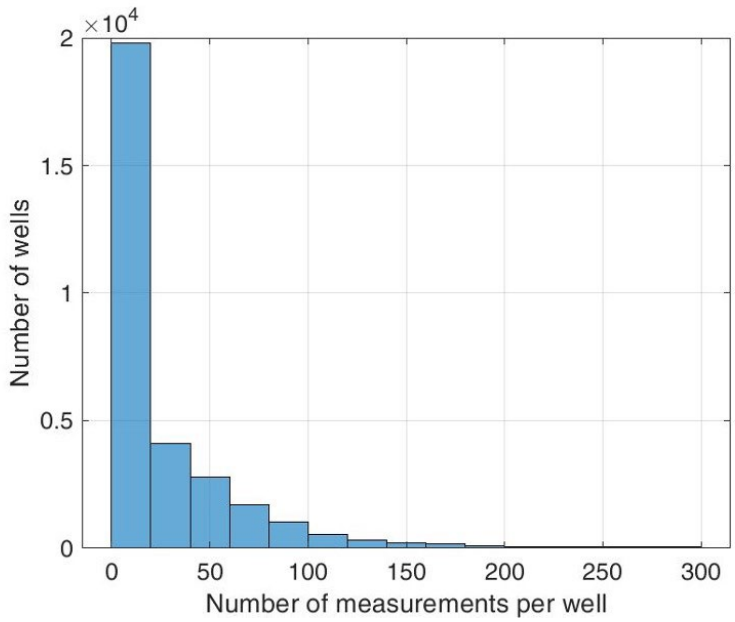

Figure 2.4. Histogram indicating the number of measurements per well; location of wells is shown in Figure 2.3

Table 2.2. Number of wells and measurements by geologic unit

Geologic Unit	Abbreviation	Number of wells	Number of measurements
Artificial fill over intertidal mud	af/Qi	14	356
Franciscan complex rocks	KJf	13	134
Cretaceous sandstone	Kss	3	179
Artificial dam fill	adf	1	22
Quaternary (H) alluvium (slope <0.5%)	Qal1	2,229	132,499
Quaternary (H) alluvium (0.5% < slope < 2.0%)	Qal2	5,868	189,373
Quaternary (H) alluvium (2.0% < slope)	Qal3	2,245	46,620
Intertidal mud	Qi	22	662
Quaternary (P) alluvium	Qoa	7,451	235,133
Quaternary (P) sand deposits	Qs	69	820
Quaternary to tertiary alluvium	QT	511	11,544
Tertiary shale and siltstone units	Tsh	24	1,549
Tertiary sandstone units	Tss	431	15,972
Tertiary volcanic units	Tv	33	246
Crystalline	crystalline	114	860

2.4 Cone Penetration Test Soundings

Data were downloaded from the publicly available USGS online repository: https://earthquake.usgs.gov/research/cpt/. The USGS CPT uses a 23-ton truck. There are 910 CPT soundings available in California, most of which are concentrated in the two major urban areas of Los Angeles and San Francisco. The locations of the CPT sounding sites are shown in Figure 2.5 below. For each site, we had access to tip resistance (Qt), sleeve friction (Fs) and the derivative friction ratio (Fs/Qt [%]) as a function of depth.

Table 2.3. Representation of CPTs used in this project by unit

Geologic Unit	Abbreviation	SoCal	NorCal	Total
Artificial fill over intertidal mud	af/Qi	0	99	99
Franciscan complex rocks	KJf	0	1	1
Quaternary (H) alluvium (slope <0.5%)	Qal1	149	184	333
Quaternary (H) alluvium (0.5% < slope < 2.0%)	Qal2	180	176	356
Quaternary (H) alluvium (2.0% < slope)	Qal3	81	65	146
Intertidal mud	Qi	0	6	6
Quaternary (P) alluvium	Qoa	11	34	45
Quaternary (P) sand deposits	Qs	0	27	27
Quaternary to tertiary alluvium	QT	1	0	1
Serpentine	sp	0	2	2
Tertiary shale and siltstone units	Tsh	1	0	1
Tertiary sandstone units	Tss	0	1	1
Tertiary volcanic units	Tv	0	8	8

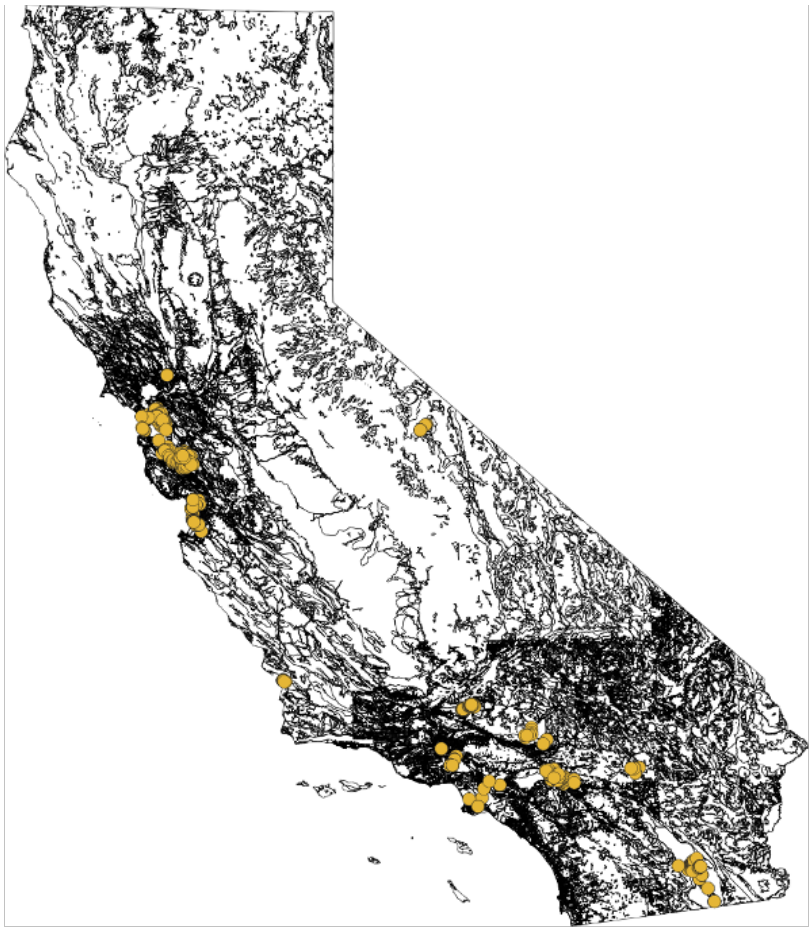

Figure 2.5. Geographic distribution of CPTs across the state of California.

2.5 Geotechnical Borehole Database

Shear strength data as derived from laboratory tests was used to derive Mohr-Coulomb strength parameters for use in seismic landslide analyses (Chapter 3). The soil specimens tested are from boreholes conducted as part of geotechnical investigations for sites in California. The data that we had access to for this study is for projects reviewed by the Office of Statewide Health Planning and Development (OSHPD) (pre-2021), now the Department of Health Care Access and Information (HCAI). These projects are related to health care facilities and schools in California.

A database of laboratory test results was provided to us by CGS on April 8, 2020. This is a relational database with more than 20,000 borehole data points, grain size distribution data, and shear strength values from geotechnical laboratory data. This database was accessed using SQL commands and data was extracted by means of specific queries.

Shear strength parameters for landslide analysis were obtained from the CGS database. The database contains over 13,000 boreholes with c′ and ϕ' from geotechnical strength testing (mostly direct shear tests conducted by consultants), as well as lithology and geologic descriptions of samples reported in the borehole logs. These boreholes, as shown in Figure 2.6, are concentrated around the San Francisco Bay area in Northern California and Los Angeles area in Southern California. The data from the San Francisco Bay area will be used for geologic units throughout Northern California, and the data from the Los Angeles area will be used for geologic units throughout Southern California.

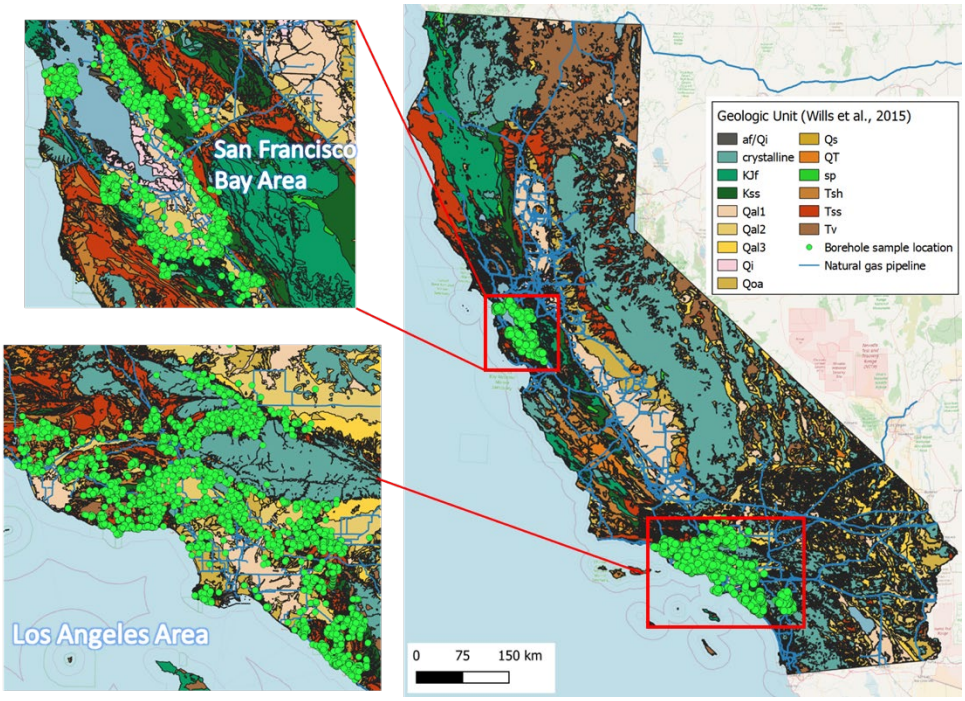

Figure 2.6: Map showing CGS borehole sample locations in San Francisco Bay and Los Angeles areas

The geologic units used to define the lithology of samples in the CGS borehole database are not the same as the Wills et al. (2015) geologic units, and generally are more detailed. The CGS geologic units were reviewed and assigned to the appropriate surface geologic units from Wills et al. (2015) according to their descriptions and the interpretation of the lithology and grain sizes.

Additionally, geologic unit descriptions available in unpublished working files provided by Chris Wills, in CGS seismic hazard zoning reports (SHZR), and in Detweiler and Wein (2017) were consulted to aid in grouping the borehole data lithologies into appropriate geologic units. The SHZR and Haywired reports include shear strength parameters that were used to compute estimates of seismic landslide zones for the various geologic units in the regions assessed. These parameters serve as a reference for shear strength comparisons later in this section. The resulting CGS borehole geologic units that were assigned to each Wills et al. (2015) geologic unit are listed

in Table 2.4 for Northern California and Table 2.5 for Southern California. The descriptions for the geologic units listed in Table 2.2 and Table 2.3 were taken from the SHZR and Haywired reports.

Table 2.4. Borehole subunits grouped with surface geologic units (Northern California).

Geologic Units (Wills, 2015)	Sub-units from CGS Borehole Database	
Qal3	Qhf	Holocene alluvial fan deposits
Qoa	Qpf	Late Pleistocene alluvial fan deposits
	Qof	Older alluvial fan deposits (late to early Pleistocene) Moderately well to deeply dissected alluvial deposits; in places, original fan-surface morphology is preserved
	Qoa	Alluvium (early Pleistocene)
QT	QTsc	The Santa Clara Formation of lower Pleistocene and upper Pliocene age consists of poorly indurated conglomerate, sandstone, and mudstone in irregular and lenticular beds.
	QTl	The Pliocene-Pleistocene Livermore Gravels unit is exposed only within Assemblage V. Material in this unit accumulated in shallow braided stream and alluvial-fan depositional environments and consists primarily of poorly to moderately consolidated, poorly bedded, cobble conglomerate, conglomeratic sandstone, and coarse-grained sandstone, with minor siltstone and claystone
Tsh	Tm	The Monterey Formation of middle Miocene age consists of porcelaneous mudstone and shale, impure diatomite, calcareous claystone with small amounts of sandstone and siltstone near the base
	Tcc	Claremont Formation. Chert and siliceous shale.
	Tms	Moraga Formation, Interflow sedimentary rocks
Tss	Tw	The Whiskey Hill Formation of middle and lower Eocene age consists of coarse-grained arkosic sandstone, with silty claystone, glauconitic sandstone and tuffaceous siltstone
Tv	Tmb	Dolomitic siltstone – Basal unit consisting of tan to yellowish-white, blocky to thin-bedded, dolomitic siltstone with thin cherty layers
Kss	Ku	An unnamed unit of Cretaceous rocks underlies Tertiary marine rocks along the eastern edge of the map area.
	Kbc	Conglomerate - Thick, indistinct beds of pebble, cobble, and less common boulder conglomerate interfingered with coarse-grained mica-quartz-lithic wacke
	Kjm	Mudstone (Lower Cretaceous and Upper Jurassic)
	Kcv	Unnamed sandstone, conglomerate, and shale of the Castro Valley area (Late Cretaceous, Turonian and younger(?))
	Ko	Oakland Sandstone (Late Cretaceous, Cenomanian and/or Turonian)
	KJs	Quartz ankerite-sericite schist (Cretaceous to Jurassic)
KJf	fm	undivided Franciscan complex mélange
	fg	Greenstone consists of basaltic flows, pillow lavas, breccias, tuffs and minor related intrusive rocks
	KJg	Granodioritic rocks (Cretaceous to Jurassic)—Variable in texture and composition, grades into diorite
	KJfm	Mélange – Chaotic mixture of fragmented rock masses embedded in a penetratively sheared matrix of argillite and crushed metasandstone.
	fss	Sandstone consists of fine- to coarse-grained graywacke with interbedded siltstone and shale
	fc	Chert (consists of thin to thick layers and commonly is rhythmically interbedded with thin shale layers
crystalline	Jgb	Gabbro and pillow basalt, basalt breccia and minor diabase are the most common ophiolitic rocks in the map area
	Jsv	Keratophyre and quartz keratophyre (Late Jurassic)
sp	sp	serpentine
	Jsp	Great Valley complex serpentinite
	Jos	Serpentinized ultramafic rocks

Table 2.5: Borehole subunits grouped with surface geologic units (Southern California)

Geologic Units (Wills, 2015)	Sub-units from CGS Borehole Database	
Qal3	Qa	Alluvium, undifferentiated, active channel late Holocene
Qoa	Qoa	Old alluvium, undivided late to middle Pleistocene
QT	QTs	Saugus Formation, undivided early Pleistocene, late Pliocene
	TQs	bedrock of the Plio-Pleistocene, nonmarine Saugus Formation
Tsh	Tm	Modelo Formation, undivided, mudstone, siltstone, shale late Miocene. The upper shale unit (Tm) consists of white-weathering, thin bedded, hard, platy to brittle, siliceous shale.
	Tmm	Malaga Mudstone Member—Radiolarian mudstone and diatomite
	Tpn1	Puente Formation, undivided, siltstone, sandstone, shale early Pliocene and late Miocene
	Tmd	Modelo Formation, diatomaceous shale late Miocene
	Tr	Trancas Formation, undivided, mudstone, silty shale, claystone middle and early Miocene
	Tpn2	Puente Formation, undivided, siltstone, sandstone, shale early Pliocene and late Miocene
	Tpy	Puente Formation, Yorba Member, siltstone late Miocene
Tss	Tt	Topanga Group, undivided, sedimentary and volcanic rocks middle Miocene
	Ts	Sespe Formation, undivided, conglomerate, sandstone late Eocene, Oligocene, early Miocene
Tv	Tc	Conejo Volcanics, undifferentiated middle Miocene
	Tvv	Vasquez Formation, interbedded volcanics early Miocene to Oligocene
	Tz	Zuma Volcanics early to middle Miocene
	Tcvb	Conejo Volcanics, basaltic flows and flow breccia middle Miocene
	Tco	Conejo Volcanics, undivided middle Miocene
Kss	Kc	Chatsworth Formation, sandstone late Cretaceous
	Kt	Tuna Canyon Formation, undivided marine sandstone, siltstone, conglomerate
crystalline	Kgr	Granitic rocks late Cretaceous
	gr	Granite, leucocratic plutonic rocks, quartz monzonite early Cretaceous to late Jurassic

3 Landslide Hazards

3.1 Introduction

The risk of earthquake-induced landslides is largely dependent on the material shear strength, geology, slope configuration, groundwater table and ground shaking intensity. The rigid sliding block approach has been used extensively to estimate the potential for earthquake-induced landslides on a regional scale (Dreyfus et al., 2013; Jibson et al., 2000; Jibson, 2007; Newmark, 1965). The approach requires the estimation of the slope yield acceleration, k_y which is defined as the horizontal acceleration that results in a factor of safety (FS) of 1.0, and k_y is used with the ground shaking intensity to compute seismic displacements (D). These displacements are related to the potential for an earthquake-induced landslide.

The calculation of k_y often utilizes an infinite slope assumption (Figure 3.1), which is a simplified representation of the actual slope configuration but is an effective configuration for regional-scale stability analyses (Dreyfus et al., 2013; Rathje and Saygili, 2008, 2009).

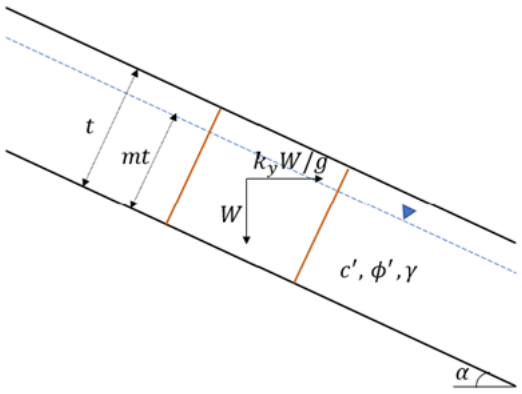

Figure 3.1. Representative geometric configuration of infinite slope model

The resulting expressions to compute k_y using the sliding block approach and the assumption of an infinite slope (Eqs. 3.1 and 3.2) are a function of the factor of safety, the effective cohesion (c'), the effective friction angle (ϕ'), the material and water unit weights (γ and γ_w, respectively), the slope angle (α), the thickness of the sliding mass (t), acceleration due to gravity (g), and the proportion of sliding mass that is saturated (m).

$$k_y = \frac{(FS-1)g}{\cos\alpha.tan\phi' + \frac{1}{tan\alpha}} \quad (3.1)$$

$$FS = \frac{c'}{\gamma.t.\sin\alpha} + \frac{\tan\phi'}{\tan\alpha}\left(1 - \frac{m.\gamma_w}{\gamma}\right) \quad (3.2)$$

The calculation of k_y is performed on a uniform grid across the study region, typically about 10 m.

Recent studies (Wang and Rathje 2015, 2018) have highlighted the importance of considering the uncertainty of shear strengths across geologic units and accounting for these uncertainties in seismic landslide predictions. One approach to incorporating these uncertainties in the prediction analysis is the use of logic trees, which is common practice in probabilistic seismic hazard analysis (Du et al., 2018; Rodriguez-Marek et al., 2021; Rathje and Saygili, 2009). This project builds upon previous work to develop a logic tree for seismic landslide analysis that can be utilized at the state-scale and incorporates not only parametric uncertainty but also differences in the displacement prediction models. The logic tree approach attempts to capture the different sources of uncertainties from different combinations of shear strength parameters, slope properties and displacement models.

3.2 General Methodology

The methodology employed in this study is summarized in the flow chart shown in Figure 3.2 The approach combines sliding displacement estimates at the grid level with identification of DEM-based slope units to define landslide zone polygons (LZP). For each LZP, statistical distributions of the landslide size (which can be smaller than the LZP), landslide movement, and direction of movement are defined.

The primary geospatial inputs essential for the estimation of sliding block displacements include a digital elevation model (DEM) for computing slope angle, digital regional-scale geologic maps, shear strength parameters, sliding mass thickness, water table data, and material unit weight, all of which are all used to compute k_y. The k_y along with the earthquake ground motion parameters are used to predict the landslide displacement.

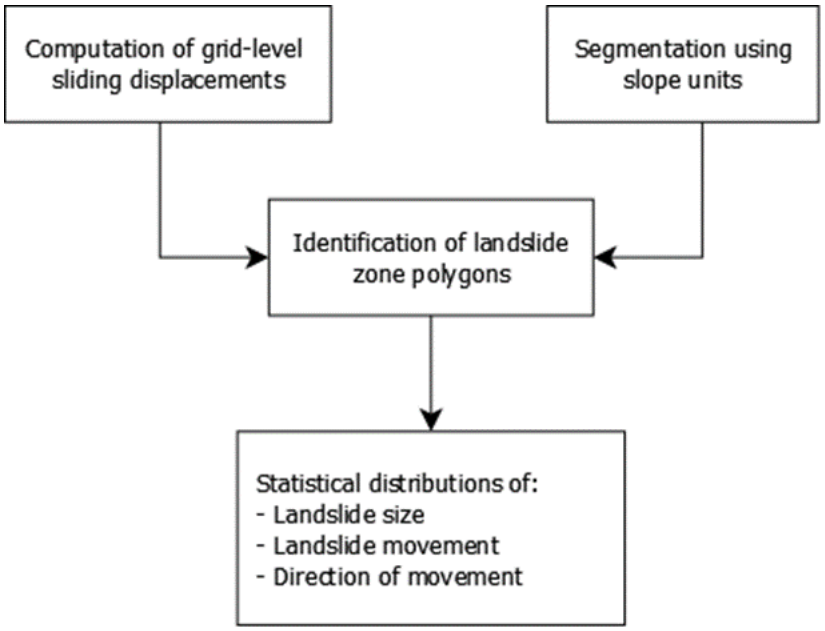

Figure 3.2. Methodology for regional-scale seismic landslide assessments

The workflow presented in Figure 3.3 shows the sources of the various input parameters used in this study and illustrates the general procedure for computing seismic displacement at the grid cell level. For this study, a 10-m resolution DEM from the California Geological Survey (CGS) was used to derive the slope angle for the entire region. The k_y is computed on the same 10-m grid using an infinite slope model (Eq. 3.1 and 3.2) and treating each cell as independent. A full probability distribution of k_y is computed from a logic tree that considers the uncertainty in each of the input parameters. Finally, the sliding displacements are computed using the values of k_y and a spatially correlated ground motion field that represents ground shaking from an event. Multiple ground motion fields and associated weights can be considered to represent the full ground motion hazard curve at a location (Baker et al., 2021).

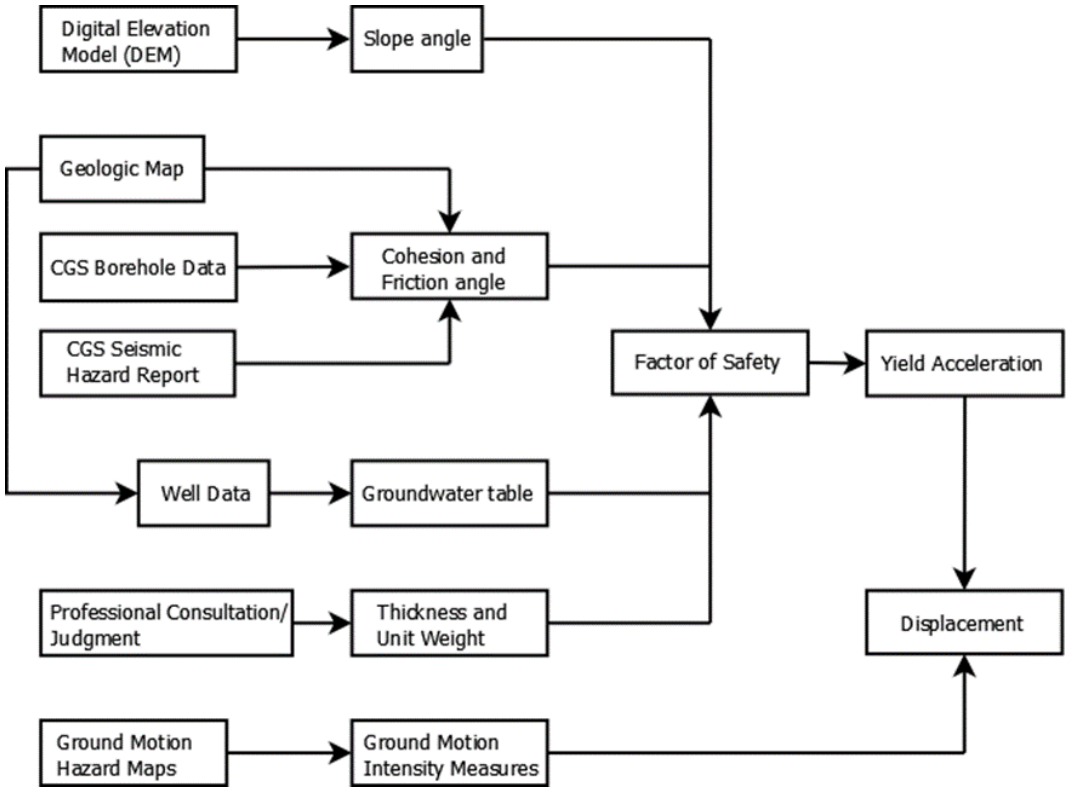

Figure 3.3. Workflow for computing seismic displacement at grid cell level

Throughout this study, probability distributions of k_y are re-sampled to fewer values following the discrete approximation approach described in Miller and Rice (1983). This approach uses a discretization method based on Gaussian quadrature where a finite number of values from a cumulative distribution function (CDF) are assigned specific weights to represent the full distribution. Miller and Rice (1983) developed the CDF probabilities and associated weights for different numbers of discrete, resampling points.

The primary outcome of the logic tree analysis is a probability distribution of sliding displacement for each 10-m grid cell. It should be noted that these displacements are indicators of potential landslide occurrence, they do not correspond to actual expected measured displacements in the field. The median displacement for each cell is computed from the cumulative density function and clusters of cells with median displacement greater than a set threshold value are created. These clusters signify areas that are susceptible to landslides and may be unrealistically large. Slope units are then used to segment the landslide-susceptible clusters into smaller areas that represent individual landslide zone polygons.

The next sections will focus on describing the assignment of shear strength to the geologic units, computation of statewide values of k_y, the prediction of the probability distributions of sliding displacement, the identification of landslide zone polygons, and the assignment of landslide size, movement, and direction to each landslide zone polygon.

3.3 Shear Strength Estimation

For each geologic unit, the shear strength parameters were statistically analyzed to obtain best estimates of c' and ϕ'. A total of 1,638 and 3,295 strength values were analyzed for Northern and Southern California, respectively. An example of the statistical distributions of c' and ϕ' for Tsh in Southern California is presented in Figure 3.4. Figure 3.4 shows that the c' data display a long tail that is characteristic of a lognormal distribution (Fanelli et al., 2015; Zhu et al., 2019), while the ϕ' data displays a Gaussian shape.

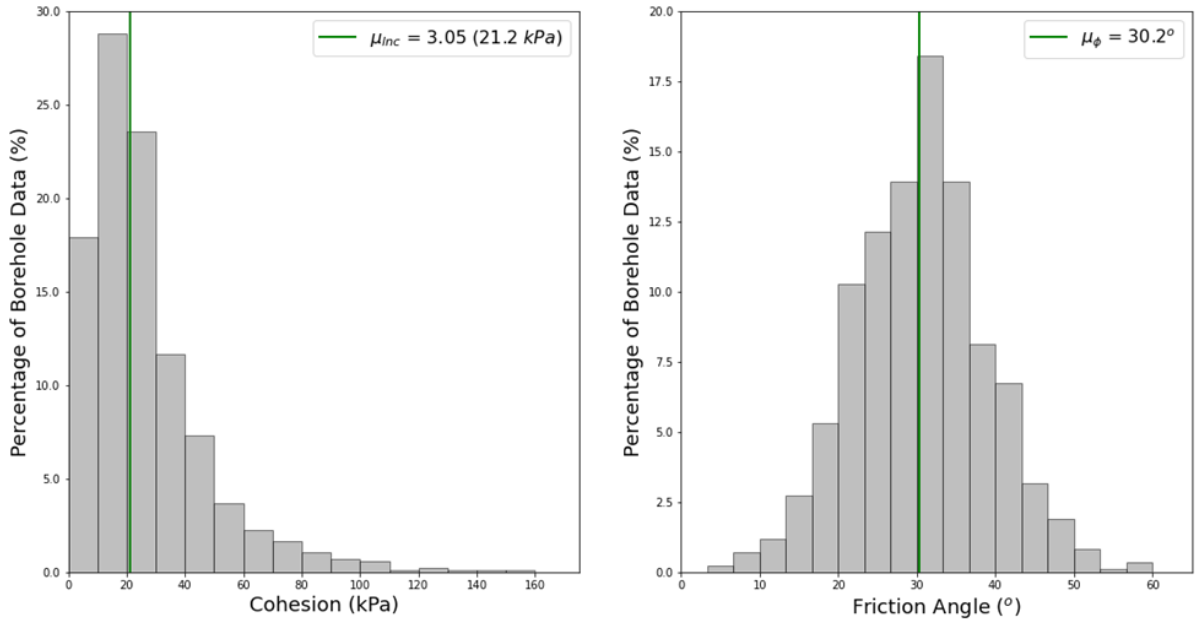

Figure 3.4. Distributions of c' and ϕ' computed from CGS borehole database for Tsh in Southern California, showing an example of normal and lognormal distributions.

We statistically tested the shape of the distributions for c' and ϕ' and established that it is reasonable to assume that c' is lognormally distributed and ϕ' is normally distributed. For the data shown in Figure 3.4 the mean value of the natural log of c' is 3.05 (i.e., 21.2 kPa) with a standard deviation of 0.72, while the mean value of ϕ' is 30.2º with a standard deviation of 8.5º.

3.3.1 Statistical summary of c' and ϕ' for each geologic unit

A summary of the computed statistics for c' and ϕ' for each of the geologic units considered in this study is presented in Table 3.1. The mean values of c' and ϕ' were adjusted for some geologic units in Northern California to ensure the strength of the unit was appropriate relative to other units of younger or older age. No adjustments were made to Southern California geologic units. The final statistics for c' and ϕ' in Table 3.1 are used to define the strength parameters incorporated in the logic tree.

Table 3.1. Computed statistics of shear strength parameters for each geologic unit.

Map Symbol	# of borehole samples	Computed cohesion from borehole data			Computed friction angle from borehole data	
		μ_{lnc}	$\mu_{c'}$ (kPa)	σ_{lnc}	μ_{ϕ} (°)	σ_{ϕ} (°)
Qal3	230	3.04	20.9	1.37	24.3	9.8
	409	2.29	9.9	0.8	32.2	6.6
Qoa	187	3.3	27	1.07	26.8	10.3
	427	2.41	11.1	0.9	32	7.7
QT	275	3.37	29	0.78	28.5	12.1
	397	2.85	17.2	0.81	31.4	8.1
Tsh	62	3.37	29	1.07	26.8	11.1
	848	3.05	21.2	0.72	30.2	8.5
Tss	269	3.4	30	0.72	28.3	10.4
	446	2.88	17.9	0.9	32.8	8.3
Tv	7	2.95	19.2	0.86	33	8.3
	460	3.18	24.1	0.82	30.5	9.1
sp	107	3.3	27	0.93	28	12.7
	not present in Southern California					
Kss	246	3.32	27.7	0.94	31	11
	111	3.01	20.3	0.82	33.4	8.4
KJf	188	3.32	27.6	0.84	32	11.7
	not present in Southern California					
crystalline	67	3.27	26.2	0.92	32	12
	197	2.85	17.2	1	36.9	6.2

Graphical representations of the final shear strength parameters for each geologic unit in Northern and Southern California are presented in Figure 3.5. Generally, the friction angle increases with geologic age, but the cohesion is a bit more variable with specific units having distinct values (e.g., Tv in Northern California and Tss in Southern California). sp and KJf are not present in Southern California.

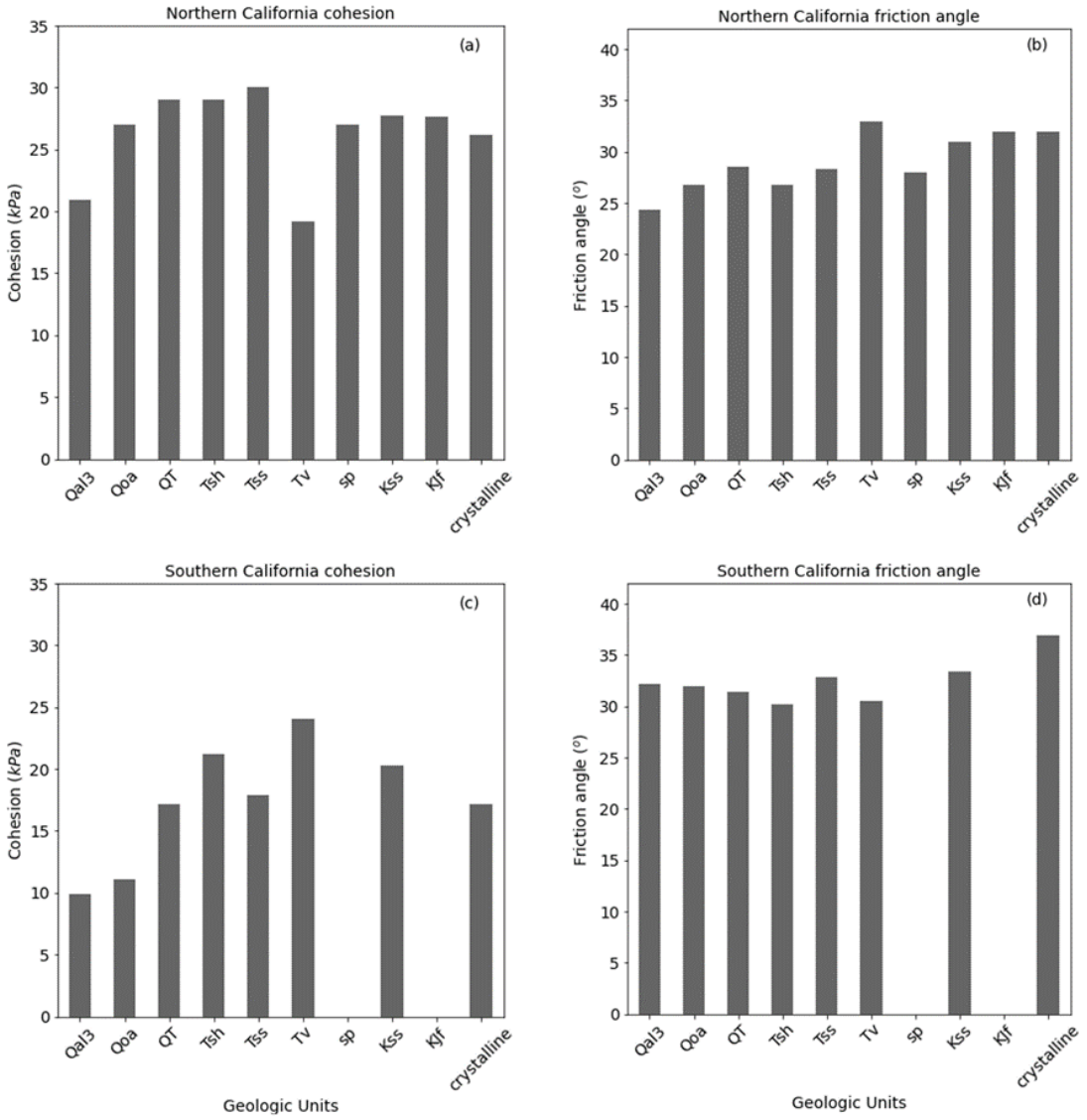

Figure 3.5. Plots of final shear strength parameters (a) cohesion and (b) friction angle for Northern California and (c) cohesion and (d) friction angle for Southern California.

Figure 3.6 compares the values of c' and ϕ' for Northern and Southern California for each geologic unit. The c' values in Northern California are higher than values obtained in Southern California for the same geologic units, while the reverse is the case for ϕ'. These data are consistent with materials being cohesion-dominant in Northern California and friction-dominant in Southern California. The higher c' values in Northern California also support the assumption of deeper sliding planes (larger t) used for geologic units in that region (see section on Sliding Block Properties).

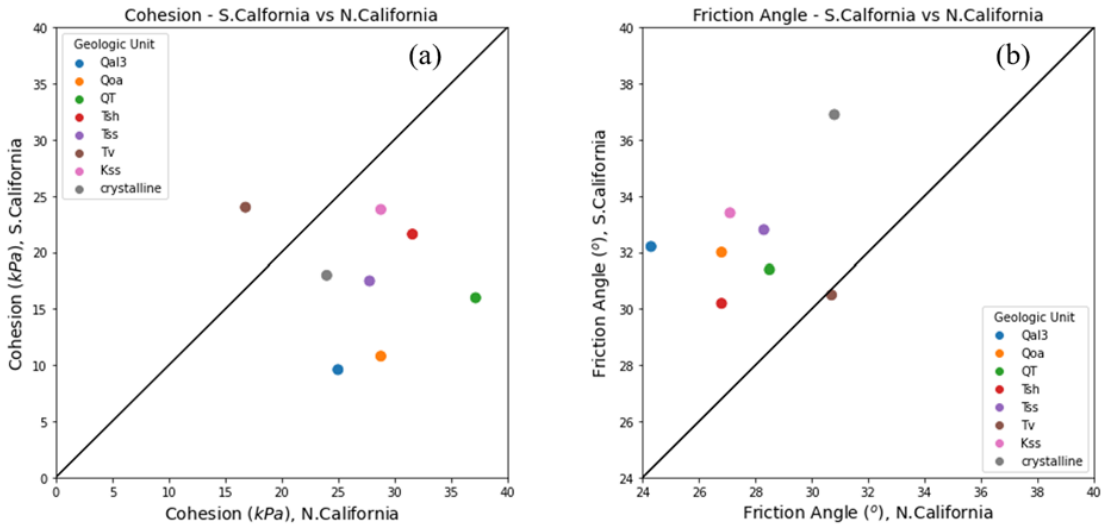

Figure 3.6. Comparison between strength parameters (a) cohesion and (b) friction angle for Northern and Southern California.

Because c' and ϕ' work together to define the shear strength, we compute the predicted shear strength for each geologic unit in Northern and Southern California (Figure 3.7). For comparison purposes, we compute the strengths for both regions at a normal effective stress of 50 kPa even though the sliding surfaces in Northern California are expected to be deeper relative to Southern California. Figure 3.7 shows that geologic units in Northern California are consistently stronger than those in Southern California at the same normal effective stress except for Tv which is slightly lower.

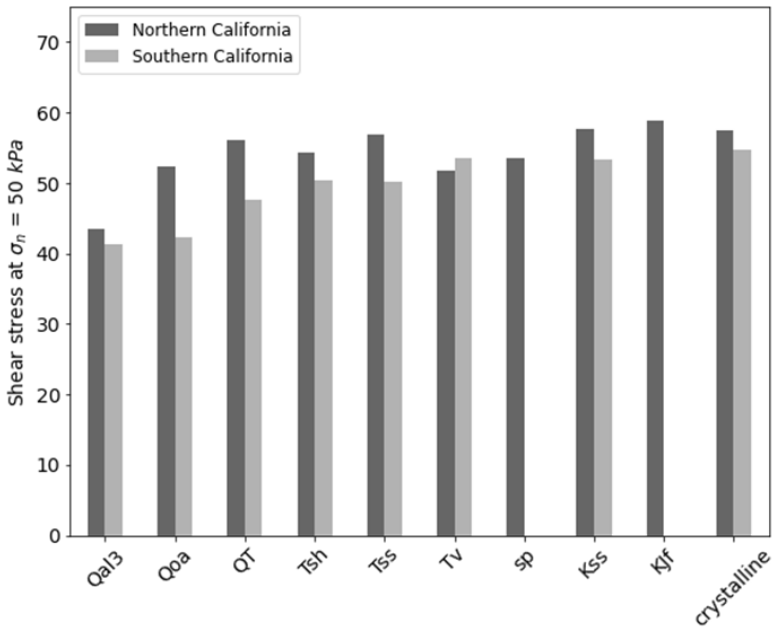

Figure 3.7. Predicted shear strength at an effective normal stress of 50 kPa for each geologic unit for Northern and Southern California.

3.3.2 Comparisons with other studies

The values of c' and ϕ' were compared with regional values reported in other studies. For Northern California, the shear strength parameters were compared with those used in the Haywired report (Detweiler and Wein, 2017) and for Southern California the shear strength parameters were compared with values from the CGS seismic hazard zoning reports (SHZR) and from Jibson et al. (2000). The specific quadrangles and geologic units used for shear strength comparison in the above-listed references are presented in Table 3.2

Table 3.2. Quadrangles and geologic units used for shear strength comparisons

Will et al. (2015) Geologic Unit	Northern California					Southern California			
	Haywired Geologic Unit	CGS SHZ Quadrangle and Unit Designation				CGS SHZ Quadrangle and Unit Designation			Jibson et al. (2000) Geologic Unit
Qal3	Qal-thin	Hayward Qhf	Cupertino Qhf	San Jose West Qhf		Palmdale Qal	Mount Baldy Qa		Qal
Qoa	Qoa	Hayward Qoa2, Qpf	Cupertino Qoa			Oat Mtn Qoa	Temecula Qoa	Mount Baldy Qoa	Qao
QT	QTs	Palo Alto QTsc	Cupertino QTsc (fbc), QTsc (abc)	San Jose West QTsc		Santa Paula Peak QTlp, QTs			QTs
Tsh	Tsh	Palo Alto Tm (abc)	Mindego Hill Tmsu (fbc), Tmsu (abc)	San Jose East Tcc	Briones Valley Tcc (fbc), Tcc (abc)	Los Angeles Tpn1,Tpn2	Point Dume Tm		Tm
Tss	Tss	Palo Alto Tw (fbc), Tw (abc)	San Jose East Tor	Briones Valley Tor (fbc), Tor (abc)		Los Angeles Tt1,Tt2	Oat Mtn Tt		Tt
Tv	Tv	Palo Alto Tmb	Briones Valley Tmb (fbc), Tmb (abc)			Point Dume Tv (fbc), Tv (abc), Tc			Tv
sp	Serp	Palo Alto sp	San Jose East Jsp (SCB), Jsp (ARB)	San Jose West Jsp	Mount Sizer Jos	Not available in Southern California			
Kss	Ks	Hayward Ko (fbc), Ko (abc)	San Jose East Kbc	Briones Valley Ku (fbc), Ku (abc)		Point Dume Kt	Temecula Kt	Oat Mtn Kc	Kc
KJf	KJf	Hayward KJfm	Palo Alto KJf	Cupertino fm	Briones Valley KJfs (fbc), KJfs (abc)	Not available in Southern California			
crystalline	Ji	Hayward Jgb, Jsv	Briones Valley gb, Jsv			Mount Baldy gr			

Figure 3.8 compares the strength parameters for Northern California and Figure 3.9 does the same for Southern California. For Northern California (Figure 3.8a), the values of c' from this study for five geologic units are within about +/- 10% of those from the Haywired report, but for the remaining units the values from this study are larger than used in the Haywired report. For ϕ' (Figure 3.8b), six geologic units are within about +/- 10% of those from the Haywired report, with the others both larger and smaller than the Haywired report. Interestingly, the friction angle values among the geologic units from this study do not vary as much as those from the Haywired report (24° to 31° vs. 24° to 36°).

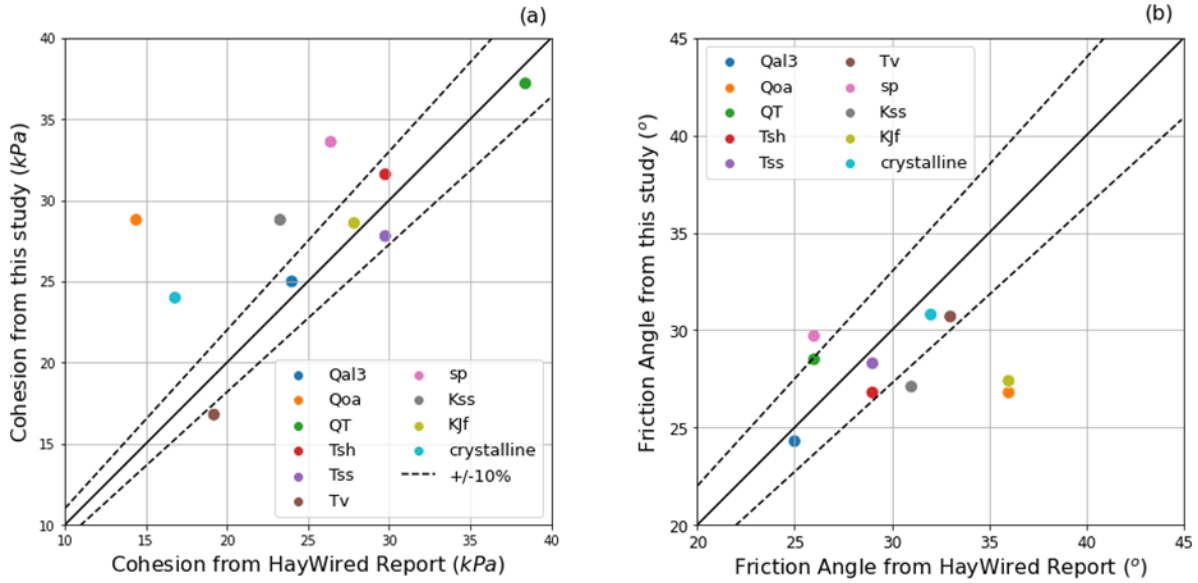

Figure 3.8. Comparison between Northern California strength parameters from this study and those from the Hayward fault scenario report for (a) cohesion and (b) friction angle

For Southern California (Figure 3.9a), the computed c' values for the Quaternary units tend to align well with those from the SHZR (within about +/- 10%), but they are larger than the SHZR for the older units (except for Tss). This discrepancy may be because the SHZR incorporated residual strength data into their shear strength parameter estimation where available (personal communication with CGS personnel). The computed ϕ' values for six geologic units are within about +/- 10% of those from the SHZR (Figure 3.9b). Similar to Northern California, the ϕ' values from this study generally fall within a narrower range (between 30° – 34°) than the SHZR (between 28° – 36°). When compared to the strength parameters used by Jibson et al. (2000) for the analysis of landslides from the 1994 Northridge earthquake (Figure 3.9c and Figure 3.9d), the values from this study are consistently smaller, about 10% smaller for ϕ' and significantly more for c', particularly for Kss. This difference is due to the fact that Jibson et al. (2000) used elevated strength parameters to ensure slopes up to 60° were statically stable. Crystalline has been omitted in Figure 3.9c and Figure 3.9d because there was no geologic formation to compare it with in Jibson et al. (2000).

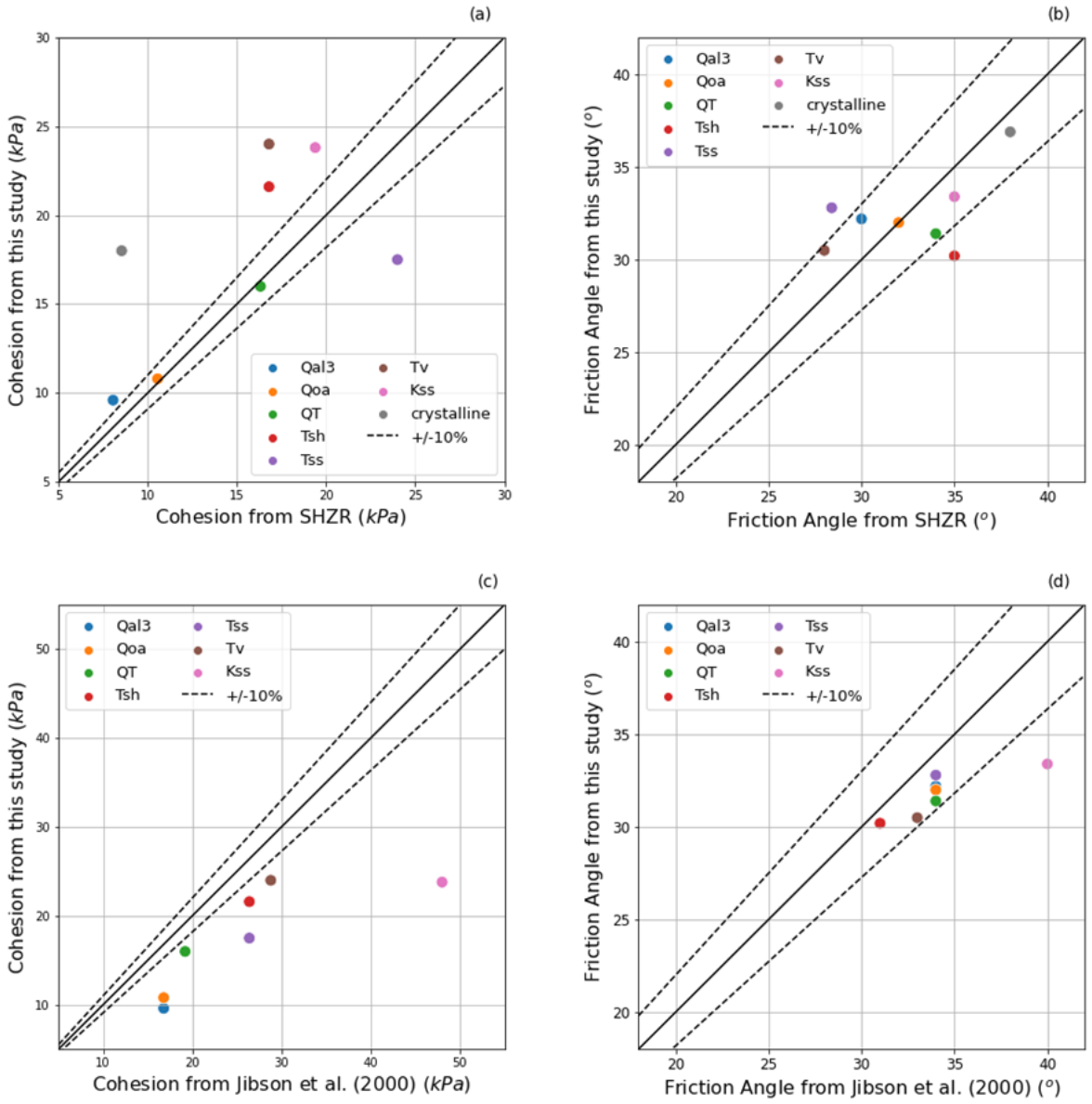

Figure 3.9. Comparison between Southern California strength parameters from this study and those from SHZR (a) and (b), and comparison with Jibson et al. (2000) (c) and (d)

As noted earlier, c' and ϕ' work together to define the shear strength at a given confining pressure. Thus, additional insights about the relative strengths from different studies for each geologic unit can be obtained by computing the shear strength at different values of effective stress. For Northern California, a confining pressure of 100 kPa, which represents the vertical effective stress at between 5 -10 m (depending on the location of the water table), was used to compute the strengths (Figure 3.10), while a confining pressure of 50 kPa was used for Southern California to represent a depth of between 2.5 - 5 m (Figure 3.11).

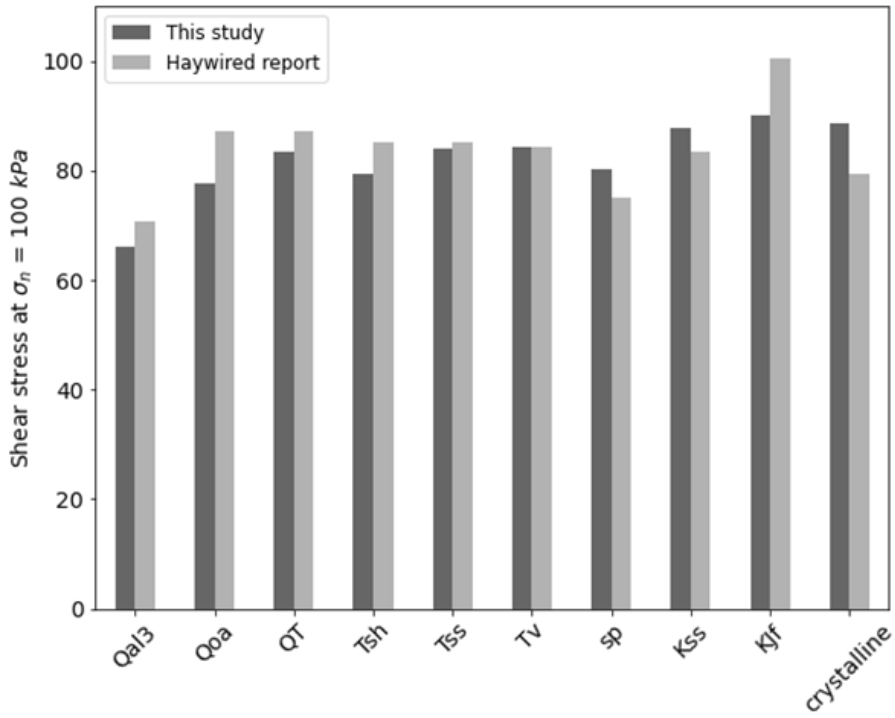

Figure 3.10. Comparison between shear strengths from this study and those from the Hayward fault scenario report by geologic units at a confining pressure of 100 kPa for Northern California

Figure 3.10 shows that the strength values for Northern California from this study compare well with those from the Haywired report, with strengths generally increasing with geologic age with the exception of sp. Similarly, the strength values for Southern California from this study compares well with those from the SHZR and Jibson et al. (2000) with the exception of Kss (Figure 3.11). As stated earlier, strength parameters in Jibson et al. (2000) were elevated to ensure slopes were statically stable.

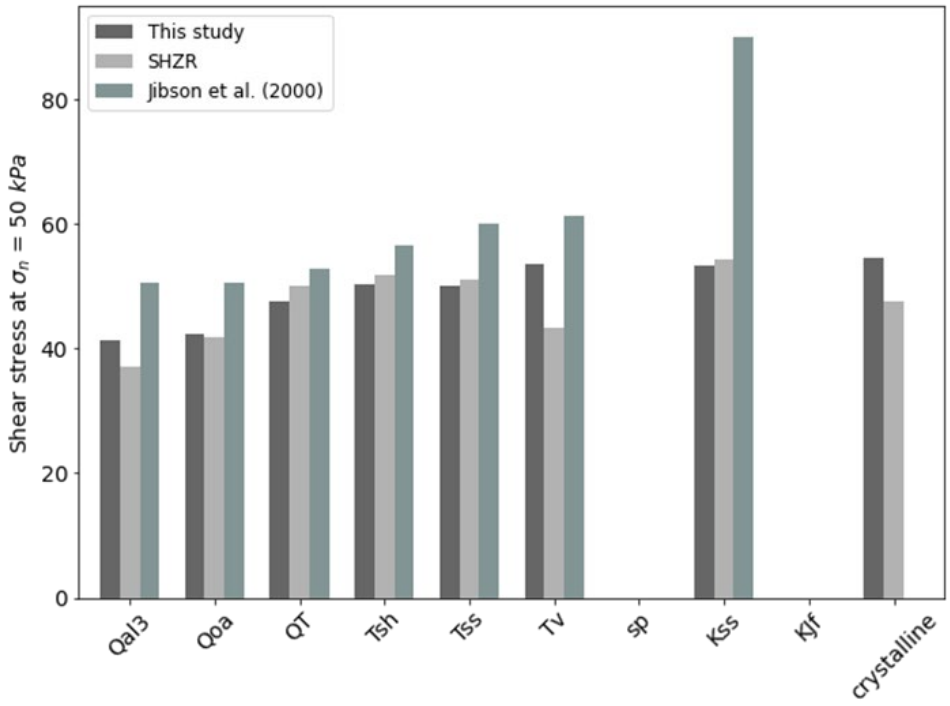

Figure 3.11. Comparison between computed shear strengths from this study and those from the SHZR and Jibson et al. (2000) by geologic units at a confining 50 kPa for Southern California. sp and KJf are not present in Southern California.

3.4 Computation of Grid-Level Yield Accelerations

3.4.1 Sliding Block Properties

In addition to shear strength, the k_y calculation also involves the slope angle, sliding mass thickness, groundwater table depth, and the soil unit weight. The soil unit weight is assumed to be 18 kN/m^3 across the entire region (Jibson et al. 2000, Dreyfus et al. 2013). The assignment of the other sliding block properties is described below.

A state-wide slope angle map was generated from the 10-m DEM, as shown in Figure 3.12. Slopes in California can be as steep as almost 80º in mountainous terrain with slopes less than 10º associated with alluvial fans and floodplains. Jibson and Michael (2009) reported that most landslides triggered by earthquake events are shallow in nature and occur on steeper slopes. Keefer (2013) reported 15º as the minimum slope inclination characteristic of disrupted landslides caused by earthquakes and 5º for landslides with minimal consequences. This study assessed seismic landslide displacements only on slopes with slopes greater than 10º.

The thickness of the sliding mass was derived from professional judgment in consultation with landslide experts. Jibson et al. (2000) used a value of 2.4 m across the Northridge earthquake study

area in Southern California based on the observation that reported depths of the sliding plane of observed landslides from the Northridge earthquake event were relatively shallow. Personal communication with the landslide experts confirmed that the sliding mass thickness in Northern California is generally deeper than Southern California. Based on these observations, three estimates of the sliding mass thickness were defined for each region: 1.5 m, 3 m and 4.5 m for Southern California and 5 m, 10 m and 15 m for Northern California.

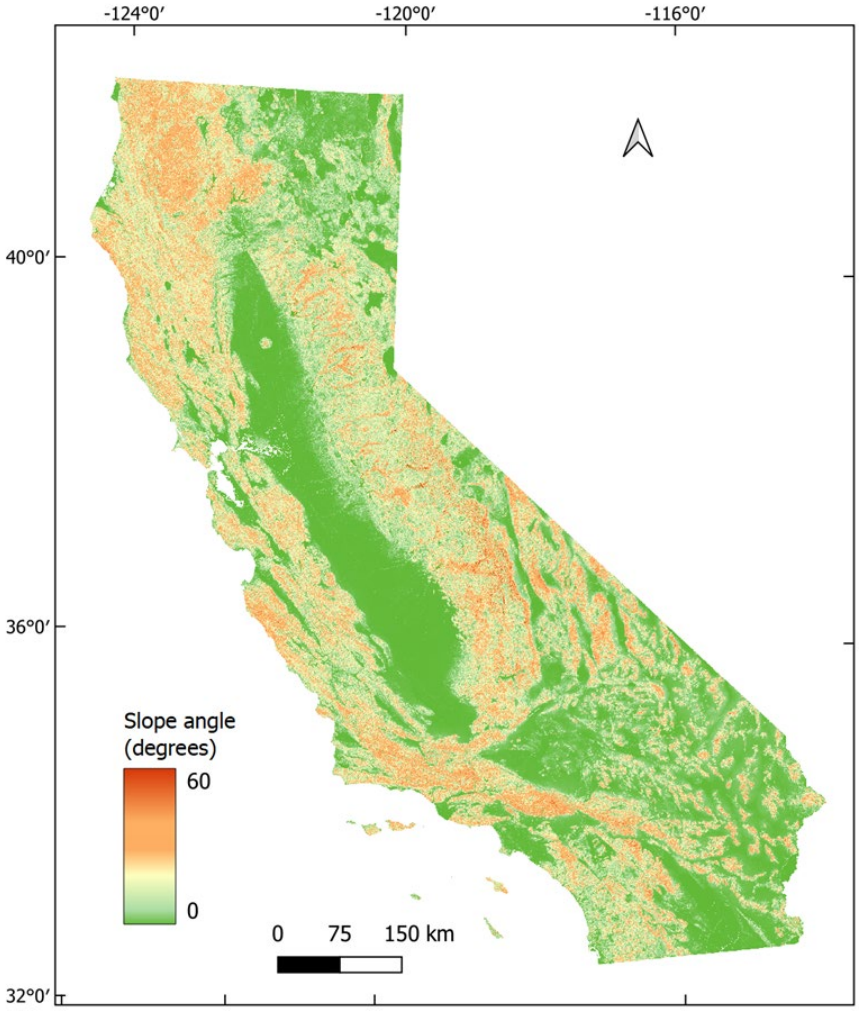

Figure 3.12. Slope angle map generated from 10-m DEM for California

The depth of the groundwater was based on well observations. Figure 3.13 shows the spatial distribution of the depth to the groundwater table (GWT) from well data obtained from the California well database (GAMA, 2020) overlain on the geologic map. This study analyzed well data on slopes steeper than 5º, which is flatter than the 10º threshold used for the landslide analysis. The reason to consider well data from flatter slopes is that there was little well data on steeper slopes and sufficient data was needed to define a range of groundwater levels. Well database was built to support construction and agriculture for irrigation which occurs mostly on flat grounds. The lack of well data in hilly terrain introduces uncertainty in the analysis; the uncertainty is considered through the logic tree.

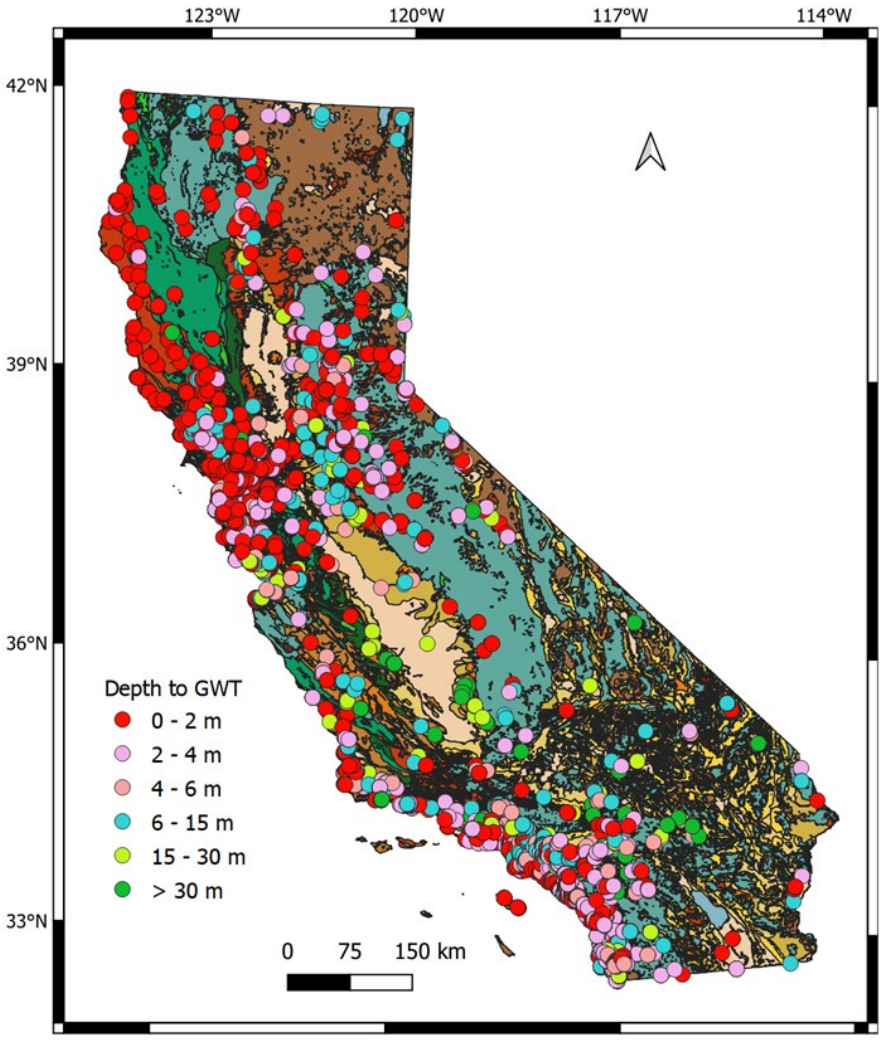

Figure 3.13. Mean annual depth to groundwater table from well data (GAMA, 2020)

Figure 3.14 shows the cumulative density functions of the groundwater depths from the well data for each geologic unit for Northern California (NoCal) and Southern California (SoCal). Most of the wells recorded shallow water depths less than 5 m for the sites considered (i.e., slopes > 5º), which is comparable to groundwater table depths in the San Francisco Bay area of 1.5 – 3 m (personal communication with local geotechnical engineer). For most places in Southern California, it is expected that the water table will be deeper than the modeled depth of the slip surface. Jibson et al. (2000) described most locations within the Northridge event area as arid, therefore the slopes were assumed to be dry for their analysis. The values in Figure 3.14 likely are not representative of the groundwater table depths at higher elevations and steeper slopes where landslides are expected. The values in Figure 3.14 are likely shallower than found in the hilly terrain, but without additional data it is difficult to evaluate different depths. Additionally, the wells do not account for the potential of a perched groundwater table, which will be present during rainy seasons. Therefore, we will use the well data in Figure 3.14 to assign groundwater table depth, acknowledging that the values may be conservative (i.e., shallower) for the dry season.

A summary of the number of wells and groundwater table depths assigned to each geologic unit is presented in Table 3.3. These values were taken from the cumulative density functions in Figure 3.14 at probabilities of 0.25, 0.5, and 0.75.

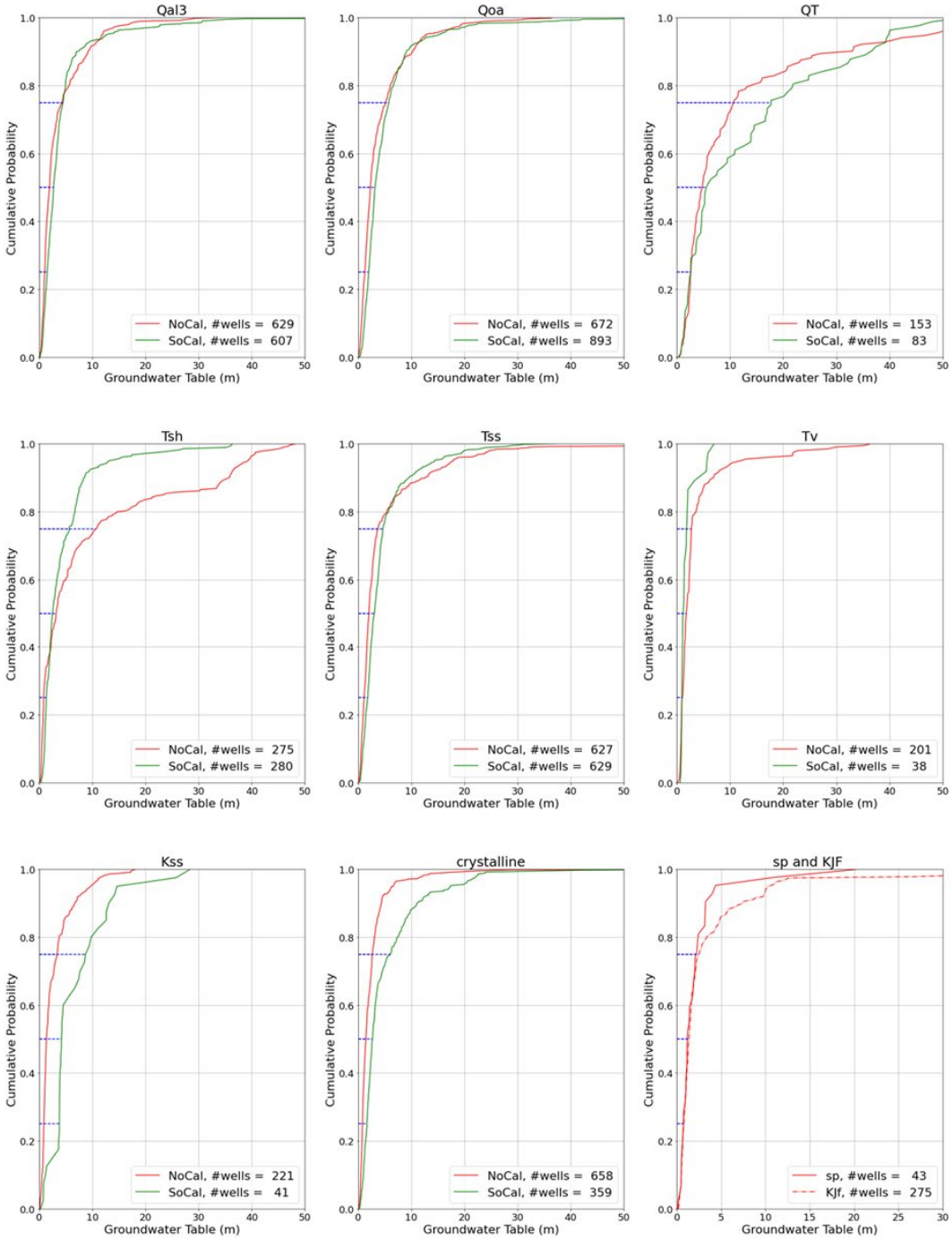

Figure 3.14. Distribution of groundwater table depth computed from California well database (GAMA, 2020)

The proportion of the sliding mass that is saturated (m), which is needed to compute k_y (eqns 3.1 and 3.2), is computed from the groundwater table depths (g_w) and the sliding mass thickness (t) using:

$$m = 1 - \frac{g_w}{t} \qquad (3.3)$$

The values of m are limited to $0 \leq m \leq 1$, with 0 representing a dry slope and 1 representing a fully saturated slope.

Table 3.3. Groundwater table depths assigned to different geologic units.

Map Symbol	Number of wells	Water table depth estimates (m)		
		Low	Best	High
Qal3	629*	1.02	1.96	4.34
	607*	1.49	2.72	4.47
Qoa	672	1.27	2.33	5.21
	893	1.98	3.22	5.81
QT	153	2.6	4.81	10.72
	83	2.55	5.64	17.71
Tsh	275	0.82	3.21	10.87
	280	1.32	2.54	5.67
Tss	627	1.14	2.04	3.72
	629	1.81	3.08	4.69
Tv	201	0.99	1.76	2.74
	38	0.94	1.17	1.83
sp	43	0.73	1.18	2.18
	not present in southern California			
Kss	221	0.88	1.37	3.37
	41	3.79	4.19	8.77
KJf	275	0.78	1.37	2.54
	not present in southern California			
crystalline	658	0.81	1.5	2.68
	359	1.67	2.72	6.12

*Values in black represent Northern California data while values in blue represent Southern California data.

3.4.2 Logic tree for k_y computation

For the k_y logic tree, the shear strength parameters (c' and ϕ') and the slope properties (t and m) are represented with three branches each, for a total of 81 branches (3 x 3 x 3 x3). For c' and ϕ', the three branches represent low, best, and high estimates of the shear strength parameters. It is important to consider the correlation between c' and ϕ' to avoid over or underestimating the shear strength. The correlation between c' and ϕ' is taken into account through a conditional distribution

for ln c', where the epsilon of ln c' ($\varepsilon_{\ln c'}$)) is conditioned on the epsilon of ϕ' ($\varepsilon_{\phi'}$) and the correlation coefficient ($\rho_{\ln c',\phi'}$) using:

$$\varepsilon_{lnc'} = \varepsilon_{\phi'} * \rho_{lnc',\phi'} \quad (3.4)$$

$$\mu_{lnc'|\varepsilon_{\phi'}} = \mu_{lnc'} + \varepsilon_{lnc'} * \sigma_{lnc'} \quad (3.5)$$

$$\sigma_{lnc'|\varepsilon_{\phi'}} = \sigma_{lnc'} * \sqrt{1 - \rho_{lnc',\phi'^2}} \quad (3.6)$$

The parameter $\rho_{\ln c',\phi'}$ reflects the degree of correlation between c' and ϕ', and it influences both the conditional mean and conditional standard deviation of $\ln c'$ (i.e., $\mu_{\ln c'|\varepsilon_{\phi'}}$ and $\sigma_{\ln c'|\varepsilon_{\phi'}}$). If there is no correlation between c' and ϕ' (i.e., when $\rho_{\ln c',\phi'} = 0$), neither $\mu_{\ln c'|\varepsilon_{\phi'}}$ nor $\sigma_{\ln c'|\varepsilon_{\phi'}}$ change from their original values. If there is perfect correlation (i.e., $\rho_{\ln c',\phi'} = 1$), $\varepsilon_{\ln c'} = \varepsilon_{\phi'}$ is used for $\mu_{\ln c'|\varepsilon_{\phi'}}$ and $\sigma_{\ln c'|\varepsilon_{\phi'}}$ is equal to 0. The correlation coefficient $\rho_{\ln c',\phi'}$ is assumed to be -0.5 for this study, which results in $\sigma_{\ln c'|\varepsilon_{\phi'}} = 0.87 * \sigma_{\ln c'}$.

To assign values of c' and ϕ' for the logic tree, three values of ϕ' are defined based on the $\mu_{\phi'}$ and $\sigma_{\phi'}$ for the geologic unit (Table 3.1) and $\varepsilon_{\phi'}$ = -1.4, 0, and +1.4. These values of ϕ' are assigned weights of 0.248, 0.504, and 0.248 based on the 3-point distribution from Miller and Rice (1983). These values of $\varepsilon_{\phi'}$ are used in eqns (3.4) – (3.6) to define the conditional distribution of $\ln c'$ (i.e., $\mu_{\ln c'|\varepsilon_{\phi'}}$ and $\sigma_{\ln c'|\varepsilon_{\phi'}}$), and these values are used to define three values of $\ln c'$ associated with $\varepsilon_{\ln c'}$ = -1.4, 0, and +1.4. Incorporating $\rho_{\ln c',\phi'}$ = -0.5 generates a smaller range of $\ln c'$ than if the two parameters were uncorrelated.

For the sliding mass thickness and groundwater table, the three values assigned to the logic tree are assigned weights of 0.248, 0.504, and 0.248. Although in these cases we are not directly using the 3-pt distribution from Miller and Rice (1983), the same weights are used for consistency.

Figure 3.15 displays the parameters in the logic tree for a single 10-m grid cell within the Tsh geologic unit in Northern California. The values assigned to the middle branches are the best estimates reported in Table 3.1 for c' and ϕ' and Table 3.3 for m . The k_y computation, using Eqs. (1) and (2), follows all possible branches of input parameter combinations through the logic tree, producing 81 k_y values for each 10-m grid cell throughout the state. To ensure all slopes were statically stable, a minimum FS of 1.1 was applied to each grid cell where required. Dreyfus et al. (2013) followed a similar approach. In contrast, Jibson et al. (2000) increased the strength of the geologic units to ensure that all slopes up to 60 were statically stable. The weight of each of the 81 k_y branches is the product of all the weights along the contributing branches as in Eq. (3.7)

$$w_{ky,i} = w_{\phi,i} * w_{c,i} * w_{t,i} * w_{m,i} \quad (3.7)$$

where w_ϕ, w_c. w_t and w_m are the weights of ϕ', c', t and m respectively.

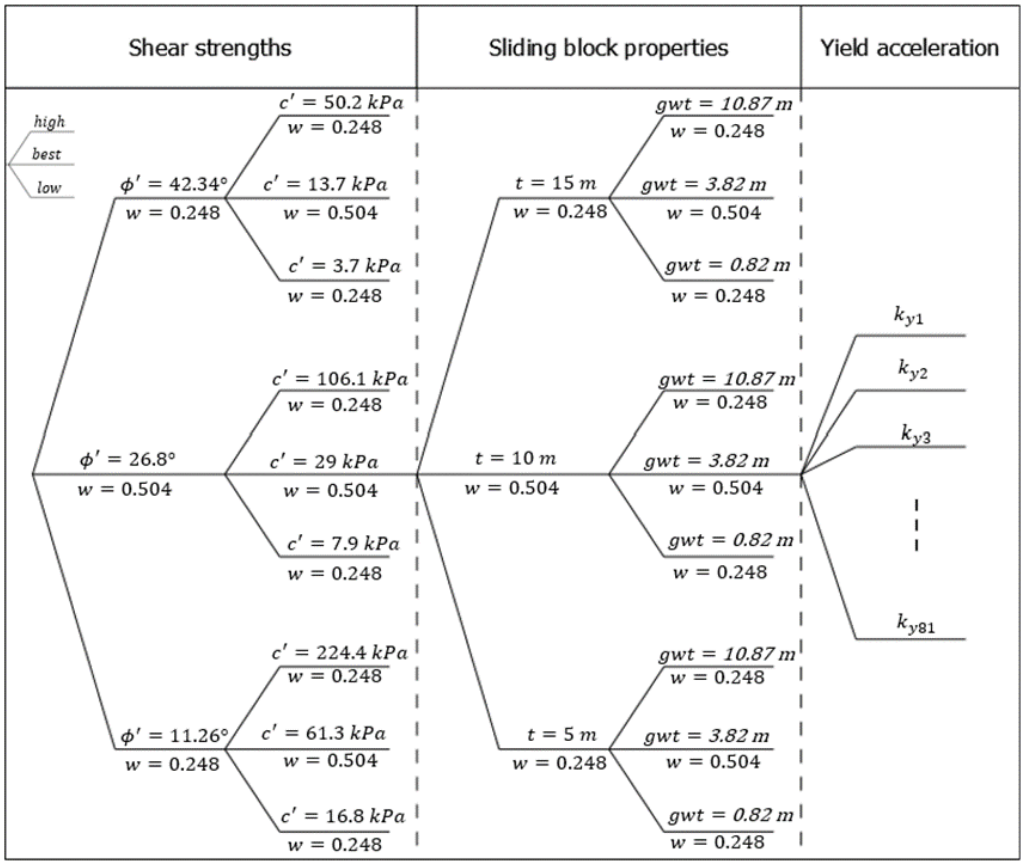

Figure 3.15. k_y logic tree for geologic unit Tsh in Northern California

The k_y values and their corresponding weights are then combined and sorted to generate a cumulative density function (CDF) for each cell, as shown in Figure 3.16. The spread of the CDF denotes the degree of uncertainty in the values of k_y. For every increase in the number of branches within a logic tree, there is an associated increase in computational demand and efficiency to compute and store the k_y values and then the displacements. This issue is particularly significant for large-scale regional analysis. Thus, it was important to limit the number of k_y branches to a reasonable number before moving on to the displacement calculation. In this case, the k_y values were re-sampled into a 7-point distribution using the approach described in Miller and Rice (1983). Here, specific values of the 7-point CDF are used to define the associated k_y values and the weights defined by Miller and Rice (1983) are assigned to each value of k_y . Figure 3.16 also shows the re-sampled 7-point distribution of k_y derived from the specific CDF percentiles. The re-sampled k_y values and the associated weights, w_{ky} are then used to compute the displacements. Table 3.4 presents the re-sampled k_y values and weights for the plotted CDF in Figure 3.16.

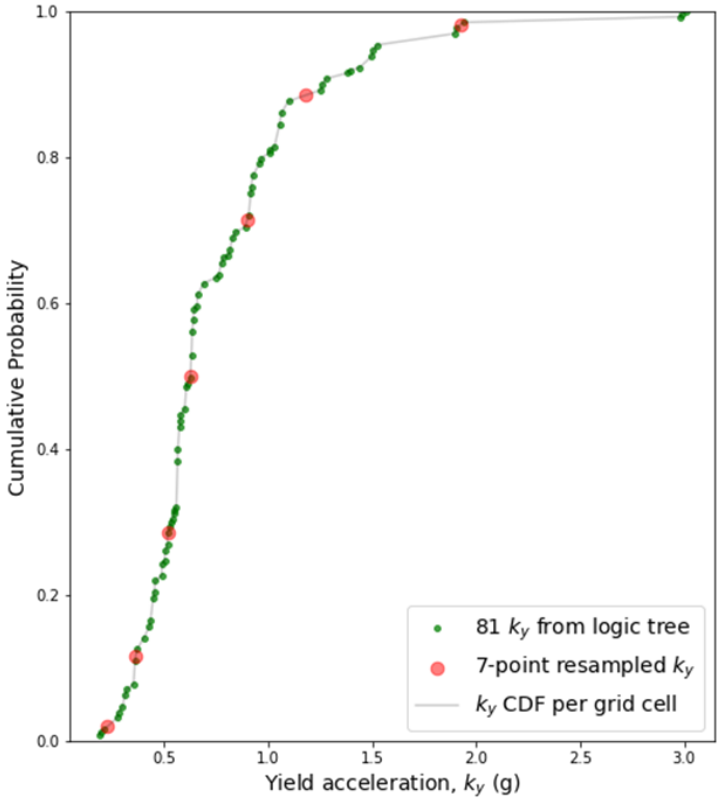

Figure 3.16. Full 81 k_y distribution for one 10-m grid cell (green dots). Red dots show the resampled values using Miller and Rice (1983) 7-point approximation.

Table 3.4. Re-sampled k_y values and weights for displacement computation for one grid cell. CDF points and weights are from Miller and Rice (1983)

7-point CDF	Weight	k_y (g)
0.019106	0.054866	0.227
0.115498	0.135893	0.363
0.285336	0.198097	0.516
0.50000	0.222288	0.625
0.714664	0.198097	0.899
0.884502	0.135893	1.177
0.980894	0.054866	1.922

3.5 Computation of Grid-Level Displacements

3.5.1 Logic tree for displacement predictions

In computing the seismic displacements, three empirical predictive models developed by Rathje and Saygili (2009) and Jibson (2007) were utilized. The models take the general form of

$$\ln D = fxn(IM, k_y) + \sigma_{\ln D} \quad (3.8)$$

where lnD is the natural logarithm of D in cm, IM is the vector of earthquake ground motion intensity measures (e.g., peak ground acceleration, PGA) and $\sigma_{\ln D}$ represents the aleatory variability or randomness in the predictive models. Two of the predictive models (Jibson, 2007; Rathje and Saygili, 2009) use a combination of earthquake magnitude (M) and PGA and each is given a weight of 0.3. The third model uses a combination of PGA and PGV (Rathje and Saygili, 2009) and is given a weight of 0.4. This larger weight reflects the belief that incorporating multiple ground motion intensity measures will produce more accurate predictions.

The spatial distribution of ground motion intensity measures used in this study were generated by Wang et al. (2022), incorporating a scenario-based approach that includes spatial correlation. Given the spatial distribution of the IM, the seven re-sampled k_y values combined with the three displacement models are used to compute 21 values of D and its standard deviation for each of the 10-m grid cells within California, following the logic tree shown in Figure 3.17. All predicted displacements less than 0.1 cm are set to a value of 0.1 cm. Cells with slope angle less than 10º are not analyzed and are assigned null values. The weight of each of the 21 D branches is a product of the weights of k_y and those of the displacement models along the contributing branches.

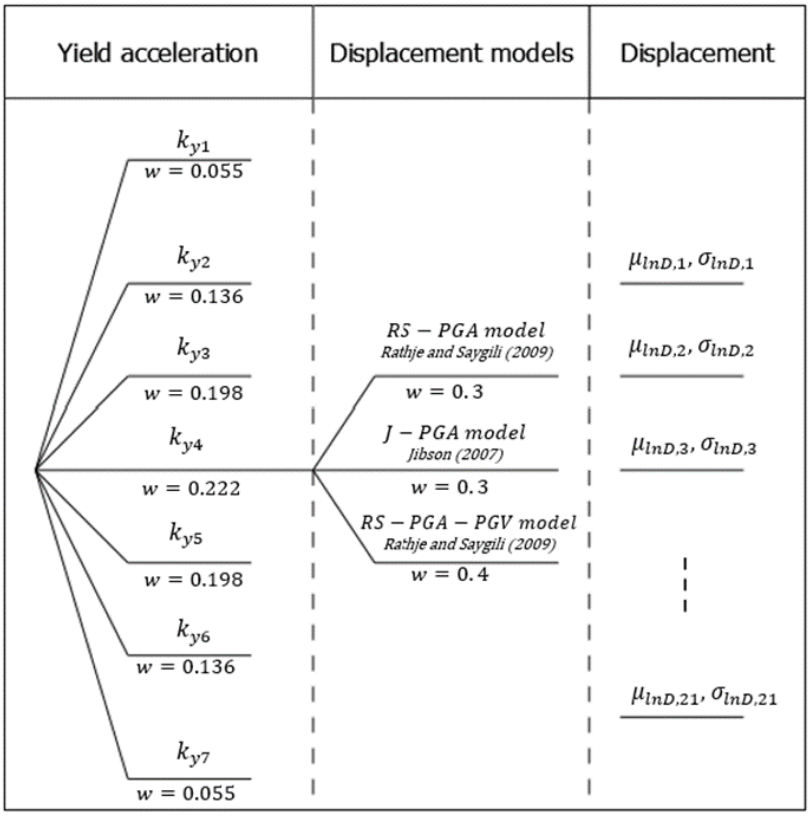

Figure 3.17. Displacement logic tree computed from 7 resampled k_y, ground motion intensity measures (M, PGA and PGV) and 3 displacement models.

3.5.2 Variability in the predictive displacement models

To account for the aleatory variability in the predictive displacement models, we compute $\sigma_{\ln D}$ at the end of each displacement branch (Figure 3.17) and sample the distribution associated with $\sigma_{\ln D}$ using a 5-point discrete approximation from Miller and Rice (1983). This approach defines the probability distribution of the displacement at the end of each logic tree branch using $\mu_{\ln D}$ and $\sigma_{\ln D}$, and then samples the distribution using the 5 CDF values and associated weights defined by Miller and Rice (1983). This expanded logic tree is shown in Figure 3.18. Incorporating the model variability results in a total of 105 displacement values (7 k_y x 3 D models x 5-point approximation of $\sigma_{\ln D}$) per grid cell per ground motion scenario. The final CDF of displacement for an example cell for a ground motion scenario of M = 6.7, PGA = 0.82 g and PGV= 100 cm/s is displayed in Figure 3.19, with values ranging from 0.1 cm to about 600 cm. The median displacement (D_{med} from this CDF is used for subsequent analyses.

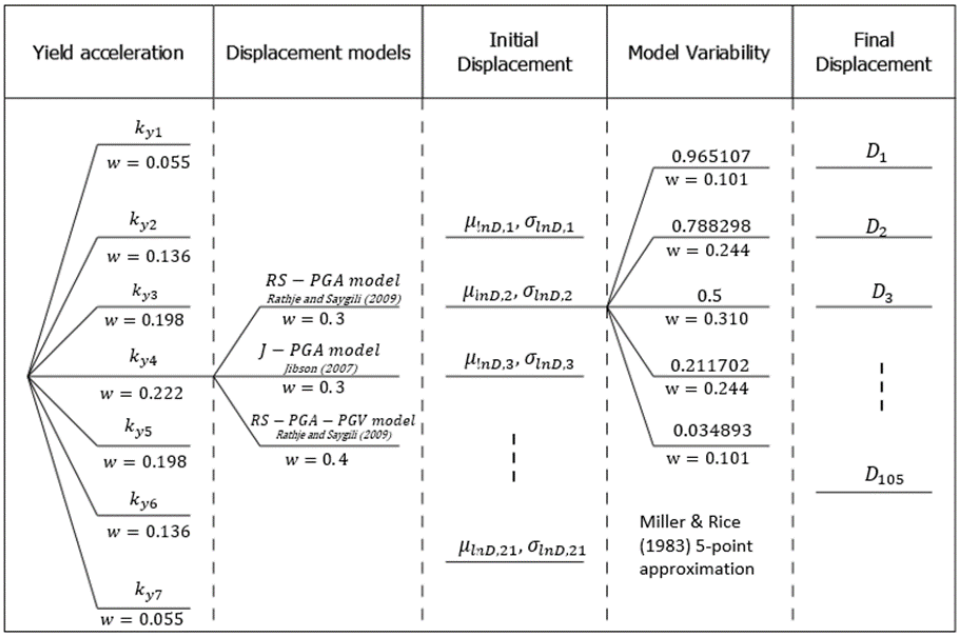

Figure 3.18. Full displacement logic tree implemented to compute the displacement CDF for each grid cell.

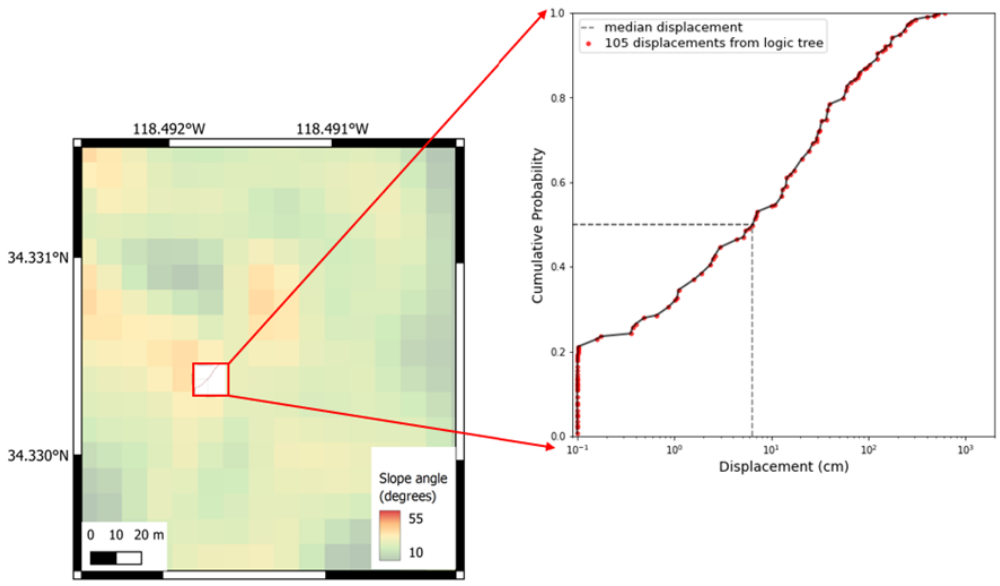

Figure 3.19. Example of slope map and CDF of 105 displacement values computed for a grid cell.

Figure 3.20 shows the CDF of k_y and displacement across the full logic tree for three different cells. These three cells were shaken by a similar ground motion intensity (M = 6.7, PGA = 0.82 g, and PGV = 98 cm/s) but the k_y distributions are different for each cell. The cell with the smallest values of k_y is associated with the largest displacements, and vice versa. Because of the epistemic uncertainty in k_y, the epistemic uncertainty associated with the different predictive displacement models, and the aleatory variability associated with the displacement predictions, the variability in the displacement associated with the CDF is substantial. The variability is smaller for the large k_y cell due to many of the displacements being associated with little/no displacement, but the variability is larger for the smaller k_y cell due to the large range of displacements predicted across the different values of k_y from the logic tree.

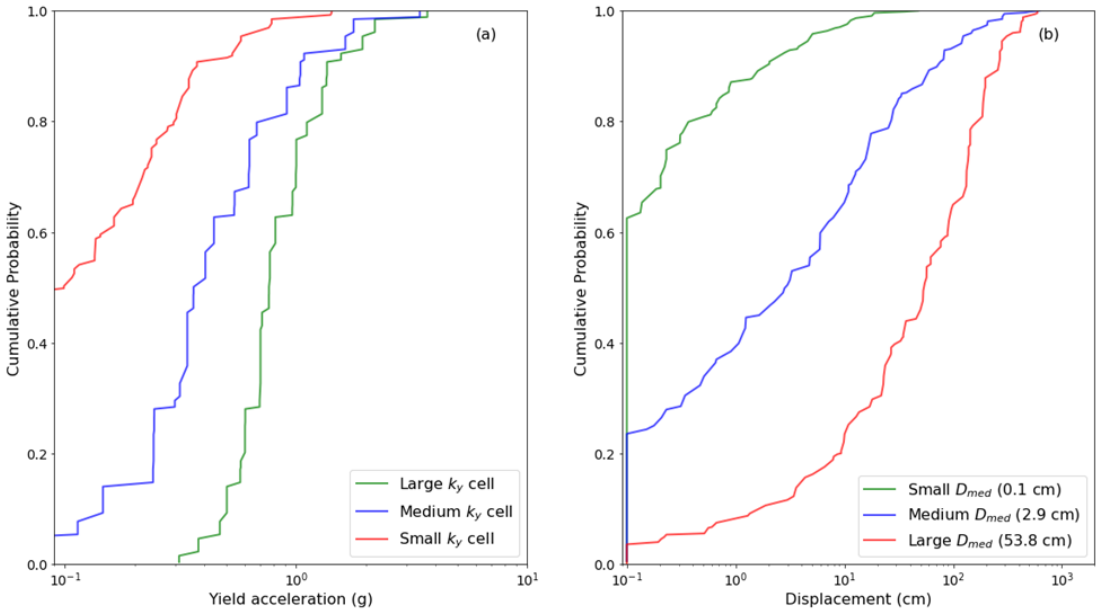

Figure 3.20: (a) k_y and (b) displacement CDFs for sample cells with small, medium and large displacement and M = 6.7, PGA = 0.82 g, and PGV = 98 cm/s).

3.6 Defining Landslide Zones and Attributes

3.6.1 Translating grid-level displacements into landslide zone polygons

Here we describe the approach used to define landslide zone polygons and their attributes (i.e., location, size, displacement, and direction) from the outcome of the cell-by-cell calculation of sliding displacement from the logic tree. These landslide attributes can be used to assess the risk to overlying infrastructure, such as pipelines. The general procedure for defining the landslide zone polygons is summarized in the flowchart shown in Figure 3.21. Additionally, we provide details on how we generated the slope units and finally, we illustrate how we computed probability mass functions for landslide sizes, displacement magnitude and direction.

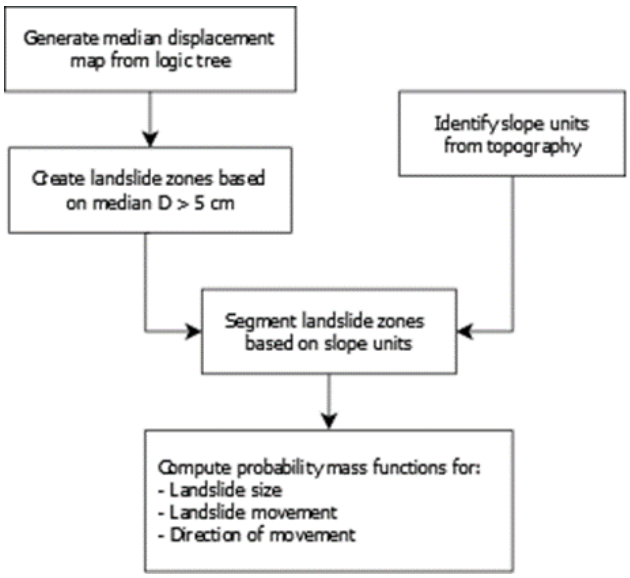

Figure 3.21. General procedure for defining landslide zone polygons and attributes

To demonstrate the procedure for defining these landslide zones, we examine a small study area in the Santa Susana mountains, north of San Fernando Valley in Southern California covering an area of about 2 km^2. Figure 3.22 shows the geologic map of the location of the study area which comprises mostly of Tertiary Sandstone, Tss.

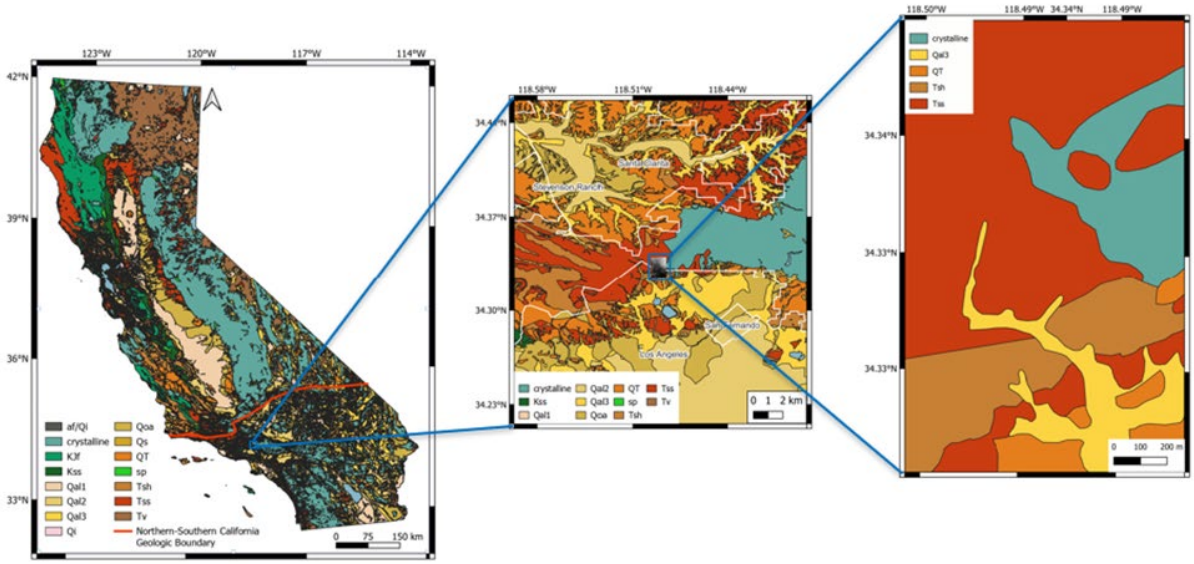

Figure 3.22. Geologic map of study area in the Santa Susana mountains, north of San Fernando Valley, Southern California

As shown in Figure 3.231, the first step in defining landslide zone polygons is to generate a seismic landslide displacement map for each ground motion scenario using the median sliding displacement (D_{med}) obtained from the displacement CDF for each grid cell. For the study area shown in Figure 3.22, a single map of D_{med} was generated using the logic tree approach described above and PGA and PGV values from the USGS ShakeMap (USGS, 2020) for the 1994 M6.7

Northridge event. Figure 3.23a is an illustration of the resulting D_{med} for each grid cell of the study area. Clusters of D_{med} that are susceptible to landslides are called landslide zones and these zones are created using a threshold on the median displacement, $D_{med,t}$, equal to 5 cm.

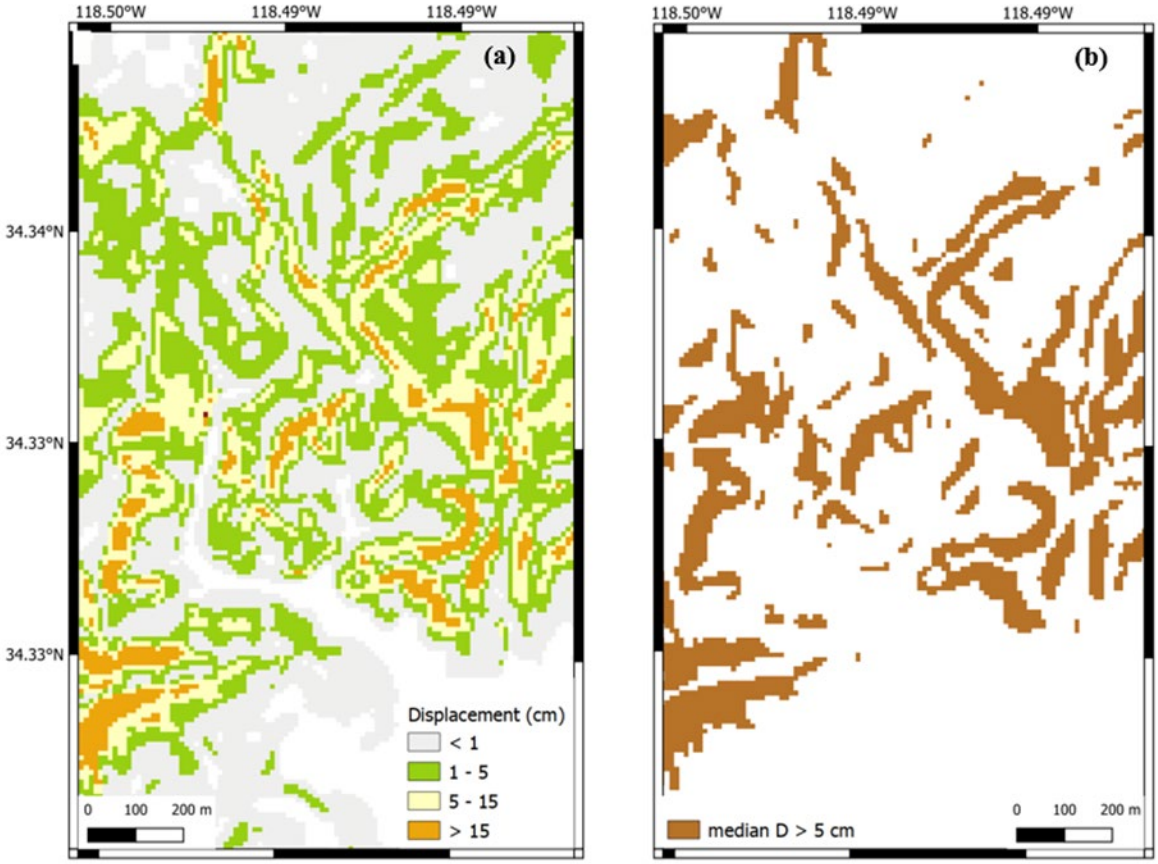

Figure 3.23. (a) Map of median displacement generated from logic tree analysis (b) landslide zones created using $D_{med,t}$ = 5 cm

Common displacement thresholds that have been used to define landslides hazards in the literature are 5, 15 and 30 cm (Nichols et al., 1997, Jibson and Michael, 2009, Dreyfus et al., 2013, Detweiler and Wein, 2017). The thresholds adopted by the CGS for the Oat Mountain quadrangle seismic hazard zoning program and Jibson et al. (2000) are presented in Table 3.5. This study uses $D_{med,t}$ = 5 cm to create the landslide zones (Figure 3.23b) because this value traditionally has been the threshold below which the landslide hazard is considered low/very low. The selected threshold delineates the zones of landslide susceptibility and a smaller $D_{med,t}$ will result in a larger total predicted landslide area and vice versa. From Figure 3.23b it is clear that aggregating grid cells with D > 5 cm can generate large landslide zones and these landslides zones are unlikely to fail as one large failure. Therefore, additional constraints are used to define the potential landslide regions.

Table 3.5. Landslide hazard potential ranking assigned from sliding displacements

CGS (Nichols et al., 1997)		Jibson and Michael (2009)		This study	
Sliding displacement (cm)	Landslide hazard potential	Sliding displacement (cm)	Landslide hazard potential	Sliding displacement (cm)	Landslide hazard potential
< 5 cm	Very low	0 – 1 cm	Low	0 – 5 cm	Low
5 – 15 cm	Low	1 – 5 cm	Moderate	5 – 30 cm	Moderate
15 – 30 cm	Moderate	5 – 15 cm	High	30 – 100 cm	High
> 30 cm	High	> 15 cm	Very high	> 100 cm	Very high

To resolve this issue of large landslide zones, slope units were generated to identify slopes that will move together as a unit and these units were used to partition the large landslide clusters into smaller polygons that represent the geomorphology of the terrain. These slope units were produced from the 10-m resolution DEM using the r.slopeunits software developed by Alvioli et al. (2016, 2020). The software is integrated into GRASS GIS and Python in a Linux environment. r.slopeunits takes the DEM and a number of user-defined parameters as the inputs and performs iterative functions using the r.watershed tool within GRASS GIS to create hydrological half-basins. The user-defined parameters include initial flow accumulation threshold area (t_f), minimum surface area (a_s), circular variance (c), and cleansize area (a_{cl}). The parameters a_s and c are the most important for slope unit partitioning because they control the size and direction of the resulting partitioned slope units. In this study, we used the following optimal parameters: t_f = 25,000 m^2, a_s = 1,000 m^2, c = 0.3 and a_{cl} = 1,000 m^2 based on our judgment of the resulting slope units. The software returns a raster file with slope units, which are then post-processed into a vector file format for landslide area segmentation.

Slope units generated in Southern California were more representative of the landforms when compared to Northern California. The topography of Northern California varies widely, including rugged coastal cliffs, dense forests, and high mountain ranges such as the Sierra Nevada and the Cascades. Southern California, on the other hand, is known for its deserts and beaches, as well as its many hills and mountains, including the Transverse Ranges and the Peninsular Ranges. Overall, Northern California tends to be more mountainous and forested, while Southern California is more arid and has more coastal and desert landscapes.

Figure 3.24 shows the slope unit segmentation process for the small study area. Figure 3.24a is the slope unit polygons defined from the slope unit analysis. These slope units are used to segment the landslide zones into smaller landslide zone polygons (LZP) that reflect the geomorphology of the area. Figure 3.24b shows the slope units overlain on the large landslide zones, and Figure 3.24c shows the resulting segmented LZP.

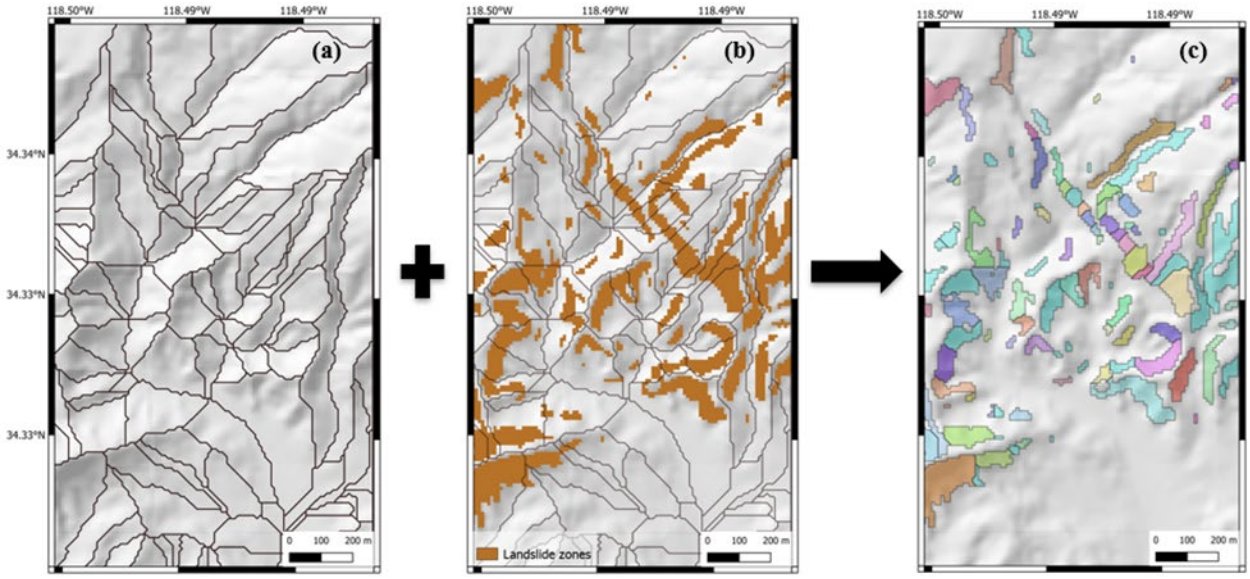

Figure 3.24. (a) Slope unit polygons generated from DEM using r.slopeunits software (b) Slope unit polygons overlain on landslide zones (c) Resulting segmented landslide zone polygons.

3.6.2 Distribution of landslide size

Figure 3.25 shows an example slope unit polygon with identified landslide zone polygons (LZP) within them. The occurrence of a landslide bigger than the LZP is considered improbable but a landslide smaller than the LZP may occur anywhere within the polygon. It is also possible that multiple LZP can be present in a single slope unit (Figure 3.25b), and for this study these LZPs will be treated separately.

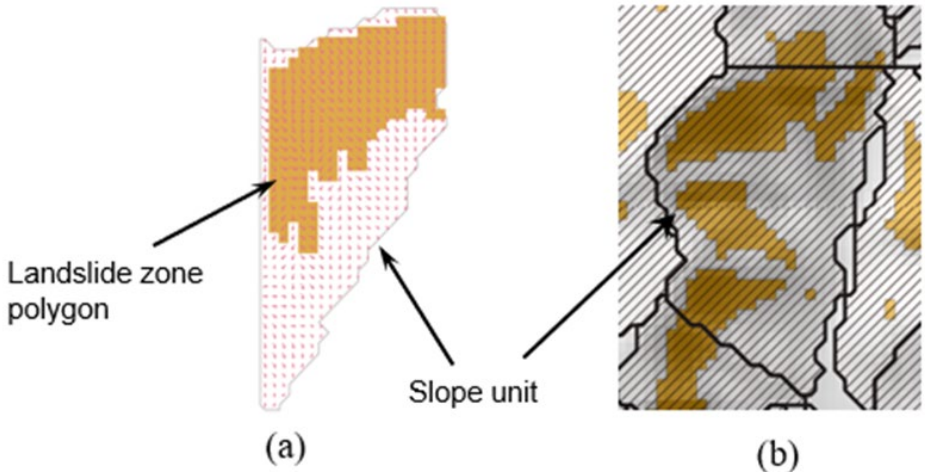

Figure 3.25. (a) LZP embedded within a slope unit (b) multiple LZP within a single slope unit

Many of the LZPs are much larger than typical landslide sizes as compared with empirical distributions from previous regional landslide events (Malamud et al., 2004, Guzetti et al., 2005, Keefer, 2013). To account for the statistical distribution of potential landslides within a LZP, the sizes of the landslides are defined with the empirical probability distribution described in Malamud et al. (2004).

Figure 3.26 shows the observed probability density of landslide areas for landslide inventories generated by the 1994 Northridge earthquake, the 1997 Umbria snowmelt, and the 1998 Hurricane Mitch rainfall events in Guatemala presented in Malamud et al. (2004). The plots follow an inverse Gamma distribution with a rollover at a landslide area of about 400 m^2 and a power law distribution at the tails.

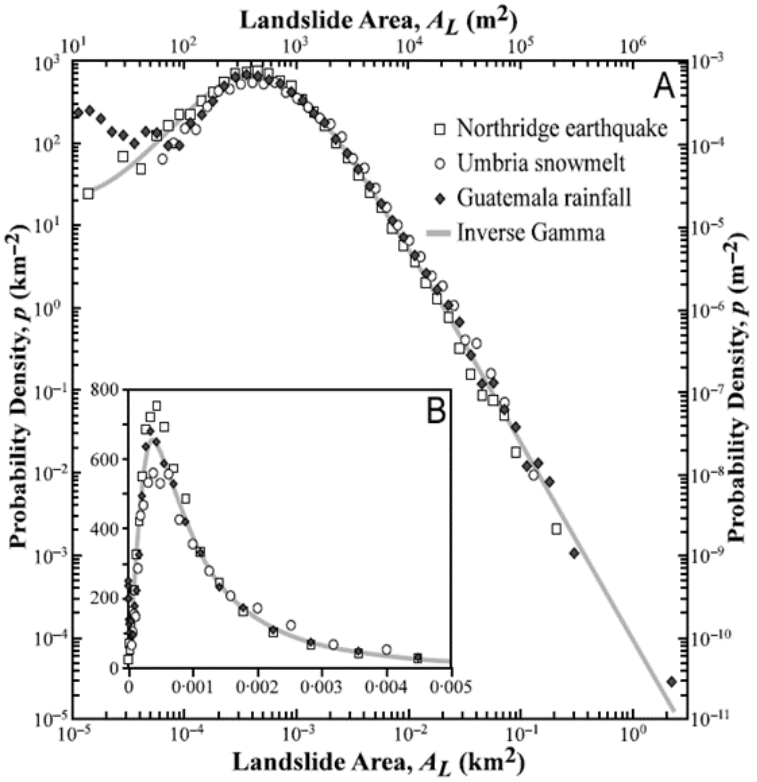

Figure 3.26. Landslide area probability densities for three landslide events plotted in log scale (A) and linear scale (B) (Malamud et al, 2004)

Malamud et al. (2004) developed a landslide area probability density function (PDF) for the observed landslide inventories as:

$$p(A_L;\rho,a,s) = \frac{1}{a\cdot\Gamma(\rho)}\left[\frac{a}{A_L-s}\right]^{\rho+1} exp\left[-\frac{a}{A_L-s}\right] \qquad (3.9)$$

where A_L is the landslide area, ρ is the parameter controlling power-law decay, a controls the location of maximum probability, s controls the exponential rollover for small landslides, and Γ(ρ) is the gamma function. Malamud et al. (2004) assumed that all landslide events should have the same mean landslide area and found that the parameters ρ = 1.4, a = 1.28 x 10-3 km^2, and s = -

1.32 x 10-4 km^2 fit all three inventories. They decided that the landslide area PDF and associated parameters can be applied to other landslide-event inventories with minimal error because the distribution is independent of the number of landslides associated with an event.

The landslide area PDF was used to identify the percentage of landslides expected in five different landslide area bins shown in Table 3.6. These area bins represent ranges associated with pipeline fragility curves that define the damage to the pipe based on the length of the pipe subjected to movement. These landslides areas represent a square area associated with the pipe lengths associated with the fragility curves (i.e., 10, 50, 100, 200, and 500 m), and are computed as the square of the pipe lengths (10 m pile length is associated with 100 m^2 landslide area). A significant percentage (~ 77%) of landslides are associated with the 100 – 2,500 m^2 area bin (10 to 50 m pipe length exposed), while the second largest bin is 2,500 – 10,000 m^2 (50 to 100 m pile length exposed) with ~18%. For some of the LZPs in this study, the landslide areas were less than 100 m^2 (the size of one 10 m-grid cell) due to remnants from the slope unit delineation. These small landslide areas were not considered LZPs in this study.

Table 3.6. Probability of different landslide area sizes from empirical distribution.

Area Bins (m^2)	Area Bins (km^2)	Probability
< 100	< 0.0001	0.9%
100 – 2500	0.0001 – 0.0025	76.8%
2,500 – 10,000	0.0025 – 0.01	18.2%
10,000 – 40,000	0.01 – 0.04	3.5%
> 40,000	> 0.04	0.6%

The probabilities in Table 3.6 serve as the starting point for the estimation of our landslide size probability mass function (PMF). However, because landslides cannot be larger than the LZP, the empirical distribution is truncated at the bin associated with the size of the LZP and normalized to achieve a total probability of 1.0. This process is outlined in Figure 3.27.

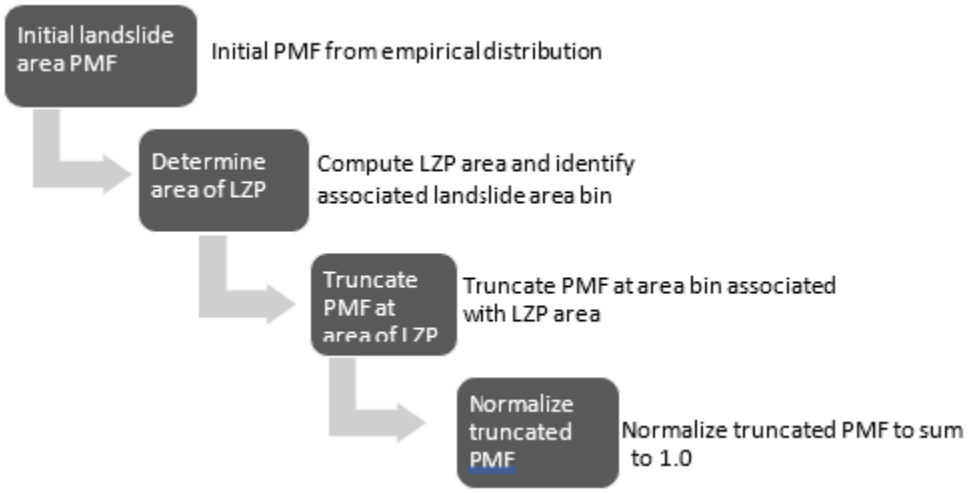

Figure 3.27. Procedure for assigning the probability distribution to landslide size for a LZP

Figure 3.28a shows an example of the truncated empirical distribution based on an LZP with a size of 7,500 m^2. This size of LZP results in truncating the last two area bins as listed in Table 3.6, which generates a slight increase in the probabilities associated with the smaller landslide area bins as shown in Figure 3.28b.

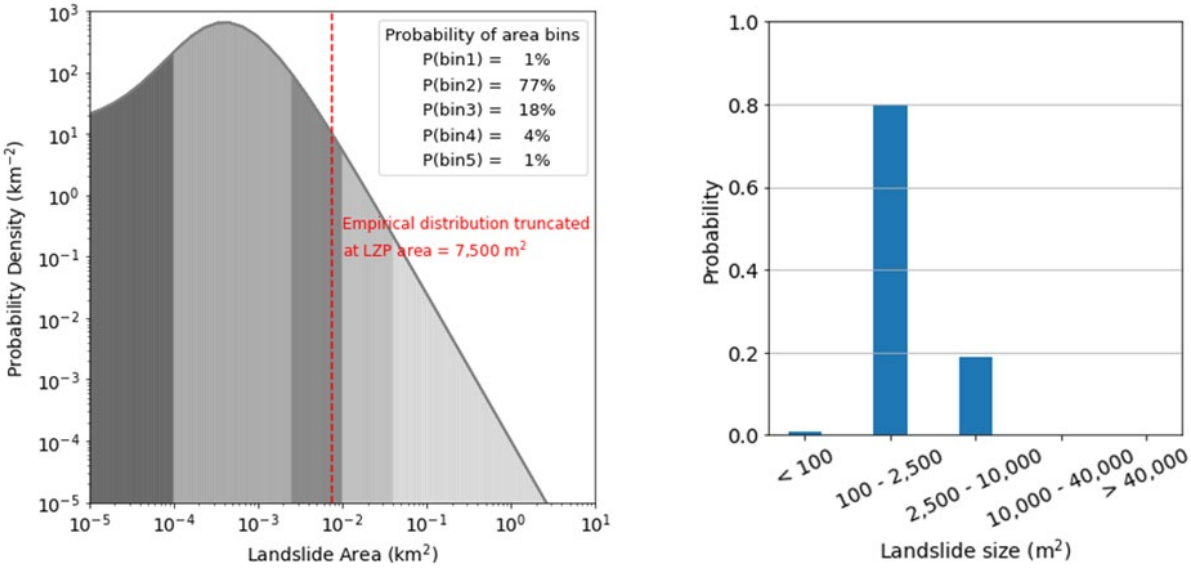

Figure 3.28: (a) Empirical probability density function for landslide size truncated at size of landslide zone (b) Resulting PMF for landslide size.

3.6.3 Distribution of landslide movement

In addition to the PMF for the landslide area, we estimate the PMF for displacement movement for each LZP using the 105 displacement values per grid cell computed for all grid cells within the LZP. First, the displacement distributions are aggregated across the grid cells to determine the combined CDF for the LZP. This aggregation is done by pooling all displacements for every cell within the LZP and applying their individual weights to compute the CDF. Figure 3.29 shows the combined CDF of displacements along with the CDF for individual cells for two different LZP. Figure 3.29a shows the displacements for a small LZP with five cells (LZP1), while Figure 3.29b shows displacement for a larger LZP with 220 cells (LZP2).

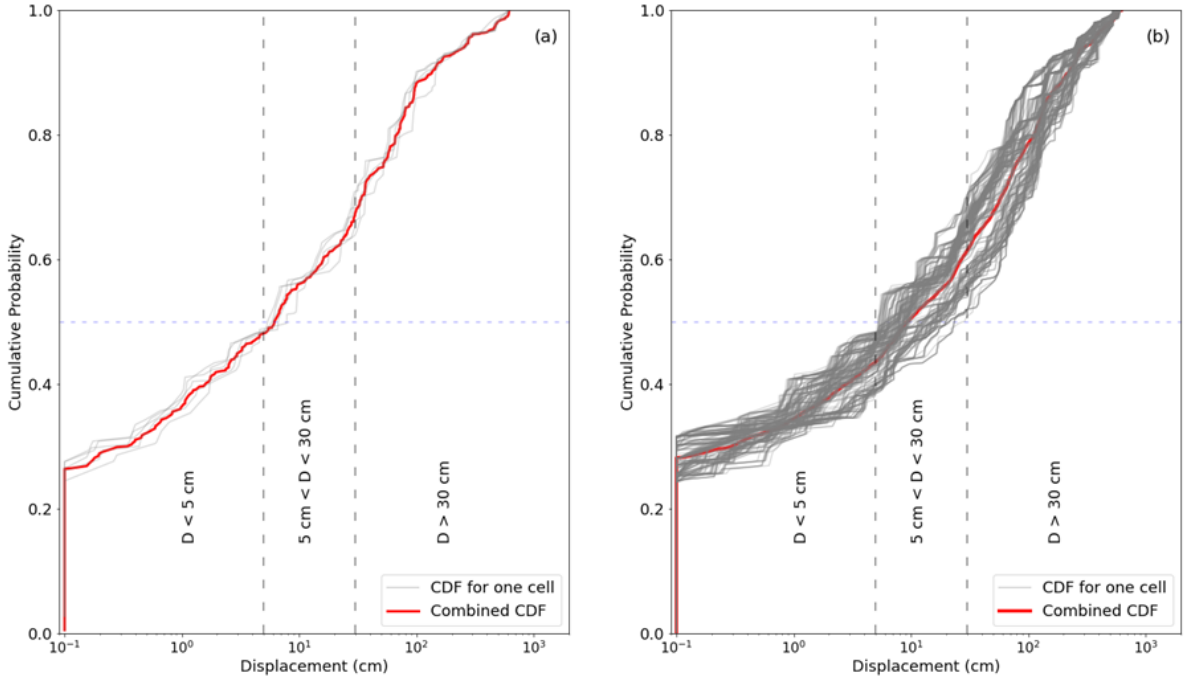

Figure 3.29. Combined CDF of displacements from all cells for two example LZPs. (a) LZP1 with five grid cells and (b) LZP2 with 220 grid cells.

An important issue to address is the relationship between the displacements, D, computed by the sliding block analysis and the expected ground movements that may affect a pipeline. Traditionally, the sliding displacements have been used as an index of seismic performance, where larger D values are associated with a larger likelihood of a landslide and larger movements. However, the value of D is not directly equal to the movement in the field, yet the fragility functions for pipeline performance require estimates of movement associated with the landslide. The bins of movement for the pipeline fragility functions are listed in Table 3.7 and extend between 0-30 cm and > 900 cm. We consider the 0-30 cm movement bin to represent no/low landslide hazard and thus the probability of this bin is assigned the CDF for D = 5 cm (i.e., probability D < 5 cm). We consider the 30 - 150 cm bin to represent moderate movement and assign to it the probability for D = 5 – 30 cm. The probabilities for D > 30 cm are more difficult to translate to landslide movements. Thus, the four largest bins of landslide movements are assigned probabilities

proportional to $D^{-0.5}$, with the constraint that the sum of all of the probabilities for the four bins are equal to 1 – CDF (D = 30 cm). This constraint ensures that the PMF for landslide movement sums to 1.0.

Table 3.7. Approach used to assign PMF to landslide movement bins using CDF for sliding displacement

Landslide Movement (cm)	Probability
0-30	CDF (D = 5 cm)
30-150	CDF (D = 30 cm) – CDF (D = 5 cm)
150-300 300-600 600-900 > 900	$\propto D^{-0.5}$

Figure 3.30 shows the resulting PMF for landslide movement for the two LZPs referred to in Figure 3.29. LZP1 has higher probabilities for the first two bins corresponding to low or moderate landslide hazard while LZP2 has higher probabilities in the last four bins corresponding to higher landslide hazards. This behavior supports the notion that smaller landslides are associated with low to moderate damage while large landslides are expected to cause more damage to structures.

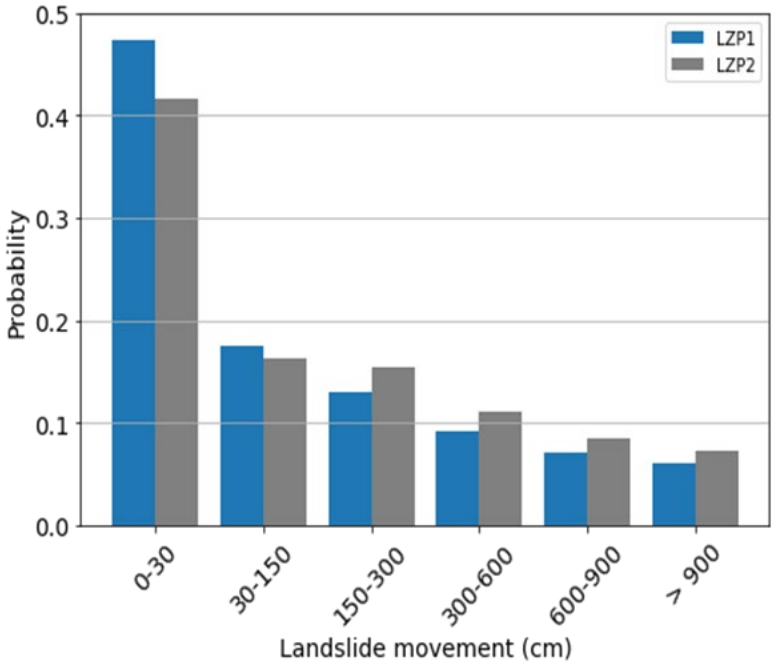

Figure 3.30. PMF of landslide movement for examples landslide zone polygons LZP1 and LZP2

3.6.4 Distribution of landslide movement direction

The final attribute required of a landslide is its direction of movement, which is used in the pipeline fragility functions to define the direction of landslide movement relative to the alignment of the pipeline. The DEM can be used to define this information. The slope angle represents the inclination of the face of the slope to the horizontal, while the slope aspect represents the direction the slope is facing, with North defined as 0°. The slope aspect gives an indication of the direction of the potential downward movement of the slope. Figure 3.31 is a map of the slope aspect for the small study area being considered in the Santa Susana mountains north of San Fernando Valley, which shows that the aspect can be quite variable over a study area.

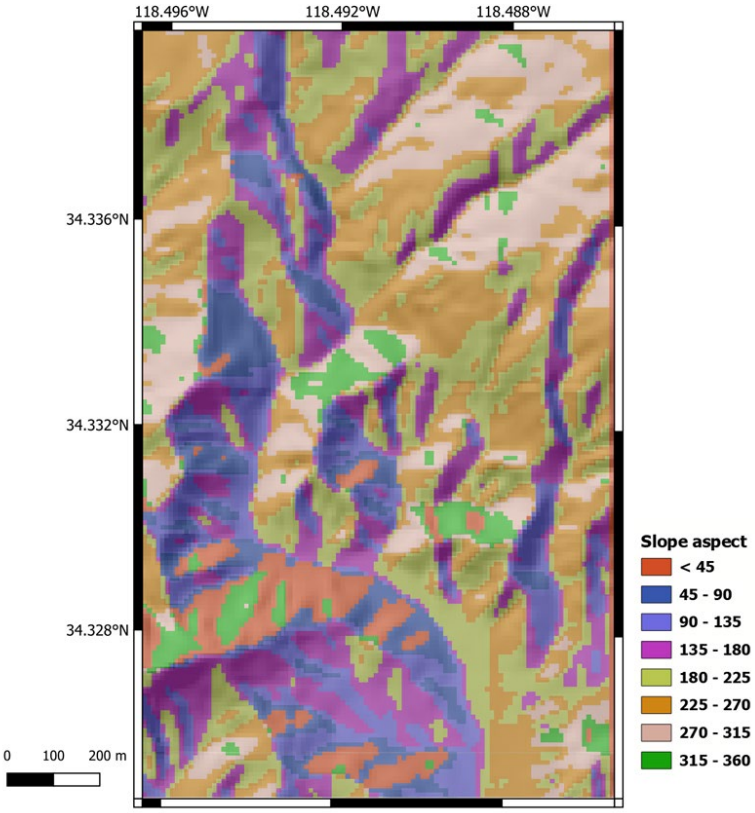

Figure 3.31. Aspect map overlain on elevation map for study area

For each LZP, the slope aspect values are aggregated across the grid cells to compute the combined direction CDF for the LZP. This aggregation is done by pooling slope aspects for every cell within the LZP and assuming equal weights for all cells. The aspect values are then discretized into 5 bins to generate the PMF for landslide movement direction for angles between 0 to 360°. The PMF is completely driven by the slope aspect generated from the DEM within the LZP and the probabilities can vary substantially with direction. Figure 3.32 shows an example LZP within a slope unit where the arrows indicate the direction of movement for each cell.

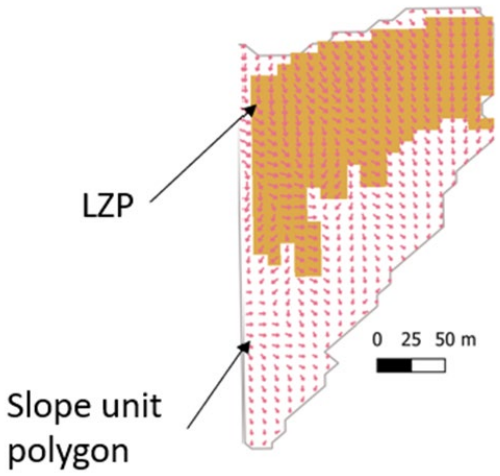

Figure 3.32. Example of LZP within slope polygons showing slope aspect representing direction of movement for each grid cell

Figure 3.33 shows the resulting PMF for the direction of landslide movement after aggregating the slope aspect for all cells within the LZP shown in Figure 3.32. As noted in Figure 3.33, the direction of movement for the LZP is very variable, but there is a high probability that the landslide will move in the SE downslope direction as most values fall within 120º - 175º.

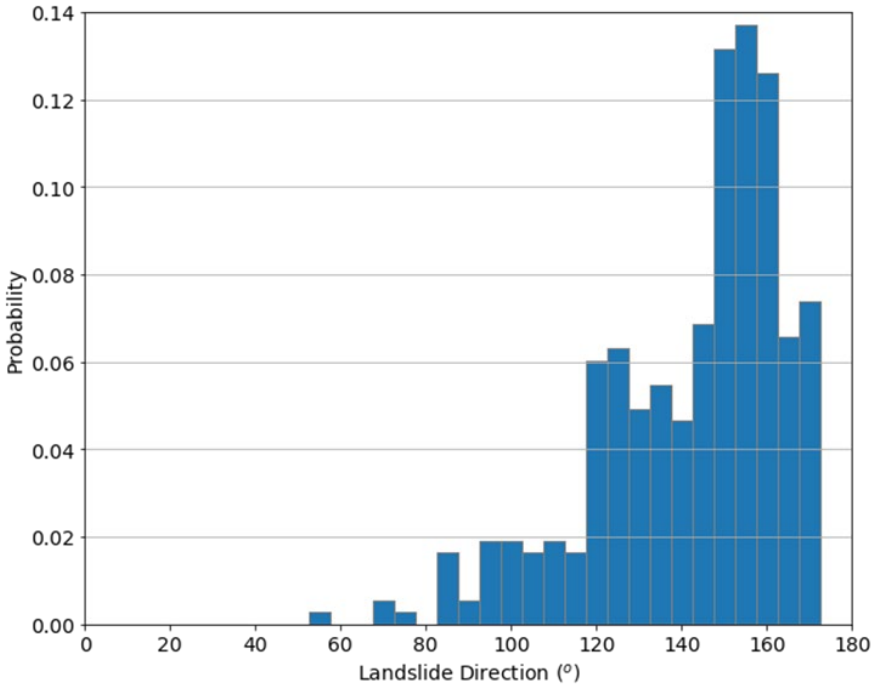

Figure 3.33. PMF of landslide direction generated from aggregating slope aspect for each grid cell within an LZP

4 Liquefaction Hazard

In this section, we describe our logic tree-based approach to estimating liquefaction-induced ground deformations on a regional scale. We developed this approach to predict such deformations at any location in the state of California using, among others, methodologies developed for liquefaction susceptibility and triggering on a site-specific scale. The first portion of the logic tree focuses on inferring the subsurface conditions and water table depth based on regionally-available data and accounts for epistemic uncertainty arising from a lack of site-specific information. The second portion of the logic tree uses the inferred subsurface conditions to perform susceptibility, triggering, and deformation analysis using a suite of probabilistic models from the literature. Figure 4.1 provides a schematic description of the layers in the logic tree.

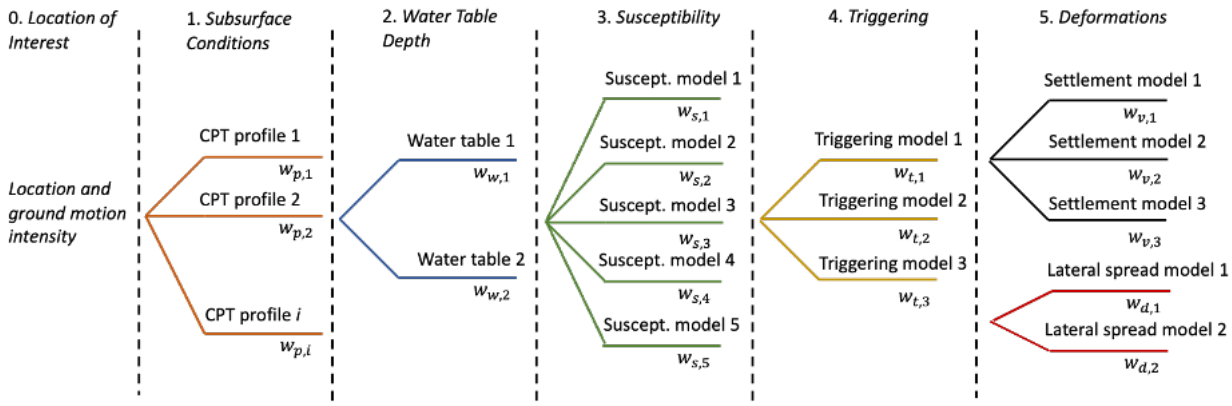

Figure 4.1. Schematic description of the layers in the logic tree presented in this study. Each branch in each layer is assigned a weight, denoted as *w*.

4.1 Epistemic Uncertainty

4.1.1 Inference of Cone Penetration Test Results

Available methods for liquefaction susceptibility, triggering, and deformation analysis use cone penetration test (CPT) results as inputs. The CPT data was non-uniformly distributed across the state (see Chapter 2), so we needed to develop a methodology for regional liquefaction displacement probabilities that was applicable to sites that did not have CPT measurements. We resolved this issue by using clustering to determine typical profiles from a database of CPTs divided by geologic unit; representing the typical profiles by means of CPT random fields; and

weighting the typical profile likelihood at each grid point based on the time-averaged shear wave velocity in the top 30 m (Vs30) (measured or calculated using proxy-based procedures) at a given location by means of maximum likelihood estimation.

We begin with a database of CPT soundings in California that were collected by the USGS (2020) and a state geologic map (Wills et al, 2015). The location of available CPT soundings across the state of California and their availability within the various geologic units are described in Chapter 2. We consider the following geologic units to be relevant to liquefaction risk analysis: quaternary (Holocene) alluvium for three slope categories (Q_{al1}, Q_{al2}, and Q_{al3}); quaternary (Pleistocene) alluvium (Q_{oa}); and artificial fill over intertidal mud (af/Q_i). The CPTs for each relevant geologic unit are grouped using hierarchical clustering. The typical CPT profiles for that geologic unit are the mean q_c and f_s each of its clusters. Clustering is performed with the definition of the "distance" between CPT soundings i and j being the mean squared error between those CPTs' q_c and f_S profiles added together:

$$\Delta q_{ij} = \sqrt{\frac{1}{n}\sum_{z=1}^{n}\left(q_i(z) - q_j(z)\right)^2}$$

$$\Delta f_{ij} = \sqrt{\frac{1}{n}\sum_{z=1}^{n}\left(f_i(z) - f_j(z)\right)^2}$$

$$\Delta_{ij} = \Delta q_{ij} + \Delta f_{ij}$$

Multinomial regression is then performed on the observed CPTs to estimate the probability of being it in a given cluster conditioned on $V_{s,30}$. Figure 4.2 depicts the clustering model for Qal1, namely the statistical distribution of CPTs belonging to one of the typical profiles within geologic unit Qal1 in Northern California (entry 3 in Table 1, NorCal). Figure 4.3 next plots the multinomial distribution for assigning weights as a function of Vs30 for typical profiles in NorCal1.

Table 4.1. CPT groups we selected according to geologic unit and location. The table summarizes the well-represented units that were kept in our analyses.

Geologic Unit	Abbreviation	Location	Number of CPTs
Artificial fill over intertidal mud	af/Qi	NorCal	99
Quaternary (H) alluvium (slope <0.5%)	Qal1	SoCal	149
Quaternary (H) alluvium (slope <0.5%)	Qal1	NorCal	184
Quaternary (H) alluvium (0.5% < slope < 2.0%)	Qal2	SoCal	180
Quaternary (H) alluvium (0.5% < slope < 2.0%)	Qal2	NorCal	176
Quaternary (H) alluvium (2.0% < slope)	Qal3	SoCal	81
Quaternary (H) alluvium (2.0% < slope)	Qal3	NorCal	65
Intertidal mud	Qi	NorCal	6
Quaternary (P) alluvium	Qoa	SoCal	11
Quaternary (P) alluvium	Qoa	NorCal	34
Quaternary (P) sand deposits	Qs	NorCal	27

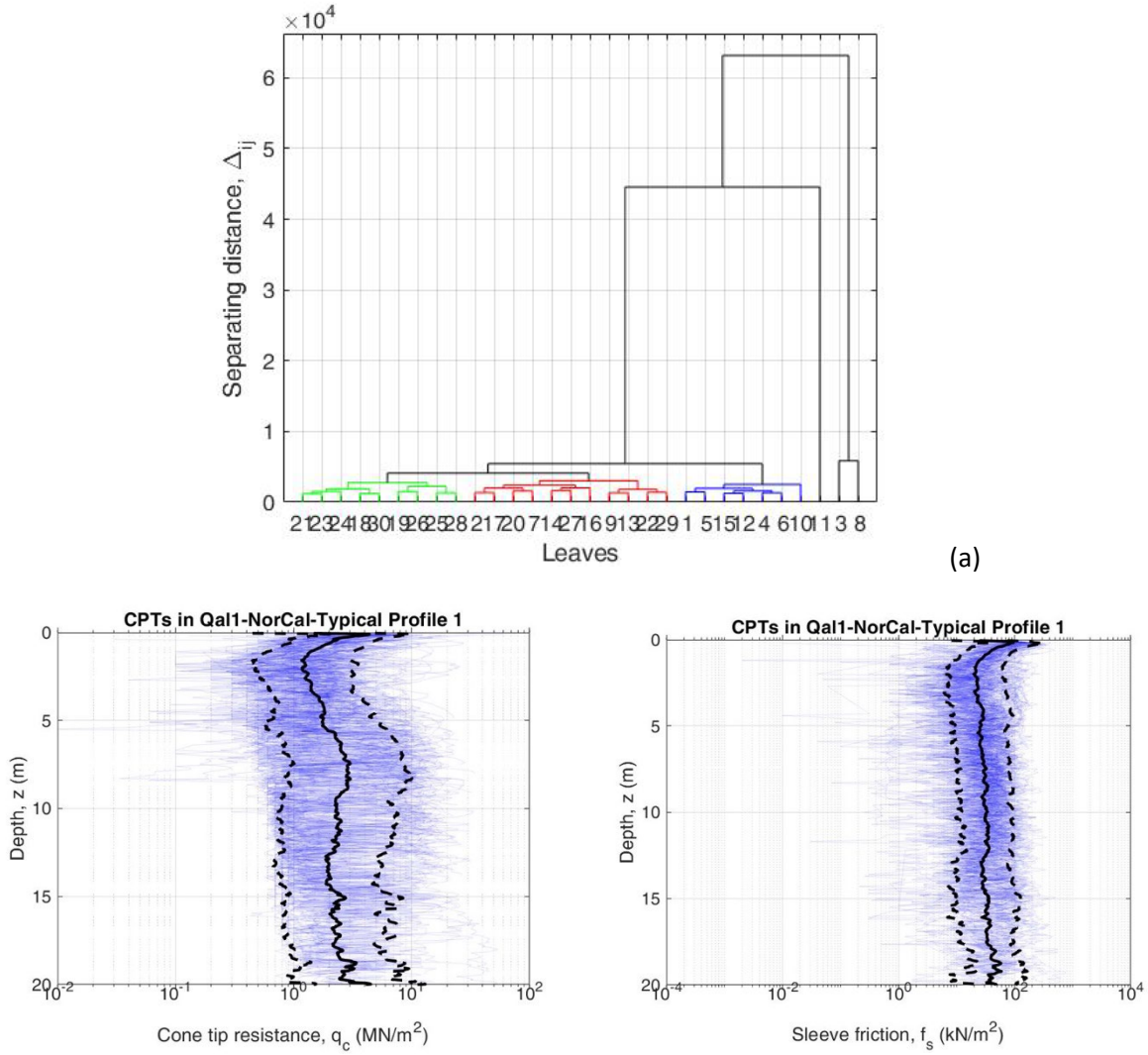

Figure 4.2. (a) Dendrogram showing the clustering of three typical profiles characterizing Q_{al1}-NorCal and (b) statistics of CPT measurements for tip resistance, q_c (left) and sleeve friction, fs (right), representative of typical profile 1 of Q_{al1}-NorCal.

In each CPT cluster of each geologic unit, we determined the necessary parameters needed for random field representation of the CPT profiles. These include the trends in q_c (tip resistance) and f_s (sleeve friction) with depth, namely the spatial autocorrelation in q_c, the spatial autocorrelation in fs and the cross correlation between q_c and f_s as a function of depth. The random field representation of each typical profile was then used to draw representative CPT profiles within geologic units across the state. The conditional probability of each typical profile was based on estimating V_{s30} for each CPT as follows: (i) using the geometric mean of Hegazy & Mayne (1995), Piratheepan (2002), and Mayne (2006); and successively (ii) using multinomial regression to get probabilities of each profile within a given unit as a function of V_{s30}. The multinomial model for assigning weights to typical profiles in Qal1 as a function of V_{s30} is shown in Figure 4.3.

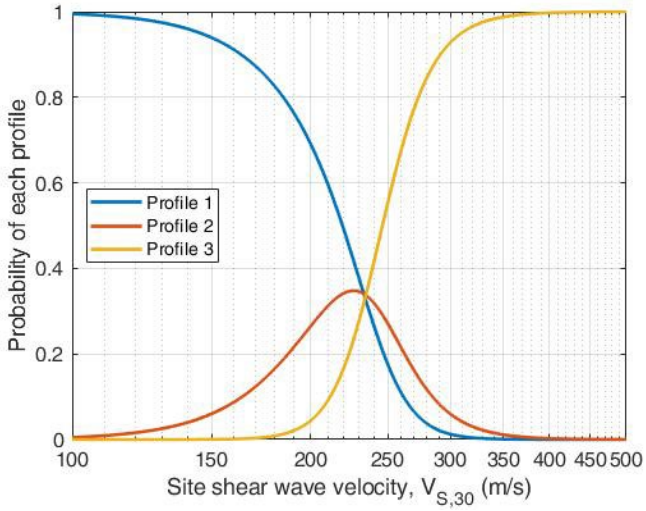

Figure 4.3 Multinomial model plot for assigning weights to the three typical profiles characteristic of Q_{al1}-NorCal shown in Figure 4.2, as a function of Vs30.

4.1.2 Inference of the Water Table Depth

In addition to the availability of CPT profiles, liquefaction analyses also require water table depth (*wtd*) to estimate the total and effective stresses. The second layer of the logic tree combines two estimates of *wtd*. The first estimate comes from the well recordings described in Chapter 2 (GAMA, 2020). We use only recordings made since January 1st, 2000, give greater weight to more recent recordings, and apply spatial interpolation (kriging) of the data to estimate the *wtd* at a given point. Because the well data are not evenly distributed across the state, we complemented the well *wtd* estimates with the global water table model by Fan et al (2013). This model can be applied globally and was previously used for regional liquefaction risk analysis by Zhu et al (2017).

We next checked for consistency of the two estimates at the locations of the wells. For this, we defined the following variables:

$z_{w,w}(t)$: depth to water table at a well at time t
$\bar{z}_{w,w}$: depth to water table at a well averaged over time
$z_{w,g}$: depth to water table given by Fan et al. (2013) global model
ε_w : log residual between $\bar{z}_{w,w}$ and $z_{w,g}$

Further, we defined the depth to water table at a given well averaged over time, as the weighted average of observations made since 1999, namely:

$$w(t) = (\text{year}(t) - 1999)/20$$

$$\bar{z}_{w,w} = \sum_t w(t) * z_{w,w}(t) / \sum_t w(t)$$

And finally, we defined the residuals of the two estimates in natural log units as follows:

$$\varepsilon_w = \ln(\bar{z}_{w,w}) - \ln(z_{w,g})$$

The histogram of the residuals is shown in Figure 4.4. The figure shows that the well-based *wtd* is systematically deeper than the estimate of the global water model, and that it is highly variable.

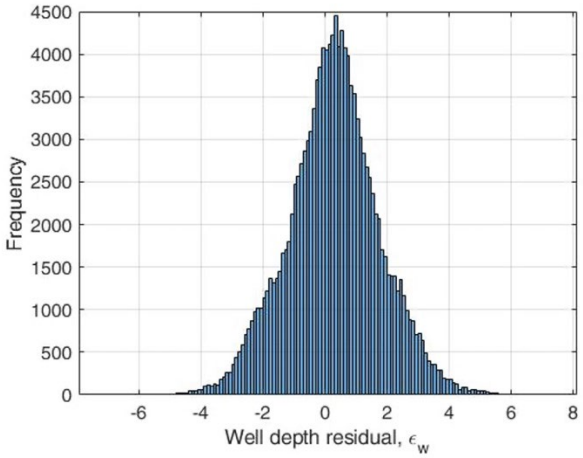

Figure 4.4. Histogram of residuals between the two wtd models, with mean 0.3 (factor of 1.35) and standard deviation 1.5 (factor of 4.5)

We further explored the inconsistency between the two models, and observed the spatial trends depicted in Figure 4.5 In the figure, positive numbers indicate that the well-based *wtd* is deeper than expected, and negative numbers indicate that the well-based *wtd* is shallower than expected. We first explored the possibility that the difference could be explained by considering the geologic units of the well locations. However, there was no systematic bias that we observed for the geologic units that we considered to be susceptible to liquefaction.

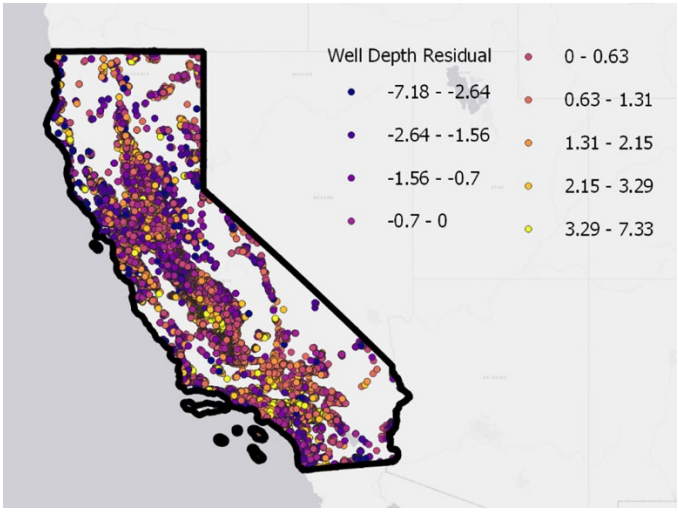

Figure 4.5. Systematic spatial trends of water table depth residuals between the wells and the global water table model in California

We then traced the systematic inconsistencies between wells-based and the global models to the land use, which is depicted in Figure 4.6 using data from the California Farmland Mapping and Monitoring Program. Dividing land use into three broad categories, Urban, Farmland and Other (see Table 4.2), we evaluated the mean and standard deviation of well depth residuals, and assigning land use across the state, we used the residuals to correct the global water model across the state.

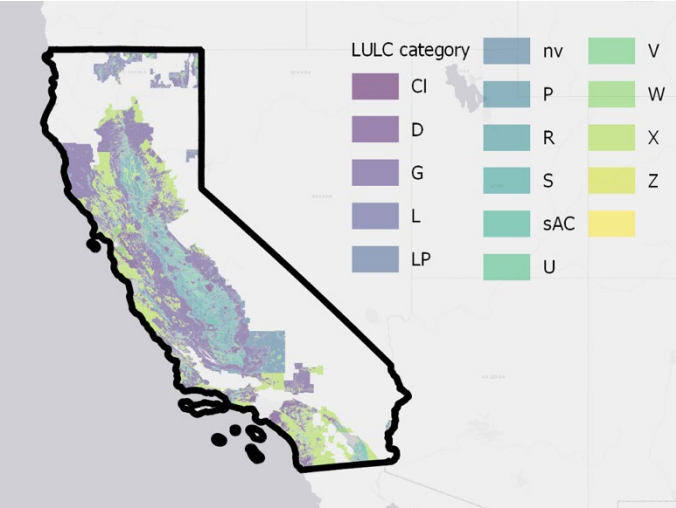

Figure 4.6. Distribution of land use from the California Farmland Mapping & Monitoring Program

Table 4.2. Well depth residuals by land use category

Group	Well Depth Residual Mean	Well Depth Residual Standard Deviation	Number of Wells
Urban	0.325	1.40	111,144
Farmland	0.526	1.52	9,103
Other	-0.012 ~ 0	1.70	16,840

The estimates of the well-based and corrected global water model were assigned weights depending on the number of wells near a given location. Specifically, weights were assigned depending on the number of wells within one correlation length away from the grid point of interest. The semi- variogram derived from the well depth residuals that was used to estimate the correlation structure of the well spatial distribution is shown in Figure 4.7a below. Based on the semivariogram, the correlation length is 33 km. The weights that we implemented in the second layer of the logic tree are shown in Figure 4.7b.

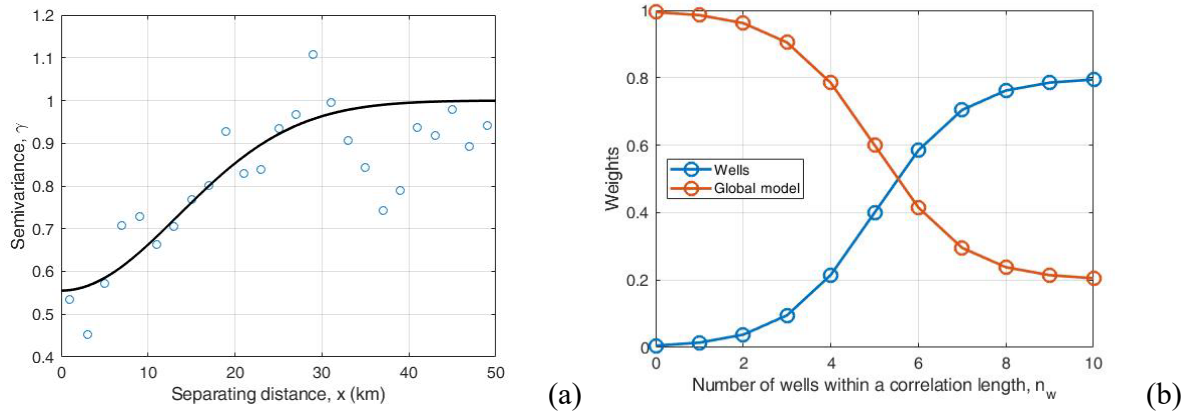

Figure 4.7. (a) Semivariogram of spatial distribution of water wells; (b) logic tree weights of the two *wtd* models (well-based and global) based on the number of wells within a correlation length from a given grid point

4.2 Susceptibility, Triggering, and Deformation Analysis

For any given CPT profile (i.e., any set of correlated *qc* and *fs* as functions of depth drawn from the random field CPT statistics described above) and a given *wtd* (estimated from the global model or evaluated on the basis of available well measurements), we perform susceptibility, triggering, and deformation analyses, which are reflected in the third, fourth, and fifth layers in the logic tree.

Most criteria for soil liquefaction susceptibility are based on Atterberg limits, which we could not infer from CPT and they are not available regionally. Instead, we opted in using only models based on soil behavior index (*Ic*). Developing the relevant profile properties for each CPT-*wtd* leaf of the logic tree involves the following steps:

- Calculate *Ic*.
- Estimate fines content from the CPT (Robertson & Wride (1998), Idriss & Boulanger (2008) and Yi (2014)).
- Calculate q_{c1N} and $q_{c1N,cs}$.
- Estimate median grain size from CPT (Douglas & Olsen, 1981)
- Estimate N_1 from q (Kulhawy & Mayne (1990), Lunne et al. (2002), Robertson (2012))
- Calculate $N_{1,60}$ and $N_{1,60,cs}$

Layer 3, the susceptibility layer of our logic tree, has five branches. On the first branch, the probability that the soil at a given depth is susceptible is 100% if $Ic \leq 2.6$ and 0% otherwise, according to Robertson (2009). The probability of susceptibility on the remaining branches is determined using Maurer's (2017) logistic models based on *Ic*, namely Polito (2001), Seed et al. (2003), Bray and Sancio (2006), Boulanger and Idriss (2006). The ensemble of 5 models used in our logic tree for liquefaction susceptibility are shown in Figure 4.8.

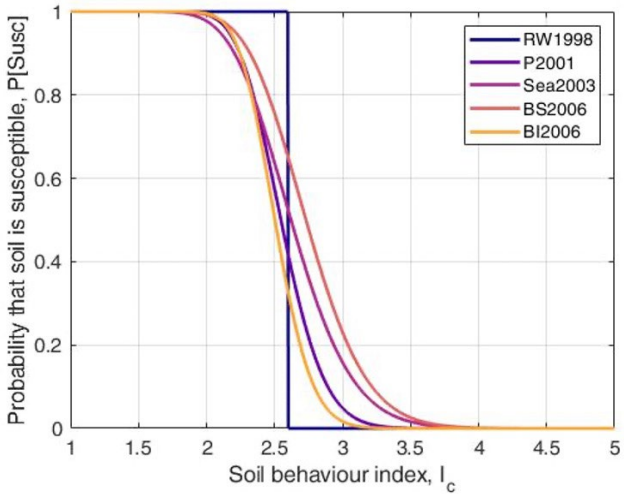

Figure 4.8. Liquefaction susceptibility of the five models implemented in our liquefaction logic tree as a function of the soil behavior index, Ic.

Triggering analysis in layer 4 yields a factor of safety against liquefaction (FSliq) that is used as an input in deformation analysis. We apply three models for FS_liq (Robertson and Wride, 1998; Moss et al (2006); and Boulanger and Idriss (2016). Standard deviations of Moss et al (2006) and Boulanger and Idriss (2016) are 0.22 and 0.2 correspondingly. We assigned to Robertson and Wride (1998) the mean standard deviation of the two other models, namely 0.21.

In layer 5, we applied three models for settlement-type deformations for each CPT-wtd leaf: Zhang et al (2002); Cetin et al (2009); and Juang et al (2013). Cetin et al (2009) has built-in uncertainty and the uncertainty of Juang et al (2013) is estimated on the basis of the uncertainty for Zhang et al (2002) with adjustments. We thus used the unadjusted uncertainty of Juang et al (2013) for Zhang et al (2002). In layer 5, we also applied two models for lateral spread-type deformations, applicable for sites steeper than 1% slope: Youd et al (2002) and Zhang et al (2004). An example of the distribution of settlement and lateral spread for a site located on 2% slope, evaluated as a function of PGA and associated uncertainty is shown in Figure 4.9.

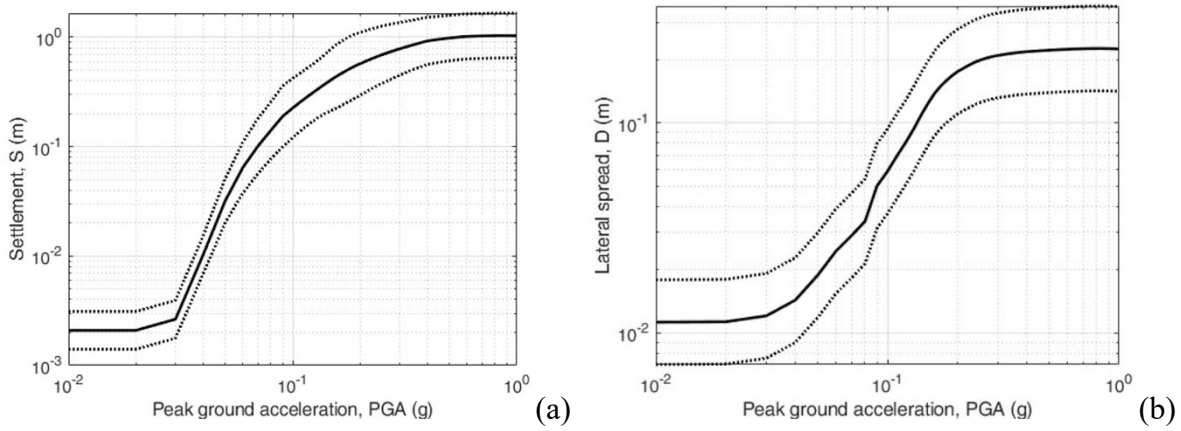

Figure 4.9. Settlement and lateral spread distribution as a function of PGA estimated at a site in a geologic unit with 3 characteristic profiles.

We optimized computational efficiency by: (a) restricting implementation of the liquefaction logic tree to susceptible units across the state, namely to areas with potentially-susceptible geologic formations (Table 1) and shallow water table estimates (wtd < 10m); (b) precomputing branches of the logic tree on a fine grid of subsurface conditions, water table depth and intensity measures, and interpolating thereafter. Still, branch levels for subsurface conditions and water table depth from wells are not linearly related and require Monte Carlo simulations to obtain samples of representative profiles within geologic units and water table maps using kriging. On the other hand, these calculations are independent of intensity, and can be performed once and saved for use in any number of ground motion scenarios.

Lastly, in its current form, the logic tree combines probability distribution functions (PDF) of probabilistic branches with probability mass functions (PMF) of deterministic branches. A more rigorous way to estimate uncertainty would be to treat the deterministic branches as samples, converting them into a single distribution using maximum likelihood estimation, and then combining them with the probabilistic branches. This task was considered outside the scope of this project. The flow chart in Figure 4.10 summarizes the development of tools and algorithms involved in the estimation of liquefaction displacement distributions, along with the steps where we drew models and methodologies from the literature. Finally, Figure 4.10 shows a schematic representation of the liquefaction displacement logic tree.

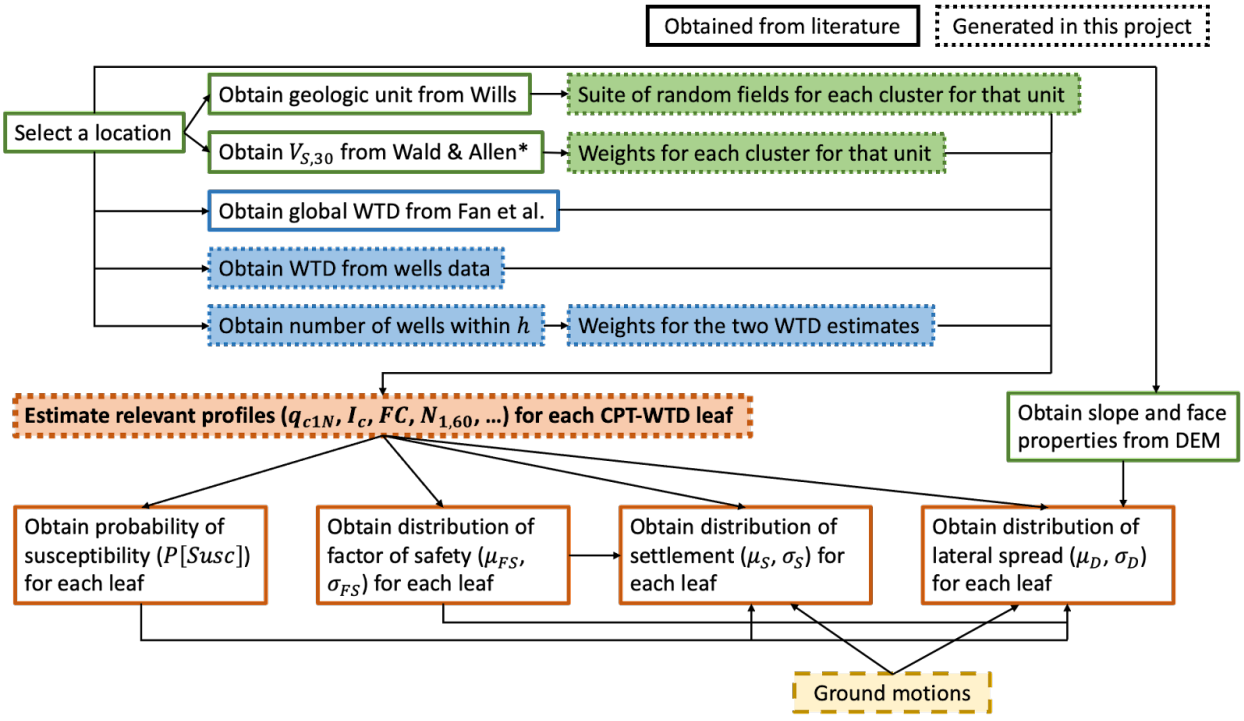

Figure 4.10. Flow chart indicating the development of algorithms and methods involved in the liquefaction displacement estimation on a regional scale.

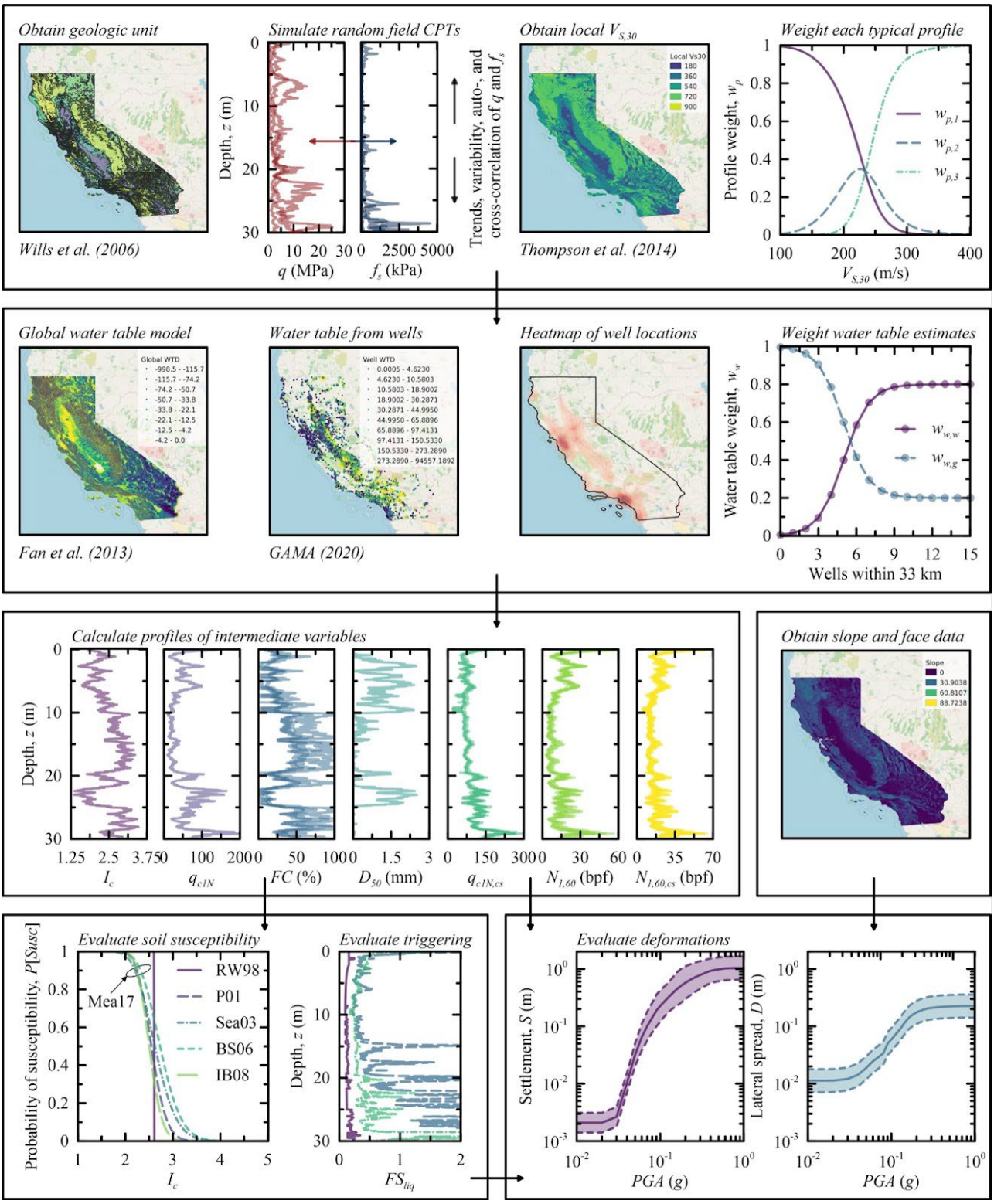

Figure 4.11. Schematic representation of the liquefaction ground displacement logic tree

4.3 Geospatial distribution of liquefaction manifestation

The logic tree-based approach described above can yield similar estimates of displacement across large areas of consistent surface geology, water table depth, and ground motion intensity. Applying the logic tree across ground motion scenario maps may therefore overestimate the area that would be affected by liquefaction-induced displacements and provide features of unreasonably large size. Recently, Greenfield and Grant (2020) used Gaussian fields to map site-specific observations into 3D independent random fields of groundwater depth, soil plasticity, and penetration resistance for different geologic units, and integrated the resulting models in a regional-scale probabilistic framework for liquefaction triggering. Still, their approach requires statistically significant site characterization data, which is rarely available on regional scales.

On the opposite length scale end, geospatial proxies for liquefaction hazard (e.g., Zhu et al. (2015, 2017), Rashidian and Baise (2020)) provide an alternative tool for regional liquefaction risk assessment that uses inputs available from remote sensing, such as the topography at a given location, to predict the probability that a specific location will be affected by liquefaction (P_{liq}). Such proxies may still require inference of certain inputs or estimation using global models (e.g., *wtd*), but the uncertainty associated with these inferences is expected to be smaller than that associated with subsurface soil conditions. P_{liq} can be interpreted as the percent of the area covered by liquefaction ($\%A_{liq}$), as in the USGS ground failure product (Allstadt et al. (2021)).

Applying site-specific procedures regionally by inferring subsurface conditions also gives P_{liq} , and can account for both variability around those procedures' outputs as well as uncertainty associated with the inference of soil properties. Regardless of which of these two approaches (applying site-specific procedures with inferred inputs or applying a geospatial proxy with remotely available inputs) is used, both methods assign liquefaction and non-liquefaction randomly in a unit area, given the percent of the area covered by liquefaction ($\%A_{liq}$).

To overcome this weakness in the state of practice, we developed an empirical procedure for creating maps of areas of liquefaction and non-liquefaction based on a latent Gaussian process. This procedure extends existing geospatial proxies to allow the assignment of liquefaction and non-liquefaction across regions while reflecting the spatial correlation structure observed in liquefaction manifestations in past earthquakes.

4.3.1 Geospatial proxy for liquefaction

Geospatial proxies such as Zhu et al (2015, 2017) are commonly used to analyze liquefaction risk on a regional scale. Zhu et al (2017) proposed separate models for use in coastal and non-coastal regions, where the coastal model is applied at sites less than 20 km from the coast. Both the coastal and non-coastal models apply as independent variables the time-averaged shear-wave velocity in the top 30 m at a given location (V_{s30}), the total annual precipitation at that location (precip), and the peak ground velocity at that location in a given earthquake (PGV). The coastal model also requires the distance from the location of interest to the nearest river (d_r) and the distance from that location to the coast (d_c). The non-coastal model instead uses *wtd* at the location of interest and the distance from that location to the nearest body of water (d_w).

The Zhu et al (2017) models give the probability of liquefaction (P_{liq}) at the location of interest in a given earthquake as their output. These models interpret P_{liq} as being equivalent to $\%A_{liq}$ based on the assumptions and procedure used in their development. However, there is no established way to assign the $\%A_{liq}$ in the literature: alternatives include assigning it randomly or assigning it as a continuous, single subarea (see Figure 4.12). Neither of these, however, incorporates a spatial correlation structure, which in turn has implications for the risk assessment of a distributed infrastructure in liquefaction-susceptible geologies. In this project, we developed a procedure to assign liquefaction to %Aliq of a grid cell using spatially correlated binary variables.

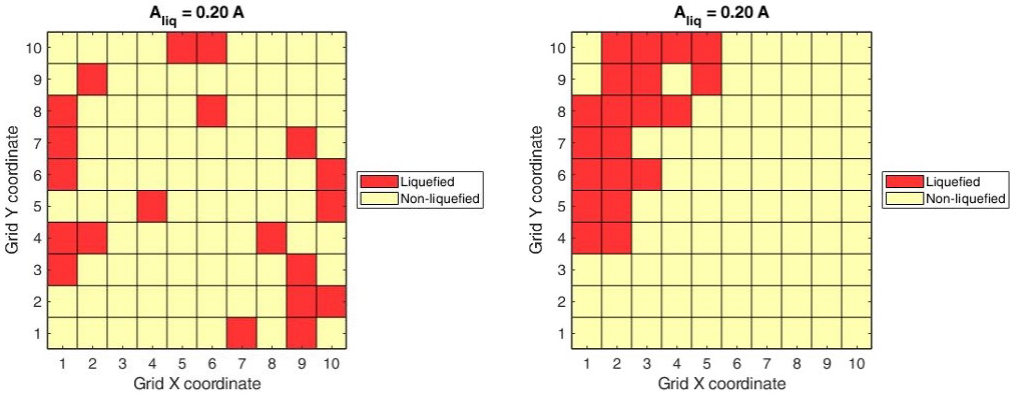

Figure 4.12. Alternatives to assign %Aliq in unit grid cell: (a) Randomly assign liquefaction to %Aliq of grid cell; and (b) Assign liquefaction to %Aliq of grid cell in n continuous segments

4.3.2 Liquefaction manifestation as a latent Gaussian process

Gaussian processes are collections of random variables where each variable corresponds to a location and/or a point in time. Essentially, a Gaussian process is a random field where each variable has a normal distribution. The distribution of a Gaussian process is then the joint distribution of all those (essentially infinite) random variables, and as such, it is a distribution over functions with a continuous domain.

Our methodology interprets the spatial distribution of surficial liquefaction manifestation as being governed by a latent (i.e., hidden) Gaussian process. In the context of latent variable modeling (see, e.g. Skrondal and Rabe-Hesketh (2007)), this Gaussian process is a *hypothetical construct*, meaning that it cannot be directly observed. Rather, we must measure it indirectly based on observations of liquefaction manifestation and our assumptions about its behavior. Describing a Gaussian process requires first obtaining a covariance function that describes the correlation among locations distributed in space. Formulating empirical semivariograms and fitting theoretical functions to the results is one approach to obtaining the covariance function. We here model the theoretical semivariogram using a nested exponential model after Markhvida et al. (2018), given by:

$$\hat{\gamma}(h) = 1 - c_1 \exp\left[-3\left(\frac{h}{\ell_1}\right)\right] - c_2 \exp\left[-3\left(\frac{h}{\ell_2}\right)\right] \qquad (4.1)$$

This functional form for the semivariogram allows us to model separate short- distance and long-distance correlation structures, where the respective correlation lengths are ℓ_1 and ℓ_2. This feature allows the model to capture the influence of the size of individual manifestations (i.e., the scale of sand boils or clusters of sand boils) with ℓ_1 and the influence of the size of liquefiable deposits with consistent properties with ℓ_2. The relative importance of the short- and long-distance correlation is determined by c1 (the weight on the short-distance correlation). c_2 is equal to $1 - c_1$ such that the semivariance at large distances is equal to 1.00.

Assume that we are observing a set of sites, **s**, where s_i is the i^{th} site; we denote surficial manifestations at the sites as **m**, where m_i=1 if there is liquefaction at s_i, and zero otherwise; and we denote the latent Gaussian process as Z and a given realization of Z as z(**s**), whose cumulative probability of being below a threshold is equivalent to a positive observation of liquefaction. Our goal is to define Z such that Equation (4.2) is true at all s_i:

$$P(Z \leq z(s_i)) = \%A_{liq,i} \tag{4.2}$$

Liquefaction manifests at the surface at si (i.e., m_i=1) if the inequality given by Equation 4.3 holds, where $\Phi(\cdot)$ is the standard normal cumulative distribution function (CDF) and $\%A_{liq,i}$ is the portion of the area liquefied estimated at s_i :

$$\Phi(z(s_i)) \leq \%A_{liq,i} \tag{4.3}$$

If the inequality in Equation 4.3 holds, Equation 4.2 is also true. This formulation assumes that the latent Gaussian process is stationary (i.e., we assume that Z is a standard normal variable at each location in **s**). Moreover, it assumes that P_{liq} at a given site in future earthquakes is equivalent to P_{liq} at many such sites in past earthquakes. This assumption is akin to the ”ergodic assumption” commonly made in ground motion prediction (e.g. Anderson and Brune (1999)).

4.3.3 Empirical Data

To estimate the correlation structure of the latent Gassian process, we used observations of surficial liquefaction manifestations in past earthquakes. Table 1 summarizes the data used. The data were collected from Schmitt et al. (2017), Zimmaro et al. (2020), and Geyin et al. (2020). The data from each earthquake detailed in Table 1 consist of the latitude and longitude coordinates of s, as well as m_i for all s_i. The Fan et al. (2013) water table model and the Daly et al. (1997) precipitation model are used to estimate *wtd* and precip in all regions, respectively. Fan et al. (2013) is used even when post-earthquake CPT data includes water table estimates, so that *wtd* is consistent between the liquefaction (i.e., observed) and nonliquefaction (i.e., sampled) points in a given earthquake. Maps of PGV for all events are obtained from the ShakeMap Atlas (Allen et al., 2008). The Thompson et al. (2014), Ahdi et al. (2017), Foster et al. (2019), and Kwok et al. (2018) models for VS,30 are used for all locations in California, Washington, New Zealand, and Taiwan respectively. The Wald and Allen (2007) model for VS,30 is used in all other regions.

Table 4.3. Summary of the empirical data used in this study

Earthquake	Moment magnitude, M_W	Liquefaction Points
1949 Olympia, WA[a]	7.1	151
1965 Puget Sound, WA[a]	6.7	223
1989 Loma Prieta, CA[b]	6.9	108
1994 Northridge, CA[c]	6.7	34
1999 Chi-Chi, Taiwan[d]	7.7	170
2001 Nisqually, WA[e]	6.8	68
2003 San Simeon, CA[f]	6.6	10
2008 Wenchuan, China[g]	7.9	116
2010 El-Mayor Cucapah, CA[h]	7.2	72
2010 Darfield, New Zealand[i]	7.1	1315
2011 Christchurch, New Zealand[i]	6.2	4786
2015 Gorkha, Nepal[j]	7.8	12
2016 Valentine's Day, New Zealand[i]	5.7	154
2019 Ridgecrest, CA[k]	7.1	190

[a]Chleborad and Schuster (1998); [b]Tinsley III et al. (1998); [c]Stewart et al. (1996); [d]Chu et al. (2004); [e]Bray et al. (2001); [f]Holzer et al. (2005); [g]Cao et al. (2010); [h]McCrink et al. (2011); [i]Geyin et al. (2020); [j]Moss et al. (2015); [k]Zimmaro et al. (2020)

As shown in Table 4.3, there are limited instances of data from multiple earthquakes in the same region, with the exceptions of the Canterbury, New Zealand, and Puget Sound, Washington regions, each of which has three earthquakes in the database. Although there are five California earthquakes in the database, none affected the same region.

For the purposes of this study, the completeness and balance of the datasets are important. We call a dataset complete if it includes all locations with liquefaction manifestations in the corresponding earthquake. We call a dataset balanced relative to $\%A_{liq}$ if the ratio of the number of liquefaction and non-liquefaction points aligns with $\%A_{liq}$ (e.g., if 4 out of 10 s_i in a dataset have m_i =1 where $\%A_{liq,i}$ = 0.4 for all i). We calculated $\%A_{liq,i}$ using Zhu et al. (2017) for all sites in all earthquakes. Based on the calculated $\%A_{liq,i}$, the databases in Table 1 are initially imbalanced relative to estimates of $\%A_{liq}$ for the corresponding earthquake. To remediate this, we sample non-liquefaction points within the study area following an approach similar to that of Zhu et al. (2017). These points are located at least 20 m and at most 1,000 m away from existing liquefaction points. This strategy assumes that the field observations include all surficial liquefaction manifestations that were generated in the given earthquake (i.e., that the datasets are complete). Put differently, this approach assumes that, for the studies listed in Table 1, liquefaction manifested at the ground surface only at the reported liquefaction points, and that any randomly sampled point outside this set of points is a true non-liquefaction point. We are generally confident in this assumption based on experience with post-earthquake reconnaissance.

4.3.4 Empirical Approach to Characterizing the Latent Gaussian Process

Let us now suppose that the latent Gaussian process for Z described above, exists. If Z were directly observable (i.e., if we could measure its value from past event data), the development of the geospatial model would have been straightforward. However, in this case, the available empirical dataset is binary (manifestation or no manifestation) and Z, which controls the manifestation of liquefaction, is hidden. For this reason, to develop the geospatial model for Z, we first perform a Monte Carlo simulation, generating multiple realizations that satisfy the underpinning assumptions (Equation 4.3) and that are consistent with the empirical dataset.

Using the Monte Carol realizations, we then determined the spatial correlation structure of z(**s**). We formulated the empirical semivariogram of each z(**s**) and fit its theoretical semivariogram using nonlinear regression with Equation 4.2 as the functional form. Because z(**s**) has a standard normal distribution, the sill value of the empirical semivariograms is 1, and we assume that c1 + c2 = 1. Finally, because each z(**s**) is created using realizations of uniform random variables, we repeat this process 1,000 times for each earthquake using Monte Carlo simulation and analyze the pooled results. Each Monte Carlo simulation is consistent with the assumed behavior of the latent Gaussian process as well as with the $\%A_{liq,i}$ calculated using Zhu et al. (2017) at each site. Applying models in this framework derived from the empirical data in Table 1 to analyses of future earthquakes requires assuming some degree of ergodicity (i.e., that the z(**s**) obtained for past earthquakes reflect future earthquakes in those regions or elsewhere).

4.3.5 Results

Figure 4.13 shows the empirical and fitted nested exponential semivariograms for each earthquake in Table 4.3 grouped according to their regions. The results presented in Figure 4.13 and Table 4.4 indicate that for most earthquakes, the overall correlation length of liquefaction manifestation (i.e., the h where $\gamma(h)$ is approximately 0.95 and $\rho(h)$ is below 0.05) is between 300 and 500 m. These results are consistent with estimates of the correlation length of indices such as the liquefaction potential index (LPI; Iwasaki et al. (1978); $\ell \sim$500 m) and cone penetration test (CPT) cone resistance and sleeve friction ($\ell \sim$300 m) per Wang et al. (2017). Figure 4.14 shows the fitted and empirical semivariograms for each earthquake together, along with those of the results pooled together according to region.

The fitted and empirical semivariograms are similar for most earthquakes in the study. Two outliers (the 2001 Nisqually and 2015 Gorkha earthquakes) have longer correlation lengths of 800 to 900 m. The databases of observations of liquefaction manifestations for these two earthquakes are small relative to many of the other earthquakes in the database, per Table 4.3.

Table 4.4. Parameters for the fitted semivariograms for each earthquake and region

Earthquake	Exponential		
	c_1	ℓ_1 (m)	ℓ_2 (m)
1949 Olympia	1.00	473	–
1965 Puget Sound	1.00	275	–
1989 Loma Prieta	1.00	365	–
1994 Northridge	1.00	355	–
1999 Chi-Chi	1.00	506	–
2001 Nisqually	1.00	892	–
2003 San Simeon	1.00	306	–
2008 Wenchuan	1.00	333	–
2010 El-Mayor Cucapah	1.00	159	–
2010 Darfield	0.64	46	431
2011 Christchurch	0.68	77	508
2015 Gorkha	1.00	799	–
2016 Valentine's Day	0.57	8	140
2019 Ridgecrest	1.00	436	–
Washington	1.00	386	–
California	1.00	468	–
Canterbury	0.82	66	435
Other regions	1.00	445	–
Global	0.87	123	501

We should note here that the models presented above are developed without consideration of surficial geology. To examine the error introduced by this assumption, we repeat the analysis above for the earthquakes in California and restrict the non-liquefaction points to be sampled in geologic units containing quaternary alluvium or artificial fill over intertidal mud according to the Wills et al. (2015) geologic map (for all other geologic units, liquefaction is considered to be absent). The correlation lengths that we estimated conditioned on susceptible geology differ by 10% or less compared to the original values. The distance restrictions placed on sampling the non-liquefaction points (i.e., that they are between 20 m and 1,000 m away from the observed liquefaction points) may affect this result, and further investigation is needed to determine how the correlation structure of z(s) is affected by conditioning on geology, including separating the liquefaction manifestation length-scales for Quaternary alluvium and artificial fill, which in principle could be derived from densely-sampled observational data. In its current form, the model should be considered agnostic to the underlying geologic units.

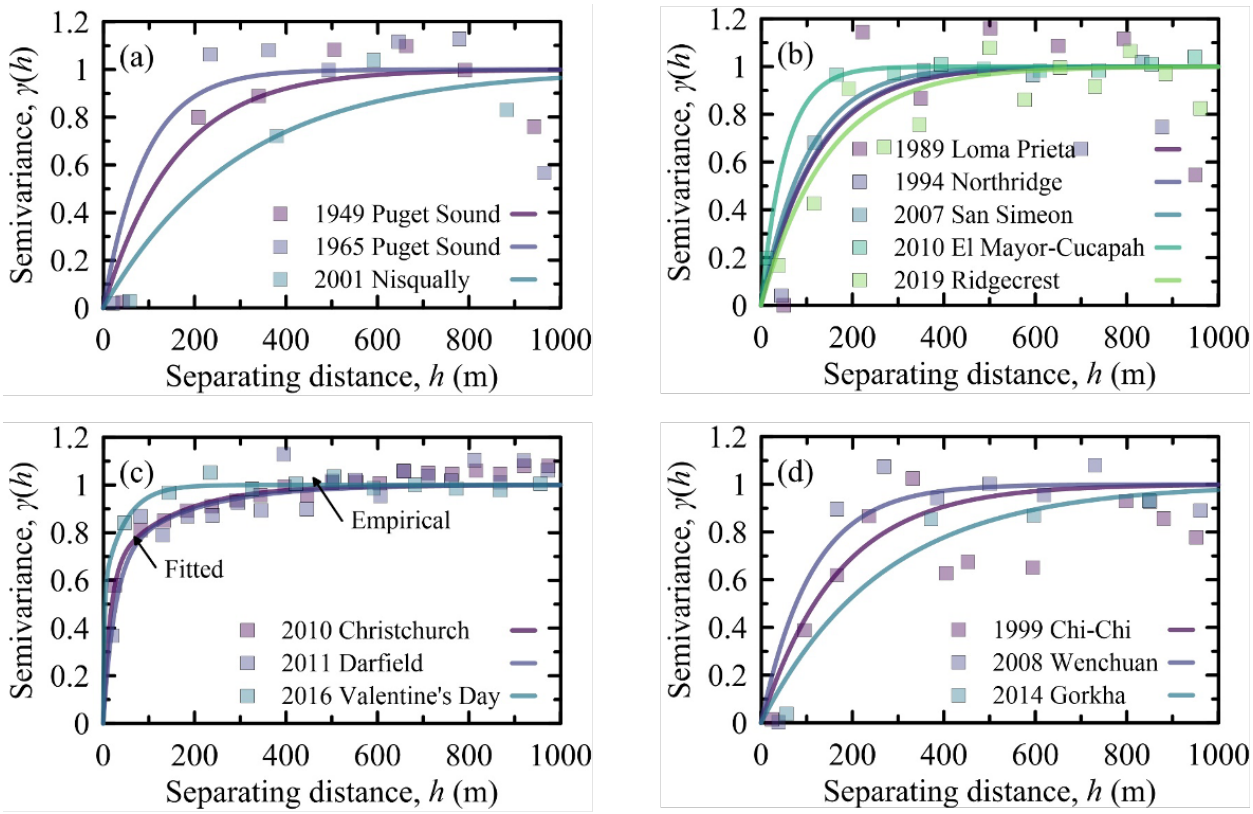

Figure 4.13. Empirical and fitted semivariograms for earthquakes in (a) Washington, (b) California, (c) Canterbury, and (d) other global locations.

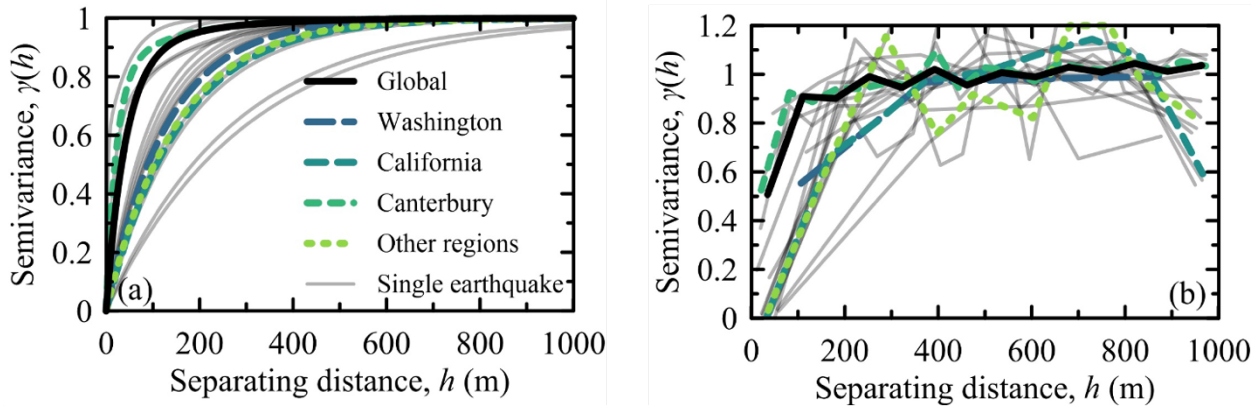

Figure 4.14. (a) Fitted and (b) empirical semivariograms calculated for each earthquake, and for the earthquakes in each region pooled together.

4.3.6 Model Implementation and Demonstration

We here provide a concise summary of how the models presented in this paper can be applied, and we validate the outcomes of the method by comparing results of the simulation to observations from the 1989 Loma Prieta and 2001 Nisqually earthquakes.

Implementing the latent Gaussian process model to produce spatially correlated maps of the liquefied area in a past or future earthquake proceeds as follows:

1. Select the lateral extents of the region of interest.
2. Divide the region of interest into a grid with spacing at least one tenth of the liquefaction feature correlation length (~468m for the ensemble of California earthquakes analyzed).
3. Define **s** by locating the centroid of each differential element within the grid (for example square, rectangular, hexagon).
4. Estimate $\%A_{liq,i}$ for each s_i using a geospatial proxy (e.g. Zhu et al. (2017)) or inference based on geology (e.g., Youd and Perkins (1978)).
5. Assemble a matrix, h, where h_{ij} is the distance separating locations s_i and s_j in m.
6. Construct the covariance matrix for a standard normal random field, $\hat{z}(s)$ using Equation 4.1 and the appropriate coefficients from Table 4.4 for the region of interest.
7. Generate the desired number of realizations of $\hat{z}(s)$.
8. For each realization, assign liquefaction to those grid polygons where $\Phi(\hat{z}(s_i)) \leq \%A_{liq,i}$ (Equation 4.3).

Case Studies

This section applies the latent Gaussian process model to develop maps of the liquefied area in Seattle, WA, in the 2001 Nisqually earthquake and San Francisco and Monterey Bay, CA, in the 1989 Loma Prieta earthquake. For all cases, we use a hexagonal grid at 100 m spacing (roughly 1/4 of $\ell 1$ for these regions). Figure 4.15 shows maps of PGV for these case studies as obtained from ShakeMaps and Figure 4.16 shows maps of $\%A_{liq}$ for these case studies as derived from the Zhu et al. (2017) model. Figures 4.17 and 4.18 show maps of $\hat{z}(s)$ for these case studies including and excluding spatial correlation, respectively. Per Equation 4.3, low (negative) and high (positive) values of $\hat{z}(s)$ are relatively likely and unlikely, respectively, to be liquefaction locations, depending on the values of $\%A_{liq,i}$. The coefficients from Table 4.4 for Washington are used for Seattle and those for California are used for San Francisco and Monterey Bay.

It should be noted that the realizations of $\hat{z}(s)$ with and without spatial correlation (Figures 4.17 and 4.18 correspondingly) are operators that translate the percent area liquefied ($\%A_{liq,i}$) maps into spatially correlated maps and uncorrelated maps (Figures 4.19 and 4.20 correspondingly) of the liquefied area, and as such have no physical meaning.

Next, Figures 4.19 and 4.20 show maps of the liquefied area corresponding to the $\hat{z}(s)$ fields from Figures 4.17 and 4.18. Qualitatively, we see that the density of liquefaction observations in both the correlated and uncorrelated maps (Figures 4.19 and 4.20) reflects the spatial distribution of the $\%A_{liq}$ predictions. Furthermore, the predictions of $\%A_{liq}$ reflect the different geologic conditions (e.g. Treasure Island is a hydraulic fill, and Yerba Buena island is a rock outcrop). In the uncorrelated maps the liquefaction points do not tend to form continuous polygons corresponding to liquefaction features such as lateral spreads. However, such features are obtained by application

of the spatial correlation model, which produces the correlated map (Figure 4.19) that has clearer distinctions between areas of liquefaction and nonliquefaction.

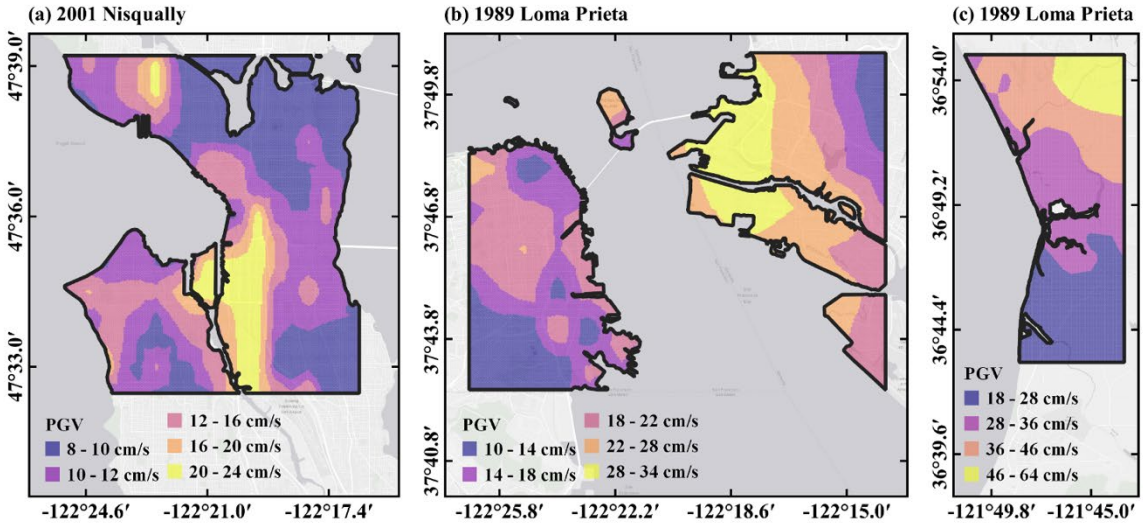

Figure 4.15. Peak ground velocity maps for (a) Seattle in the 2001 Nisqually earthquake, (b) San Francisco and Oakland in the 1989 Loma Prieta earthquake, and (c) Monterey Bay in the 1989 Loma Prieta earthquake.

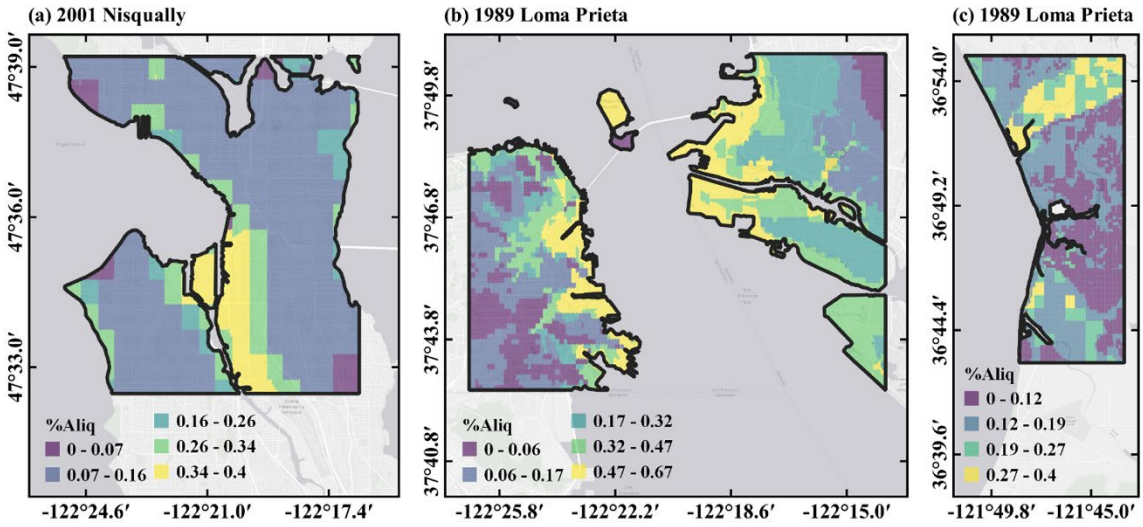

Figure 4.16. Percent area liquefied ($\%A_{liq,i}$) maps for (a) Seattle in the 2001 Nisqually earthquake, (b) San Francisco and Oakland in the 1989 Loma Prieta earthquake, and (c) Monterey Bay in the 1989 Loma Prieta earthquake. $\%A_{liq,i}$ calculated using Zhu et al. (2017).

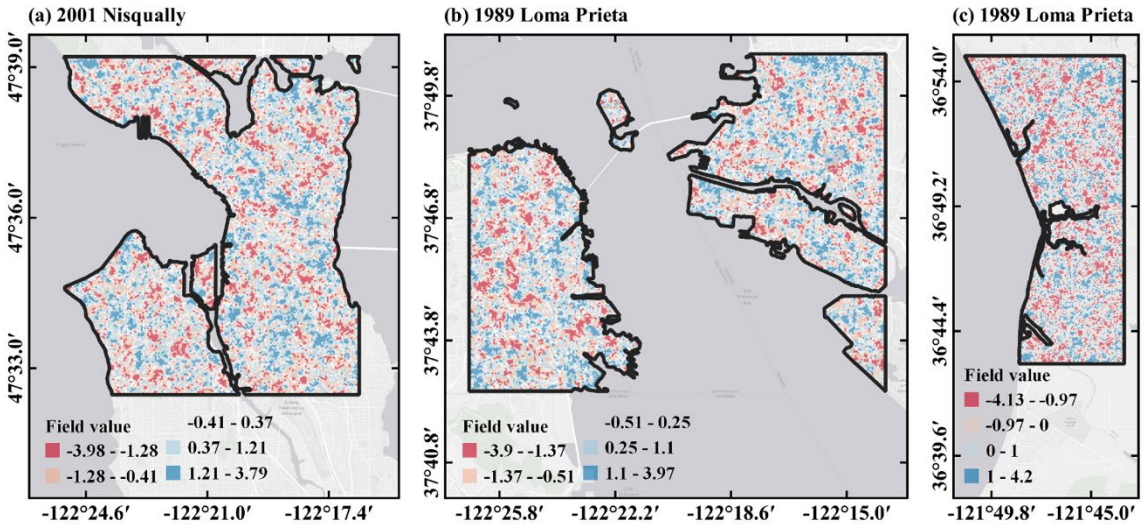

Figure 4.17. Spatially correlated standard normal random field maps, depicting field value ($\hat{z}(s)$) for (a) Seattle in the 2001 Nisqually earthquake, (b) San Francisco and Oakland in the 1989 Loma Prieta earthquake, and (c) Monterey Bay in the 1989 Loma Prieta earthquake.

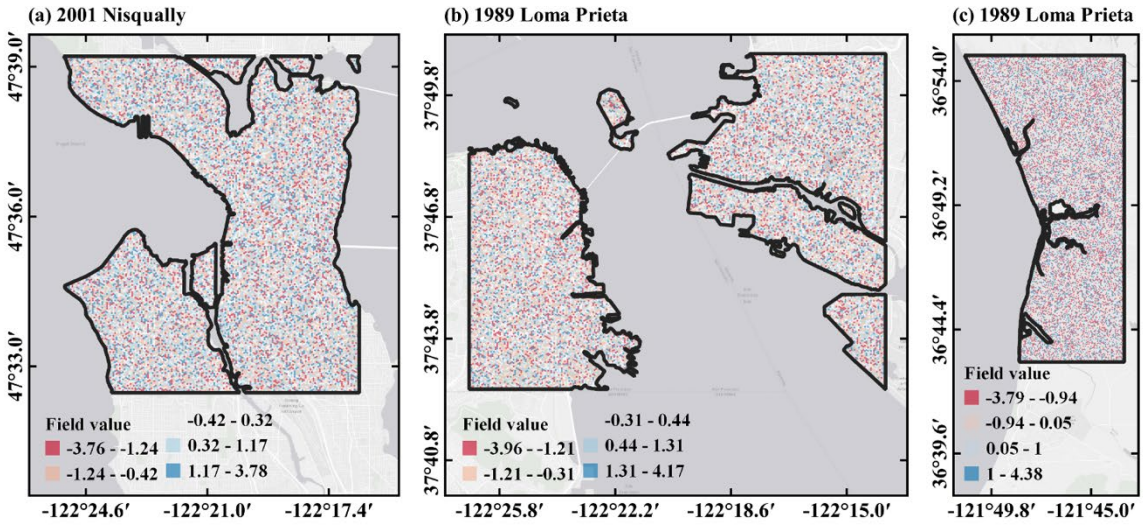

Figure 4.18. Uncorrelated standard normal random field maps, depicting field value ($\hat{z}(s)$) for (a) Seattle in the 2001 Nisqually earthquake, (b) San Francisco and Oakland in the 1989 Loma Prieta earthquake, and (c) Monterey Bay in the 1989 Loma Prieta earthquake.

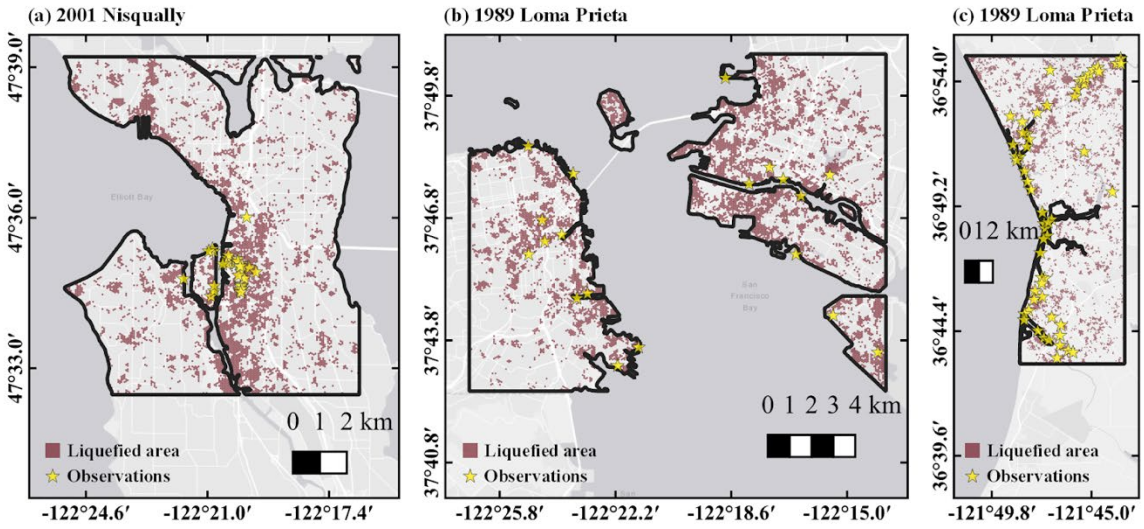

Figure 4.19 Spatially correlated maps of the liquefied area for (a) Seattle in the 2001 Nisqually earthquake, (b) San Francisco and Oakland in the 1989 Loma Prieta earthquake, and © Monterey Bay in the 1989 Loma Prieta earthquake.

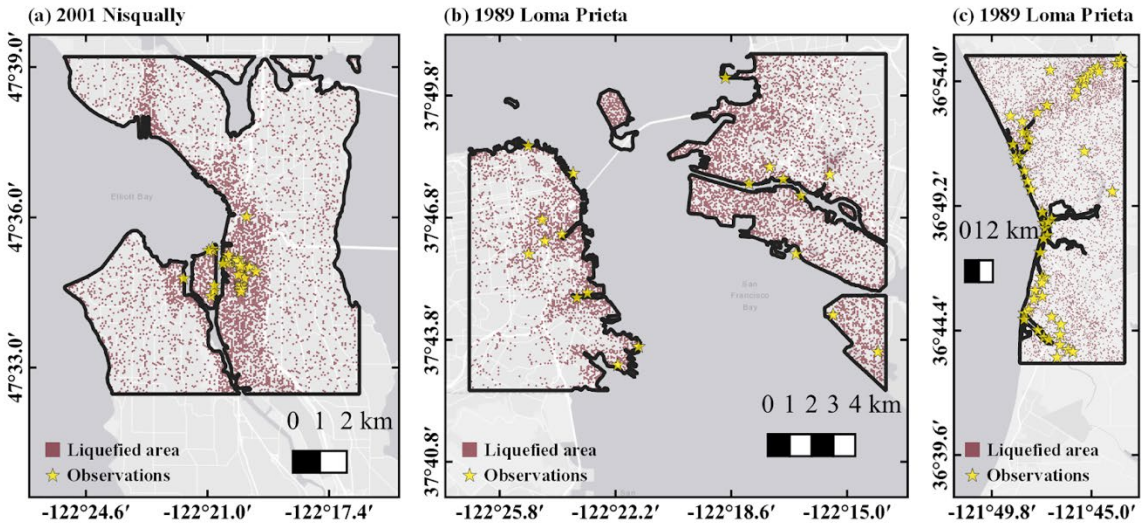

Figure 4.20. Uncorrelated maps of the liquefied area for (a) Seattle in the 2001 Nisqually earthquake, (b) San Francisco and Oakland in the 1989 Loma Prieta earthquake, and (c) Monterey Bay in the 1989 Loma Prieta earthquake.

We can obtain a suite of maps like those in Figure 4.19 for each region by generating multiple realizations of $\hat{z}(s)$ in Monte Carlo simulation. Each map can be used to evaluate performance metrics of interest (e.g. disruption of an infrastructure system), the results of which can then be aggregated across the map suite to evaluate probabilities (e.g., probability of failure of an infrastructure system). To verify that the Gaussian process accurately captures the predictions of

%Aliq from the geospatial model, Figure 4.21 shows the simulated $\%A_{liq}$ (i.e., the area of cells marked as ”liquefied areas” in Figures 4.19 and 4.20 divided by the total area) binned according to the predicted $\%A_{liq}$ (i.e., Figure 4.16). Results from 10 random field realizations are shown for both approaches. Either approach generates maps of the liquefied area that are consistent with $\%A_{liq}$. Across a sufficiently large number of realizations, the true positive rate at sites with manifestations is equal to $\%A_{liq,i}$ at those sites, as dictated by Equation 4.3. The false positive rate at sites without manifestations is likewise equal to $\%A_{liq,i}$ at those sites. These identities are true for the implementations with and without spatial correlation. However, the case including spatial correlation is more likely to correctly identify clusters of sites with manifestations. Figure 4.22 shows the true positive rate conditioned on a nearby true positive (that is, how likely it is for the model under evaluation to have correctly predicted that a site has truly liquefied given that a nearby site has also liquefied) for the cases with and without spatial correlation for 1,000 realizations of the Monterey Bay and Puget Sound study areas. These areas are used for this analysis because they include more observations (46 and 37 points, compared to 16 in the San Francisco and Oakland study area). The conditional true positive rate is much higher at short distances when including spatial correlation. In the case without correlation, predictions at each site are independent, and the true positive rate is $\%A_{liq,i}$ regardless of whether a site with a true positive is located nearby.

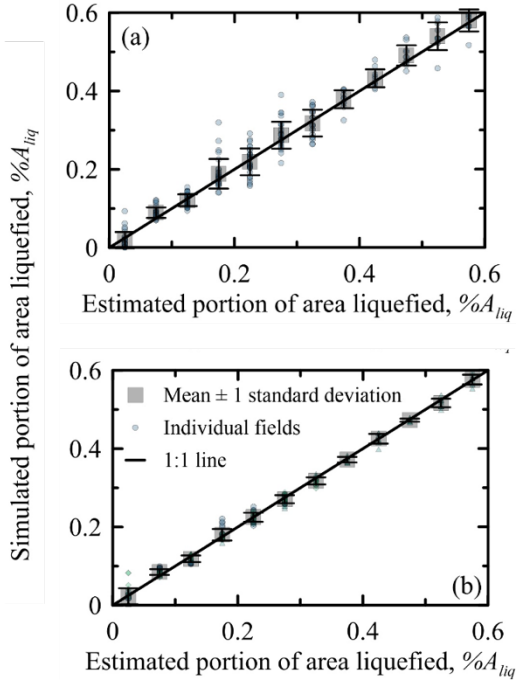

Figure 4.21. Comparison of the predicted and simulated $\%A_{liq}$ values for 10 random field realizations for each case study area for (a) the case including spatial correlation and (b) the uncorrelated case.

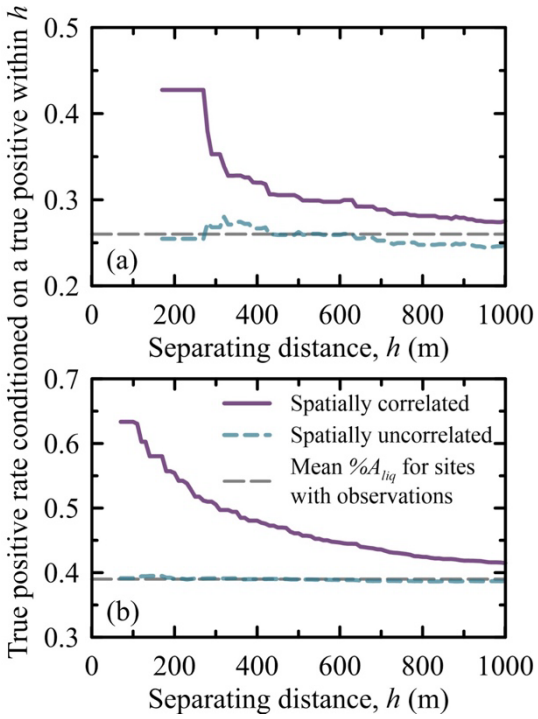

Figure 4.22. The true positive rate for sites in the (a) Monterey Bay and (b) Puget Sound case study areas conditioned on a true positive within a threshold separating distance.

We next demonstrate the use of the method for a region in Southern California, where observations of liquefaction were available from the 1994 Northridge M6.7 reconnaissance. Figures 4.23-4.29 show sequence of input parameters, from the geology and ground motion distribution to the estimated settlement and lateral spreading prior and after the application of the Gaussian process model.

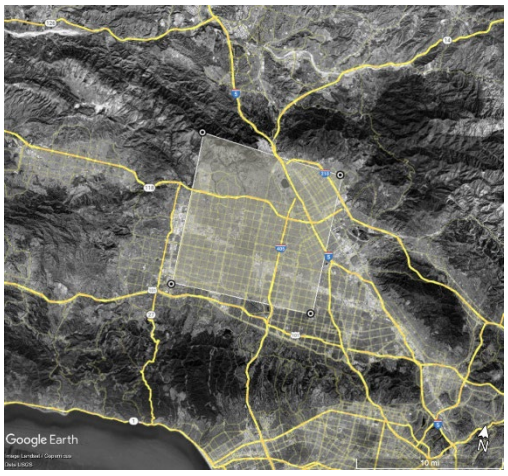

(a)

Figure 4.23. (cont)

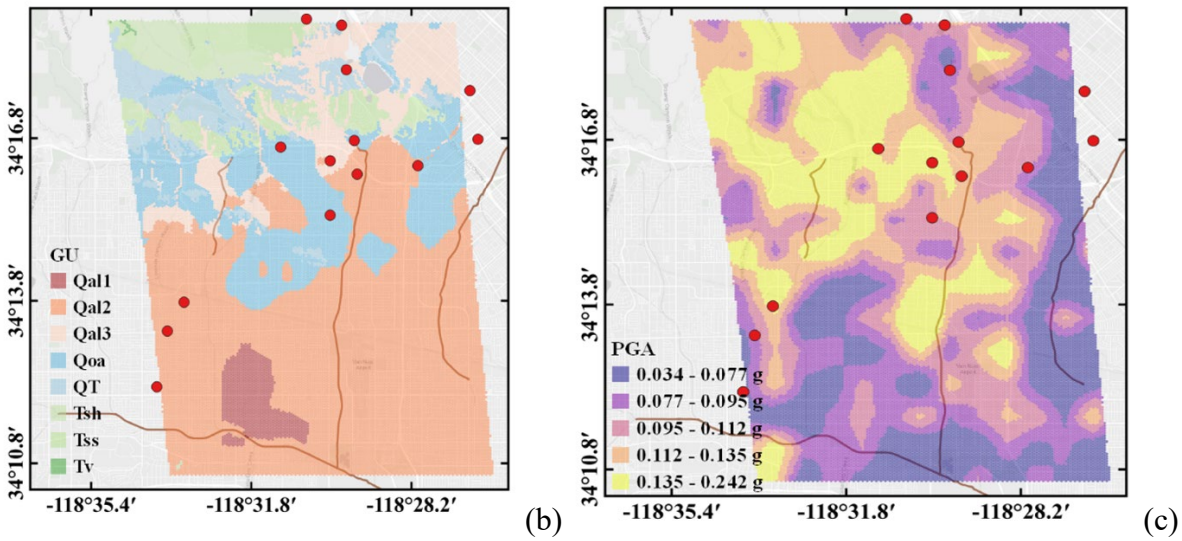

Figure 4.23. Study area affected by 1994 M6.7 Northridge earthquake: (a) location on the map along with observations of liquefaction (red dots); (b) geologic index of the study area; and (c) Shakemap PGA of the event, used for triggering and displacement evaluation

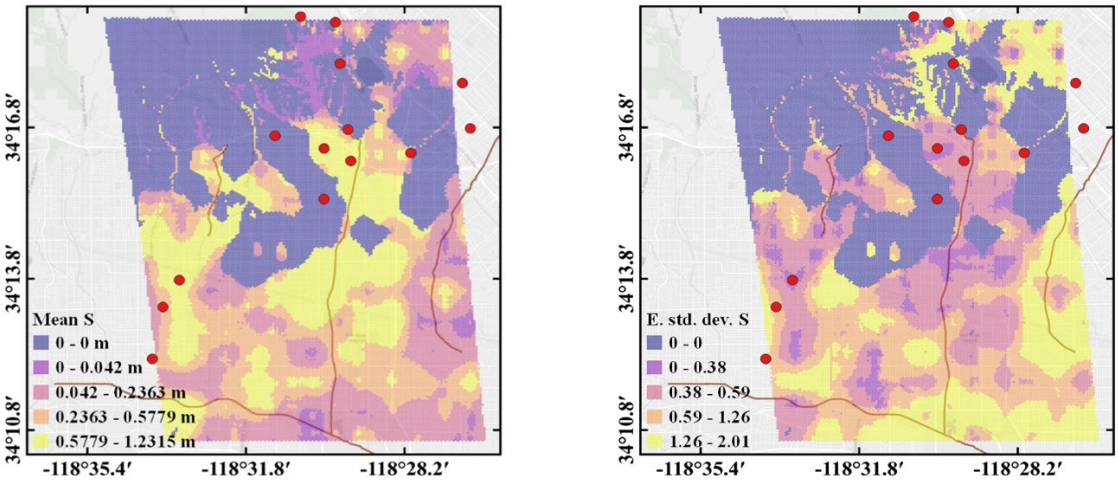

Figure 4.24. Mean and standard deviation of settlement estimation in study area

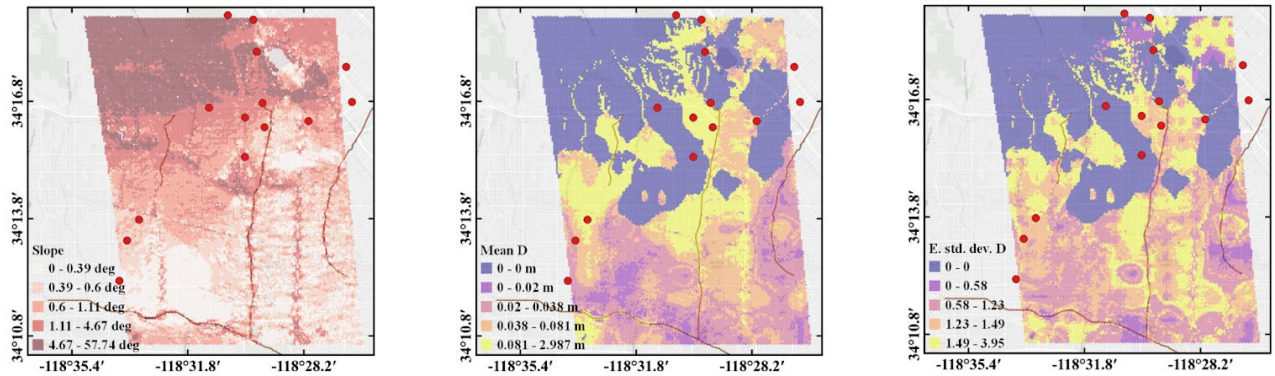

Figure 4.25. Slope, mean and standard deviation of lateral spread estimation in study area

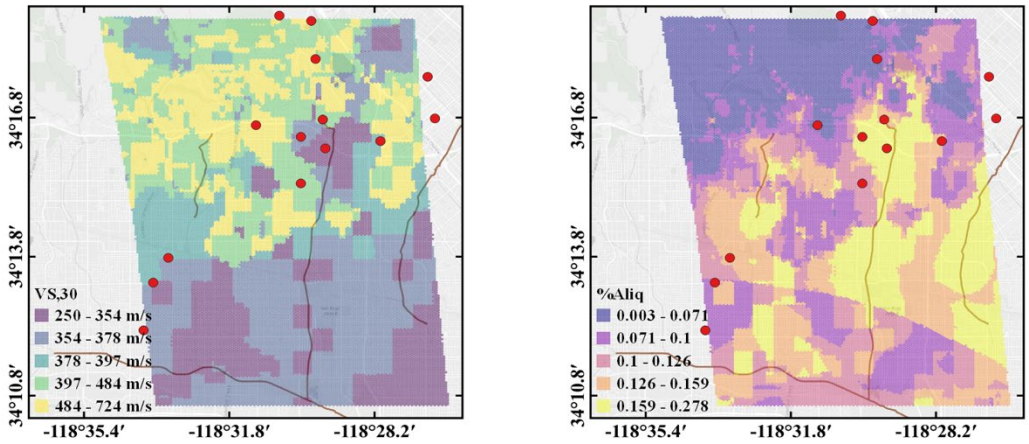

Figure 4.26. Vs30 and resulting %Aliq from the geospatial model by Zhu et al (2017)

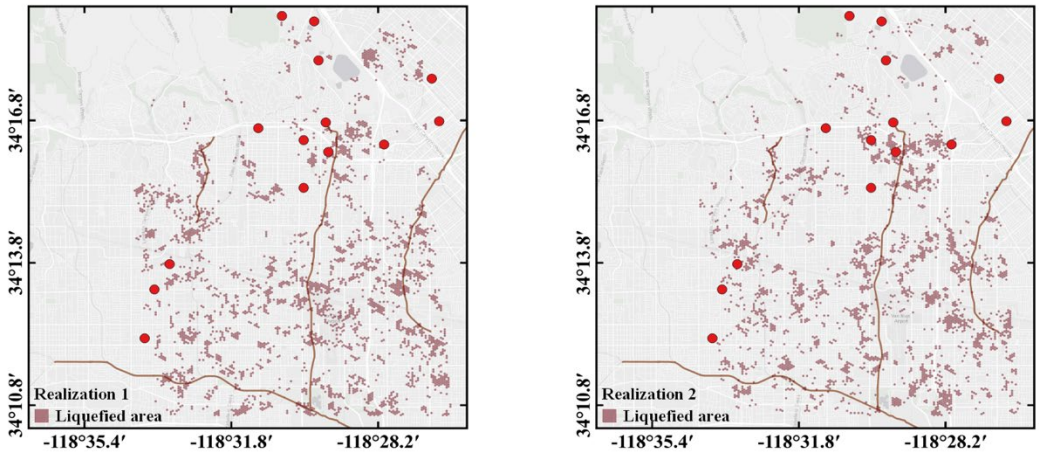

Figure 4.27. Two realizations of $\%A_{liq}$ into liquefaction manifestation through the gaussian process model: liquefaction is assigned to points where the standard normal cumulative distribution function (CDF) of z at site i falls below $\%A_{liq}$ at that site.

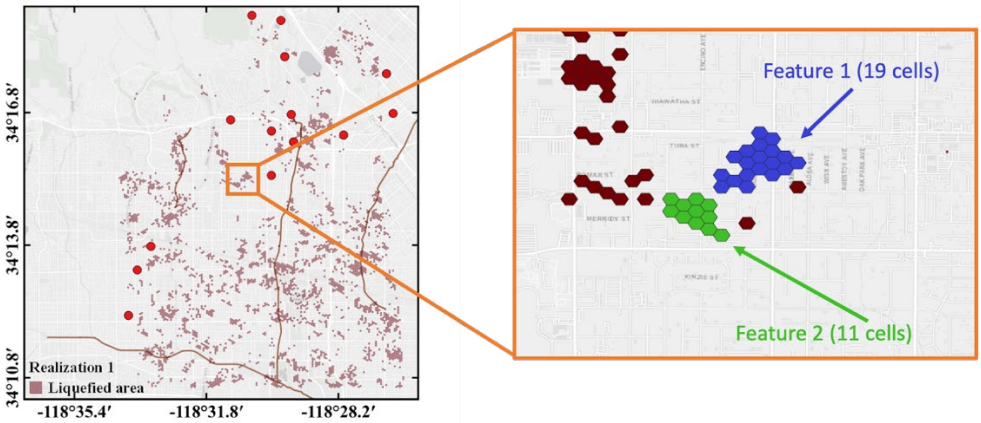

Figure 4.28. Zoom-in one realization of liquefaction manifestation, revealing among others, two features (grid cells connected to in a continuous formation)

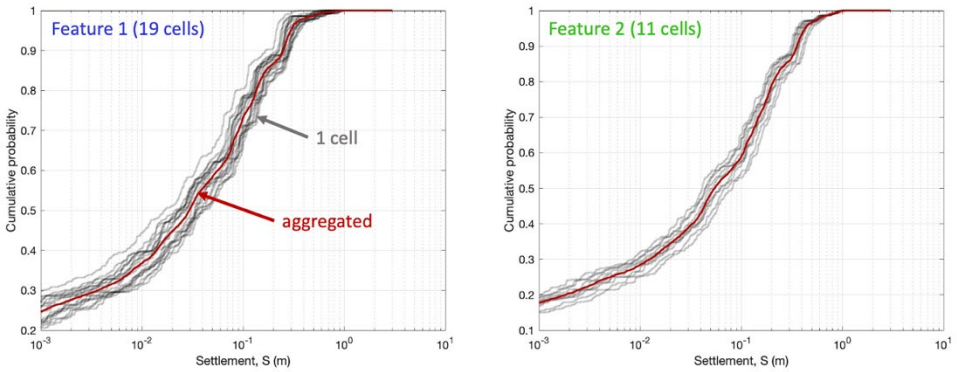

Figure 4.29 Individual and aggregate settlement probabilities for each feature in Figure 4.28.

4.3.7 Geological vs Geospatial Approaches for Feature Mapping

The Zhu et al., 2017 geospatial liquefaction model used in this work to map the spatial extent of liquefaction, uses globally available geospatial explanatory variables that are proxies for soil density, soil saturation and dynamic loading. The models were developed using logistic regression. Zhu et al. (2017) also proposed a logistic function to translate the liquefaction probability to an estimate of the liquefaction spatial extent (%Aliq), which, as we saw above, allows the resulting map to provide an estimate of the fractional area of liquefaction within a pixel/polygon, and can be more directly compared with ground observations of liquefaction.

An alternative approach to map probability of liquefaction is to use decision thresholds central to the use of liquefaction hazard frameworks, such as the liquefaction severity number (LSN). The severity of soil liquefaction manifested at the ground surface serves as a practical proxy for liquefaction damage potential, particularly for pavement systems, buried lifelines, structures on shallow foundations, and other near-surface infrastructure; by way of this simplifying proxy, hazard frameworks have been proposed to link the factor of safety against liquefaction triggering at depth (FSliq) to damage potential. Iwasaki et al. (1978) proposed the first such framework: the liquefaction potential index (LPI), which has been used to assess liquefaction hazards worldwide.

Though widely adopted, evaluations of LPI following recent liquefaction events, such as the 2010-2011 Canterbury Earthquake Sequence (CES), show that it performs inconsistently (e.g., Maurer et al., 2014). This inconsistency inspired the development of new hazard frameworks, among which the liquefaction severity number (LSN) (van Ballegooy et al., 2014a), a variation of 1-dimensional post-liquefaction reconsolidation settlement (e.g., Zhang et al., 2002). Central to all of these hazard frameworks are proposed decision thresholds corresponding to different levels of expected hazard. For example, Iwasaki (1986) proposed that liquefaction hazard is “low” at sites where LPI $\leq$ 5, “high” where 5 < LPI $\leq$ 15, and “very high” where LPI > 15. Similarly, Tonkin and Taylor (2013) proposed that little to no manifestation of liquefaction is expected at sites where LSN < 20; moderate to severe manifestation of liquefaction is expected where 20 < LSN < 40; and major manifestation of liquefaction is expected where LSN > 40. Thus, an LPI of 5 and an LSN of 20 correspond to similar levels of expected hazard.

In this section, we compare the extent of liquefaction evaluated through frameworks based on LPI and LSN to the $\%A_{liq}$ estimated using the Zhu et al (2017) model, along with realizations of areas of liquefaction manifestation using the Gaussian Process model described above. The comparative study starts with analyzing all CPTs for each geologic unit to obtain geotechnical indices, namely:

$$LPI(CPT_i) = f(CPT_i, PGA, M_W, wtd) \quad \text{or} \quad LSN(CPT_i) = f(CPT_i, PGA, M_W, wtd) \tag{4.4}$$

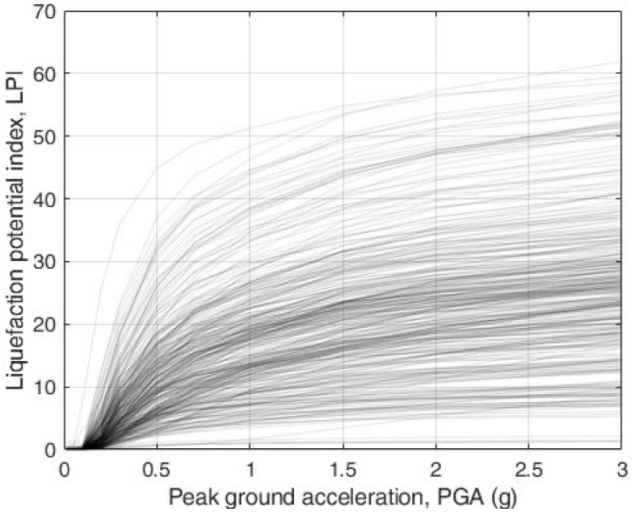

Figure 4.30. CPT realizations within the geologic unit artificial fill over bay mud analyzed in this study, translate into LPI vs. PGA distributions.

Next, for a given index threshold, we calculate the probability of exceedance for a given unit (e.g. the geologic unit in Figure 4.30) as follows:

$$P_{liq}(GU_j) = \frac{N\left(CPT_{GU_j} \ni \text{ Index } > x\right)}{N\left(CPT_{GU_j}\right)} \quad P_{liq}(GU_j) = f(x, PGA, M_W, wtd) \tag{4.5}$$

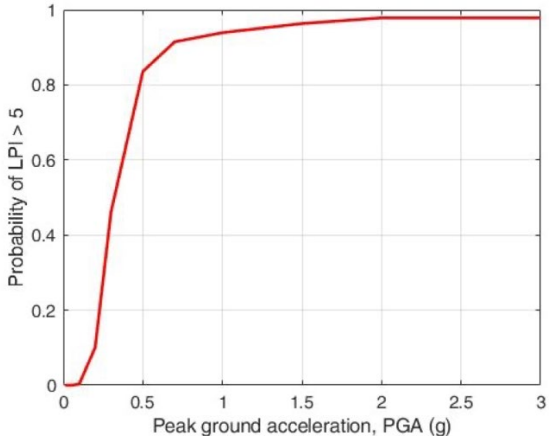

Figure 4.31. Example of probability of exceedance of liquefaction potential index LPI > 5, for the geologic unit of Figure 4.30 as a function of PGA

The input parameters required in each approach (geologic vs geospatial) for the 1989 Loma Prieta Earthquake are shown in Figure 4.32. Specifically, the geology-based probability is based on PGA, geologic unit and *wtd*; whereas the geospatial model probability is based on PGV, Vs30 and *wtd*.

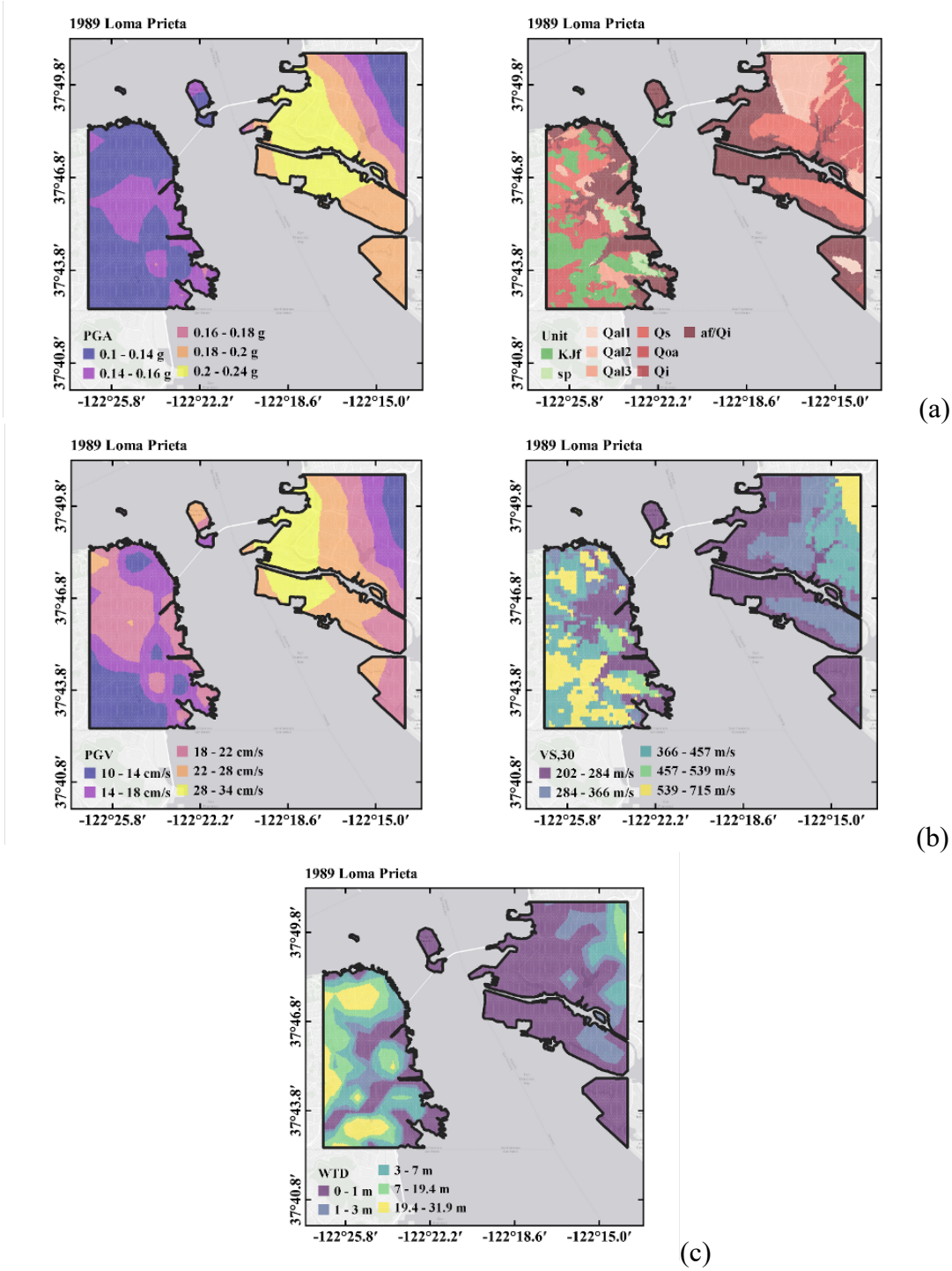

Figure 4.32. Input parameters required in (a) the geologic and (b) the geospatial approach for the 1989 Loma Prieta Earthquake scenario. The water table depth shown in (c) is an input in both approaches.

Results for the 1989 Loma Prieta scenario are compared in Figure 4.33. As can be seen, the geospatial model on the left yields more granularity in probability distribution of the Bay Area. Interestingly, although Treasure Island is estimated to have a $P_{liq} > 50\%$ with all approaches, only the geospatial model yields P_{liq} for Yerba Buena Island equal to zero (i.e. consistent with the observations). The percent difference between the geospatial and each of the geologic models in terms of $\%A_{liq}$ is depicted in Figure 4.34. Lastly, Figure 4.35 shows the implementation of the latent Gaussian model for liquefaction manifestation applied in each of the three variants of A_{liq} shown in Figure 4.33.

While the geospatial model yields more realistic distribution of liquefaction manifestation compared to the geology-based susceptibility indices, what is important here is that the spatial correlation model is agnostic to the underlying approach of estimating P_{liq} on a regional scale, and can thus be applied so long as the uncertainty associated with the Pliq estimation is of order comparable to that of the geospatial model by Zhu et al (2017) used in this work.

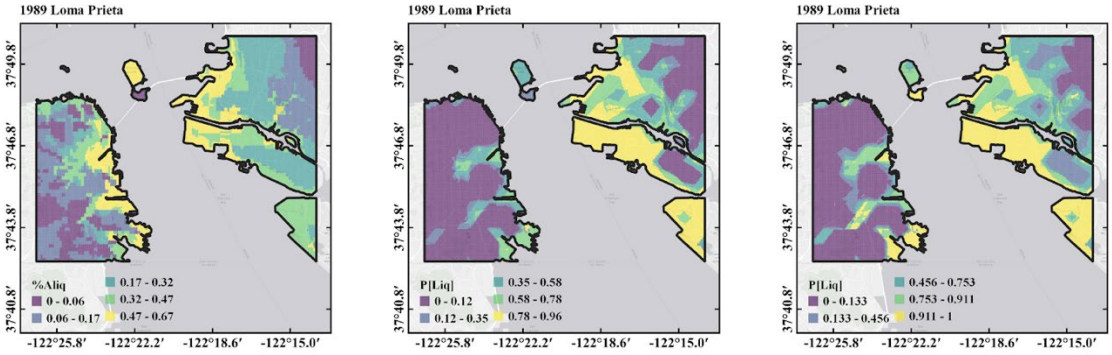

Figure 4.33. Probability of liquefaction estimated using the geospatial (left), the geologic model with threshold LPI>5 (middle), and the geologic model with threshold LSN >15 (right)

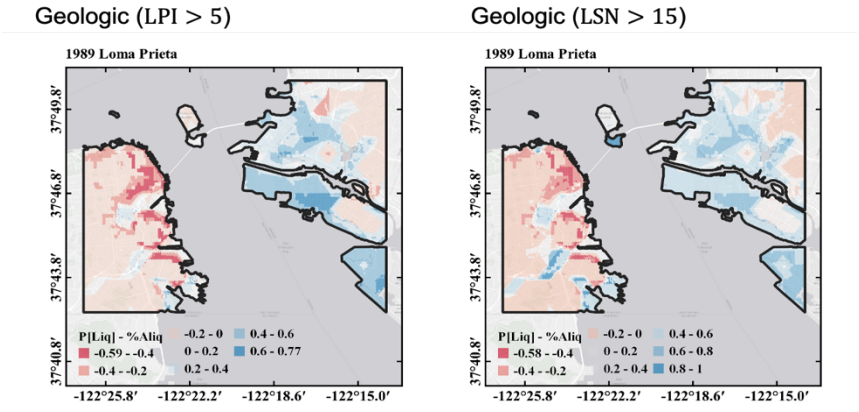

Figure 4.34 Difference in $\%A_{liq}$ between Zhu et al (2017) geospatial model and the two geologic models based on LPI and LSN thresholds.

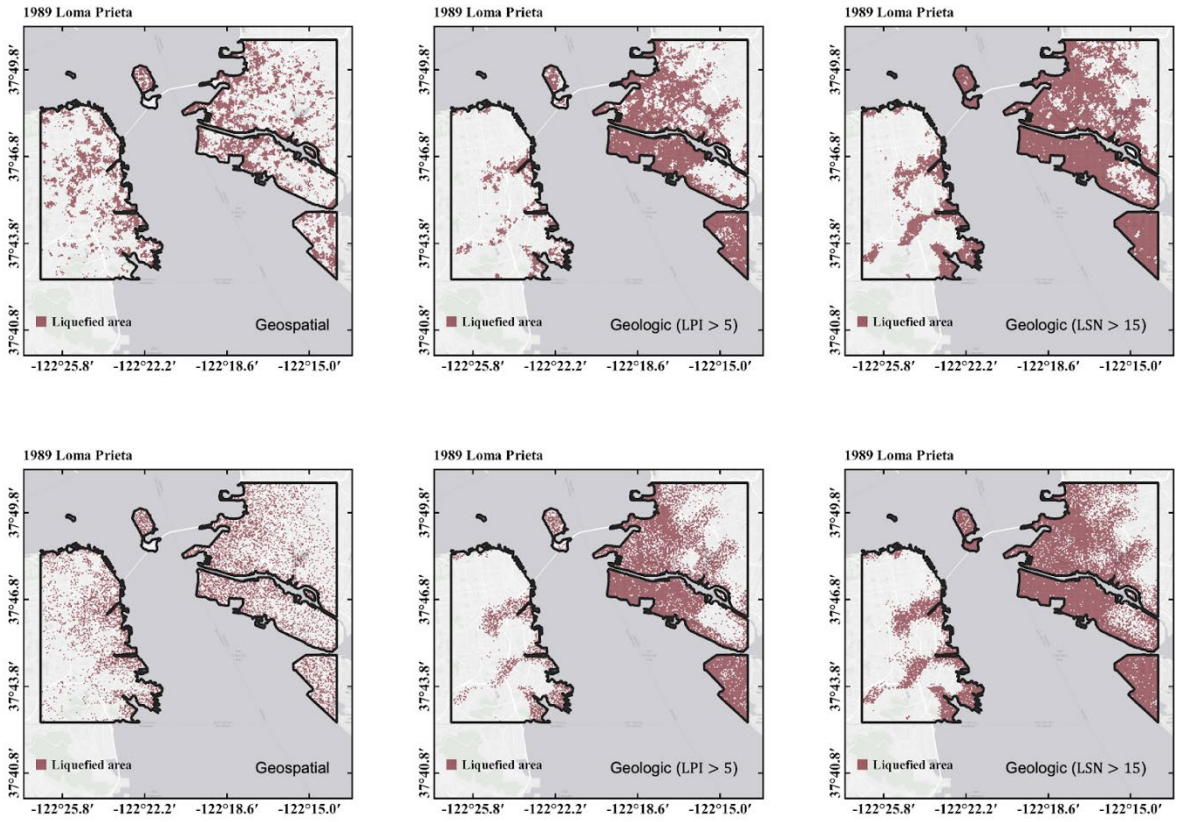

Figure 4.35. Liquefaction manifestation realizations with and without spatial correlation, using the three alternative models to map the $\%A_{liq}$ during the 1989 Loma Prieta earthquake.

4.4 Sensitivity Analysis of Logic Tree

In this section, we evaluate the sensitivity of our liquefaction hazard logic tree. We demonstrate the sensitivity analysis at a site on flat quaternary alluvium in San Jose. We then formulate all logic tree branches (levels 1-5) and define their residual relative to the total mean:

$$\mu = \exp\left(\sum_i w_i \ln(\mu_i)\right) \tag{4.6}$$

where ⌈i is the mean of the distribution for each branch, and μ is the total mean of the logic tree distribution. Then, each branch has a residual given by:

$$\varepsilon_i = \ln(\mu_i) - \ln(\mu) \tag{4.7}$$

Next, we use mixed effects regression to separate the individual branch contributions to the variance of means. We specifically break down the residuals into components for the typical profile, the CPT profile realization, the water table and water table realization (in well-maps kriging), the susceptibility model, the triggering model, the triggering model realization, and the deformation model:

$$\varepsilon_i = (\delta P + \delta P^r) + (\delta W + \delta W^r) + \delta S + (\delta T + \delta T^r) + \delta D$$
$$\sigma_\mu^2 = \left(\sigma_P^2 + \sigma_{P^r}^2\right) + \left(\sigma_W^2 + \sigma_{W^r}^2\right) + \sigma_S^2 + \left(\sigma_T^2 + \sigma_T^2\right) + \sigma_D^2 \quad (4.8)$$

We repeat the process separately for settlement and lateral spread. Results are depicted in Figures 4.36-4.42. In each case, we evaluated the contribution of the individual models to the total variance as $C = \sigma_X^2/\sigma_\mu^2$.

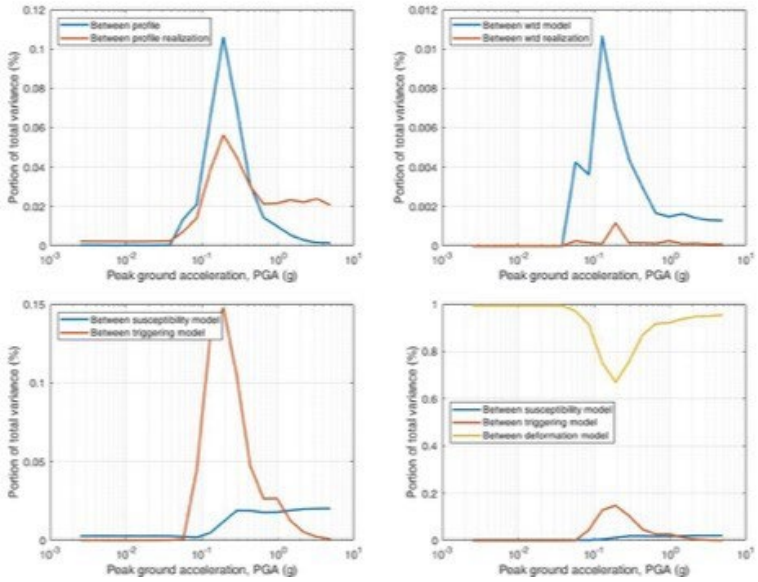

Figure 4.36 Sensitivity of variance to intensity (settlement)

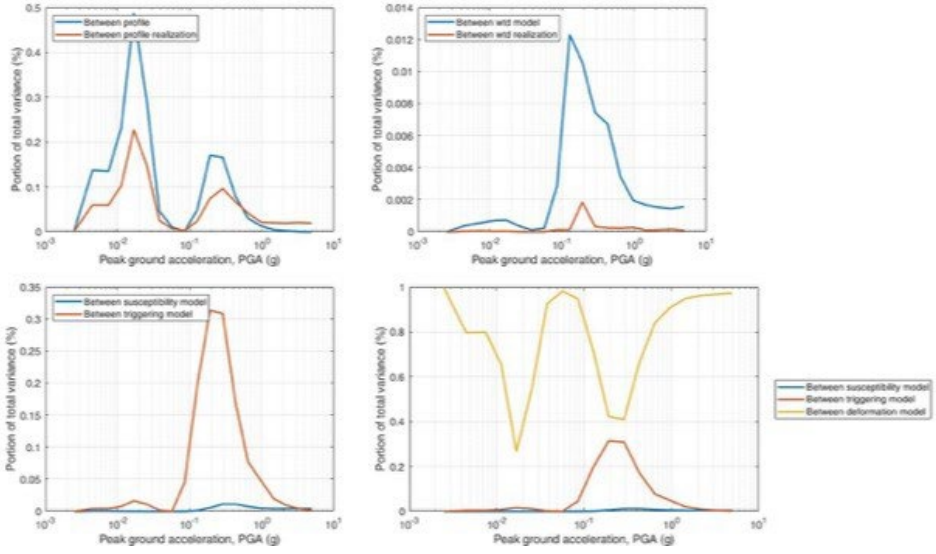

Figure 4.37 Sensitivity of variance to intensity (lateral spread)

Adding uncertainty to the *wtd* models increased the corresponding variance components, but the overall uncertainty is small relative to the contribution of triggering and deformation:

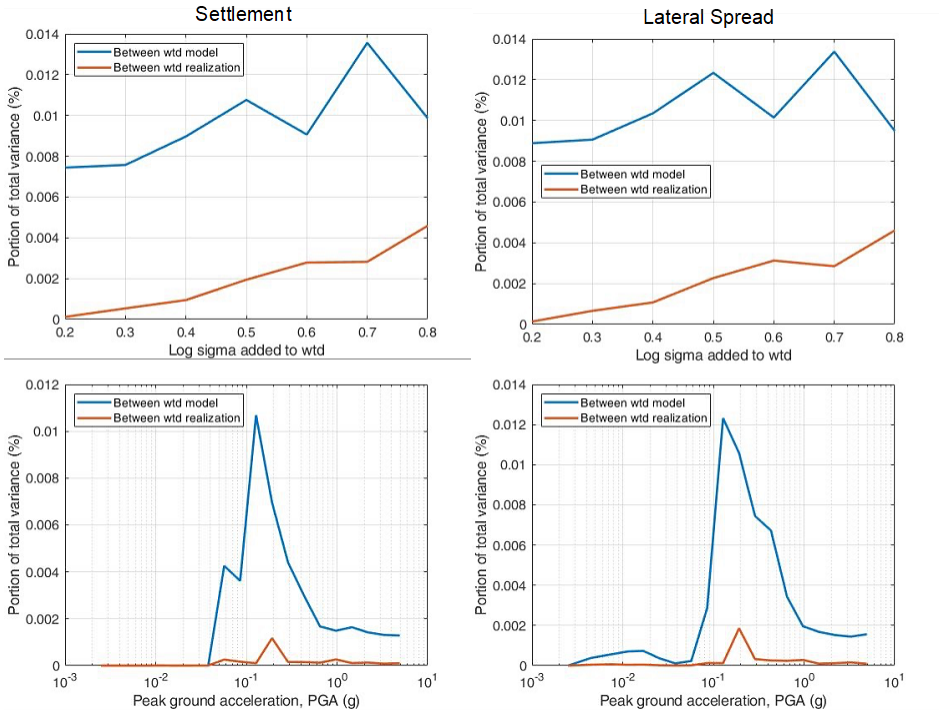

Figure 4.38 Contribution of uncertainty of the wtd models to the total variance of the logic tree for settlement (left) and lateral spread (right).

Our analyses showed that the settlement models have extreme log variance at low intensities (i.e., 10^{-6} m and 10^{-4} m have small absolute difference, large log difference). Rather than reporting log variance at low intensities, we assumed that if our analysis yields that liquefaction was triggered, then S $>10^{-3}$ m.

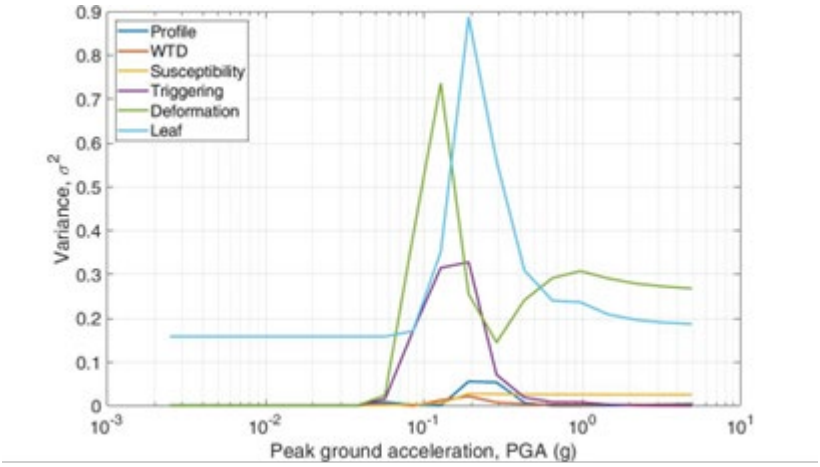

Figure 4.39 Sensitivity of variance to intensity for a given geologic unit

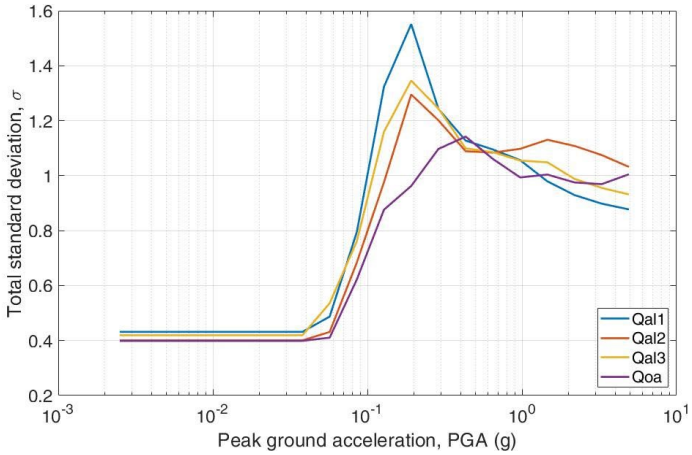

Figure 4.40 Sensitivity of total standard deviation to intensity across four geologic units

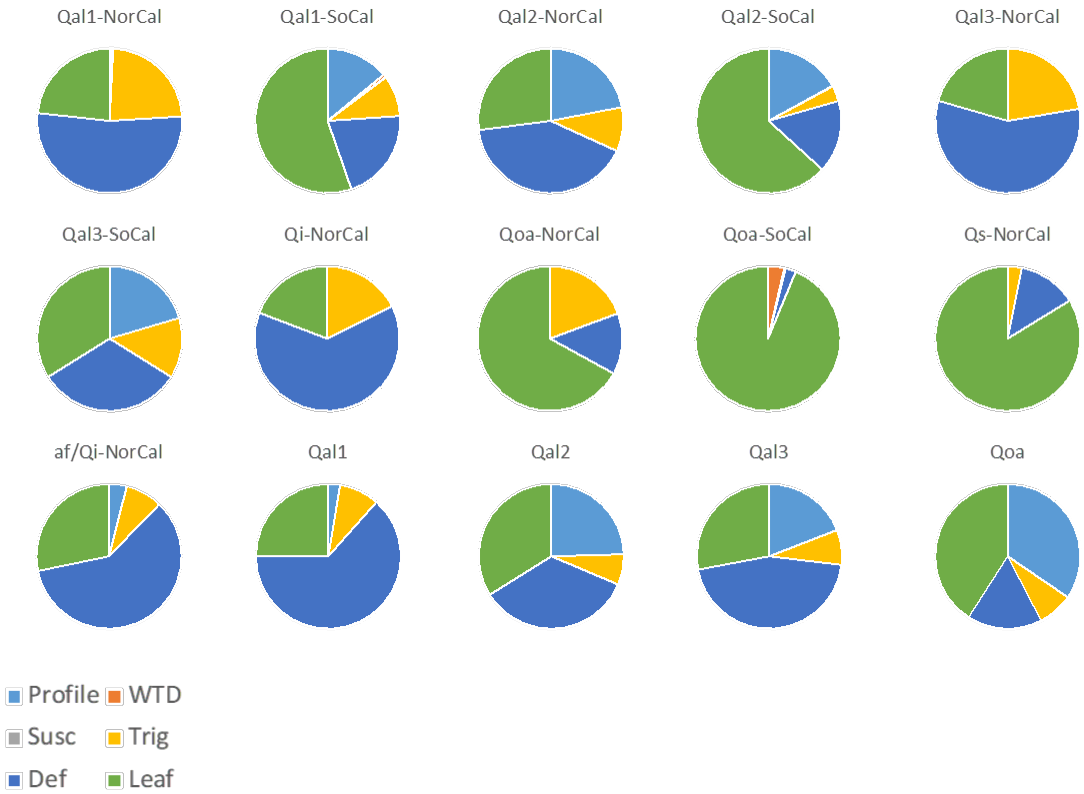

Figure 4.41 Pie charts of contribution to total standard deviation across all susceptible geologic units for low intensity motion (PGA = 0.09g)

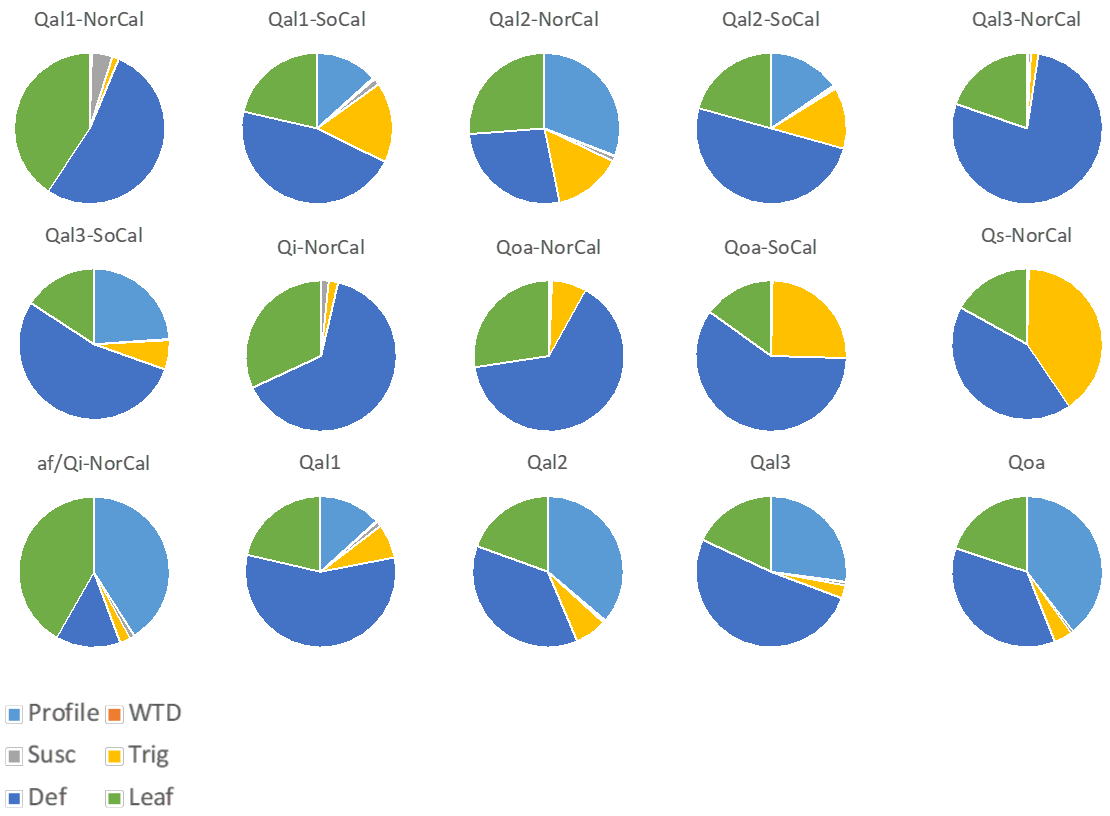

Figure 4.42 Pie charts of contribution to total standard deviation across all susceptible geologic units for high intensity motion (PGA = 0.97g)

4.5 Summary

We developed and presented a regional methodology for estimating liquefaction-induced ground failure deformations and assigning them spatially. The uncertainty around regional estimates of deformations remains high compared to site-specific estimates, but the approach described herein allows rapid application of liquefaction risk analysis procedures without extensive site-specific data. The methodology uses a logic tree to represent uncertainty in subsurface conditions as well as liquefaction susceptibility, triggering, and deformations. Two features of this approach act to reduce overestimation of liquefaction risk. First, the logic tree yields a probability mass at zero displacement, meaning that even areas affected by liquefaction may experience zero deformations. Second, a spatial model for distribution liquefaction was applied, which reduces the total area over which deformations are estimated.

5 Presentation of Results

The distributions of geo-hazards (i.e., landslides and liquefaction features) were assessed using the procedures described in Chapters 3 and 4 for the 25 earthquake scenarios described in Wang et al. (2023). This chapter has two aims: (1) provide example landslide and liquefaction results for a single earthquake scenario and mapped region and (2) describe the format of the results that were provided for risk calculations.

5.1 Example Results

The earthquake scenario for which example results are provided is No. 5 in Wang et al. (2023). It is an M = 8.0 event that involves rupture of the Ft. Tejon segment of the San Andreas Fault and the Garlock Fault, as shown in Figure 5.1. The area for which geo-hazards results are illustrated for this scenario is shown in Figure 5.2, which is located just south of the fault segment intersection and covers an area of about 3,920 km^2 (approx. 39.2 million grid cells). The geologic map (top right) highlights the young alluvium units considered for liquefaction assessments and the older geologic units considered for landslide assessments. The slope map (bottom right) has a spatial resolution of 10 m with slope angles ranging from 0° to 82°. Figure 5.3 shows a subregion map to illustrate the controlling ground motions considered for this scenario in the geo-hazards study area. The contour maps show values of PGA up to 1.6 g and PGV up to 170 cm/s for this earthquake magnitude of **M** = 8.0.

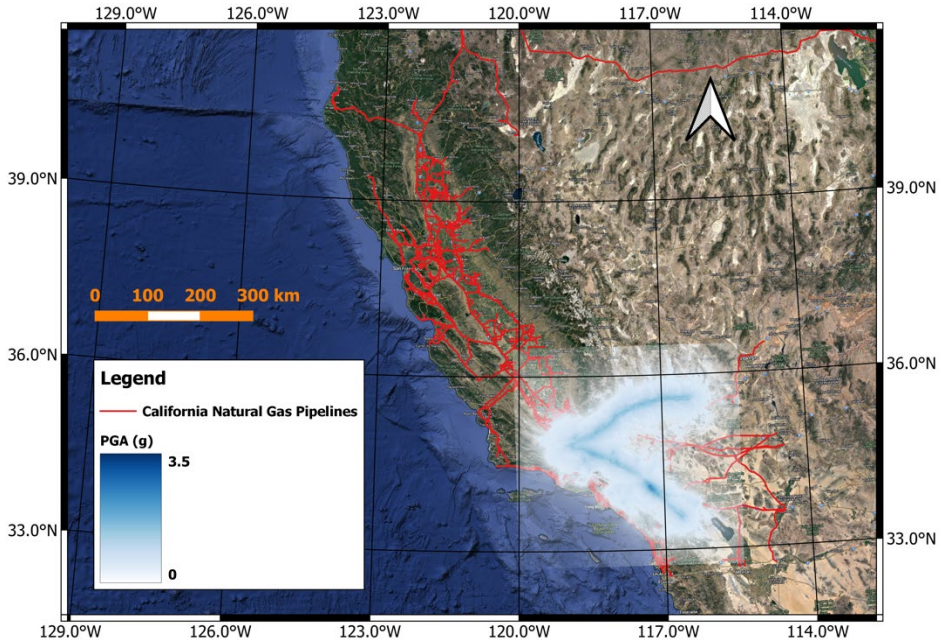

Figure 5.1. Rupture segment for Scenario 5.

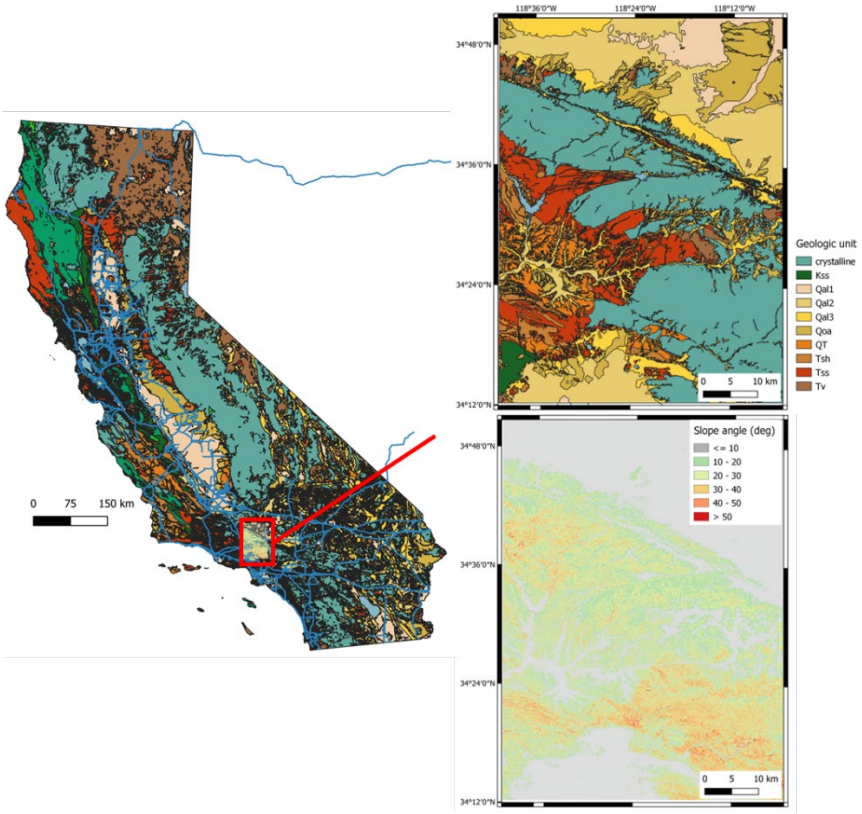

Figure 5.2. Region for which geo-hazards results are illustrated. Left – vicinity map, top right – subregion geology map, bottom right – subregion slope map.

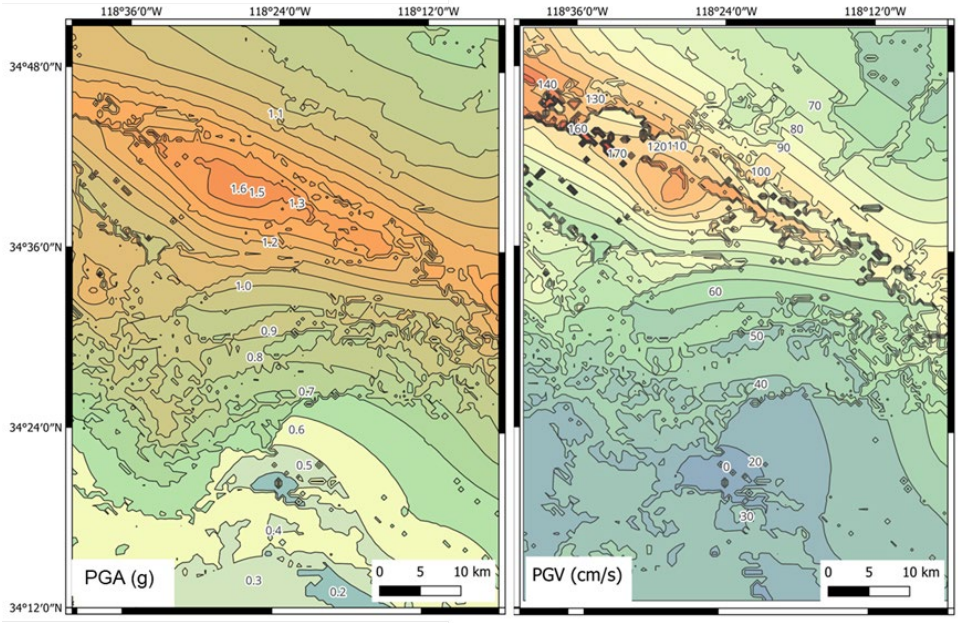

Figure 5.3. Earthquake ground motions, PGA (g) and PGV (cm/s), from scenario No. 5 for the landslide analysis including

Figure 5.4 shows the resulting landslide displacements computed for individual 10-m cells, as described in Chapter 3, and Figure 5.5 displays the resulting segmented landslide zone polygons. We examine the density of landslide zone polygons for two subregions (Zones 1 and 2) that are predominantly associated with the crystalline and Tss geologic units. Zone 1 shows a higher density of landslide zone polygons than Zone 2 even though the slopes in Zone 2 appear to be steeper. This result is due to the ground motion intensity being relatively larger in Zone 1 compared to Zone 2 (Figure 5.3).

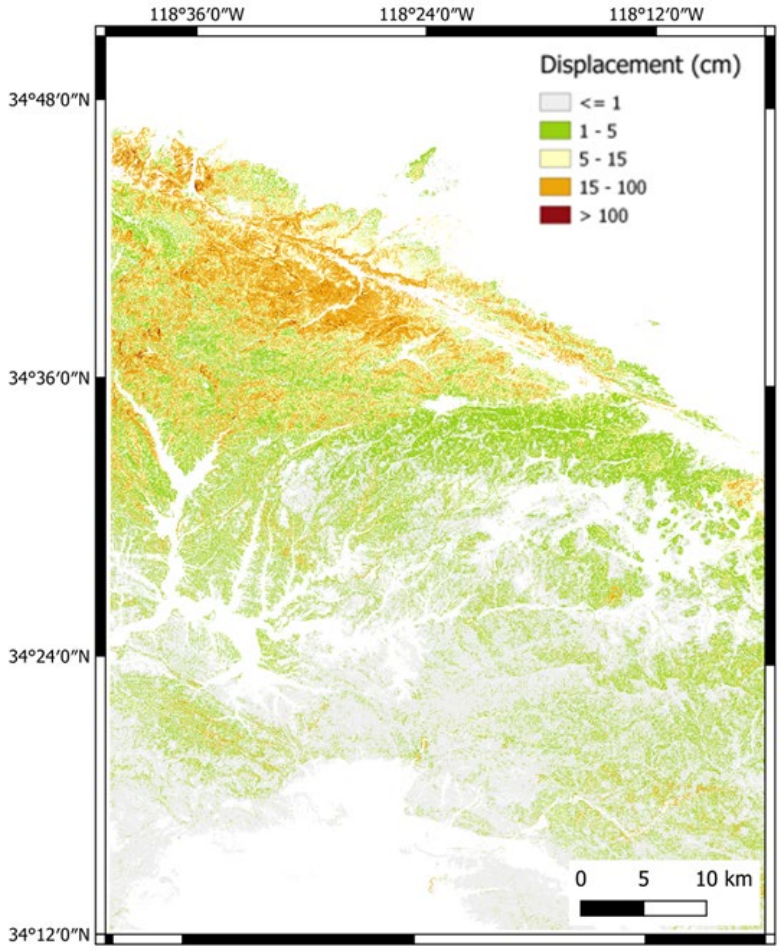

Figure 5.4. Cell-based landslide displacement results for earthquake scenario No. 5.

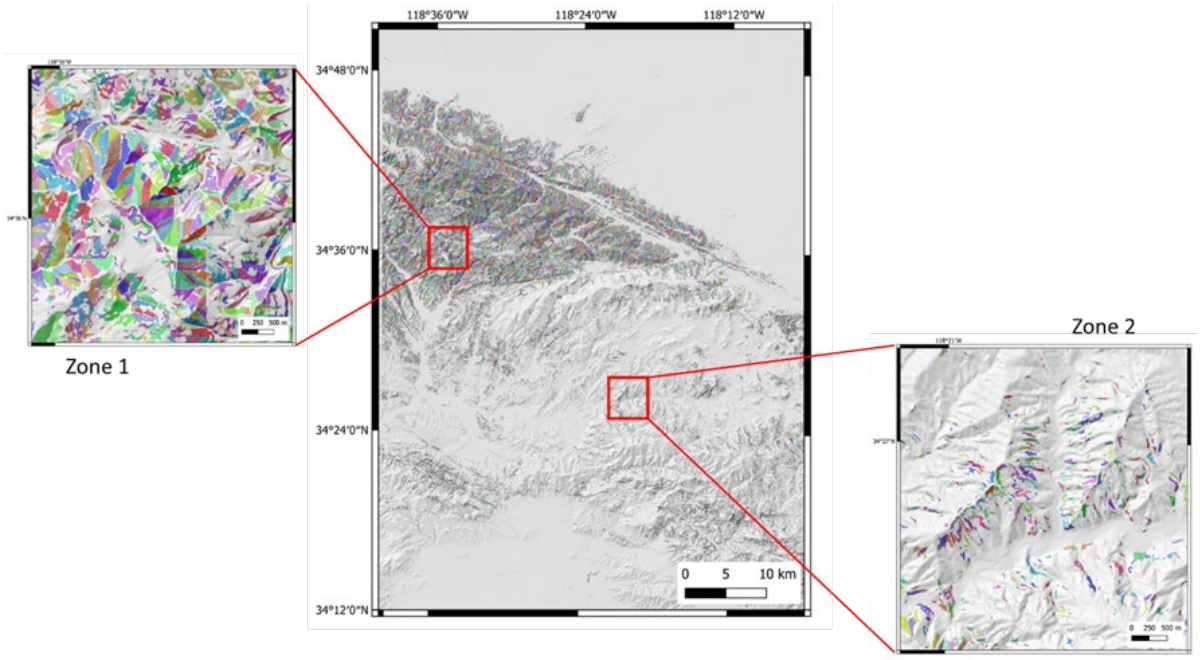

Figure 5.5. Map of segmented landslide zone polygons highlighting spatial distribution of predicted landslides

Figure 5.6 presents the regions susceptible to liquefaction as determined from the surficial geological units. In this example, the susceptible units include young quaternary alluvium (Qal1, Qal2, Qal3, Qoa, and Qi) and artificial fill (af) units. Figure 5.7 shows the mean displacements induced by liquefaction and Figure 5.8 shows the primary mechanism. Overall, in regions where volumetric settlements is the primary mechanism, the mean displacements range from 0.0 to 0.5 meters while in the regions where lateral spread is the dominant mechanism, the mean displacement range from 0.5 to 6.0 meters. The dominant mechanism is primarily controlled by the slope angle, in this example the threshold between lateral spread and volumetric settlements occurs at around 0.20 degrees.

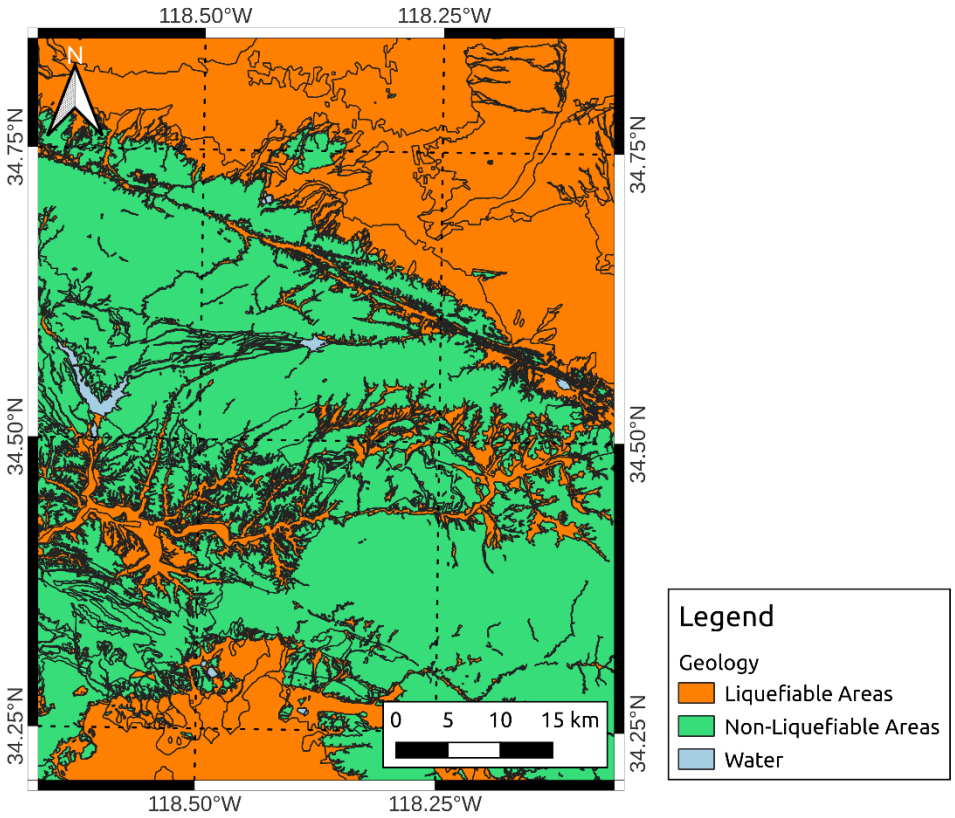

Figure 5.6. Map of liquefiable and non-liquefiable zones based on geology

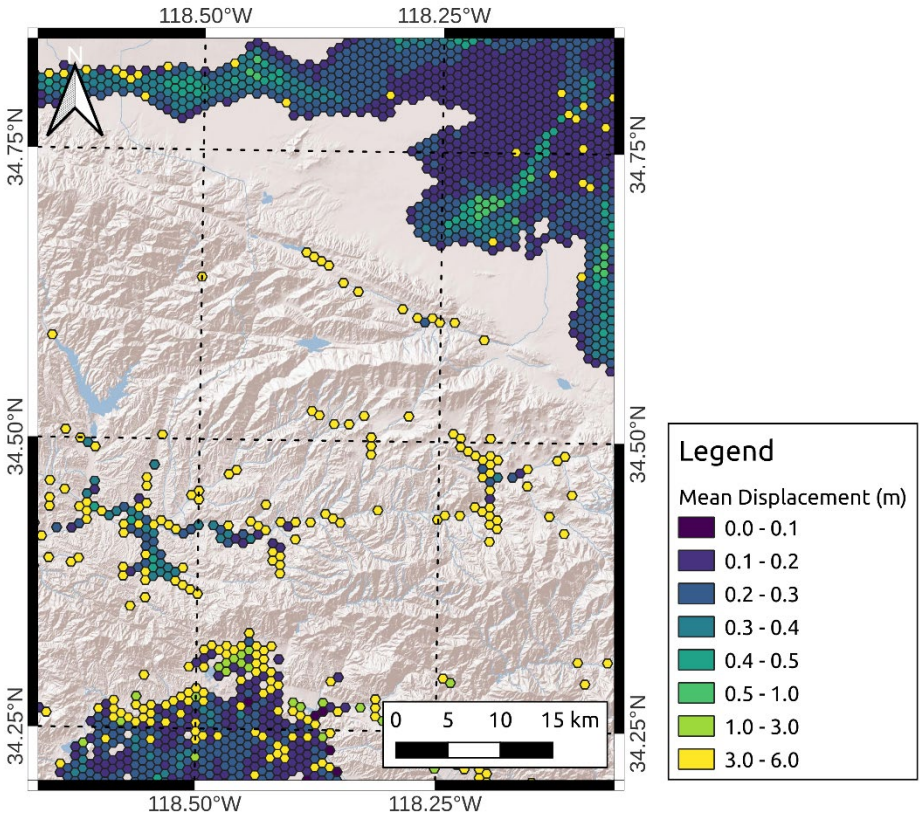

Figure 5.7. Map of mean liquefaction mean displacement results for earthquake scenario No. 5

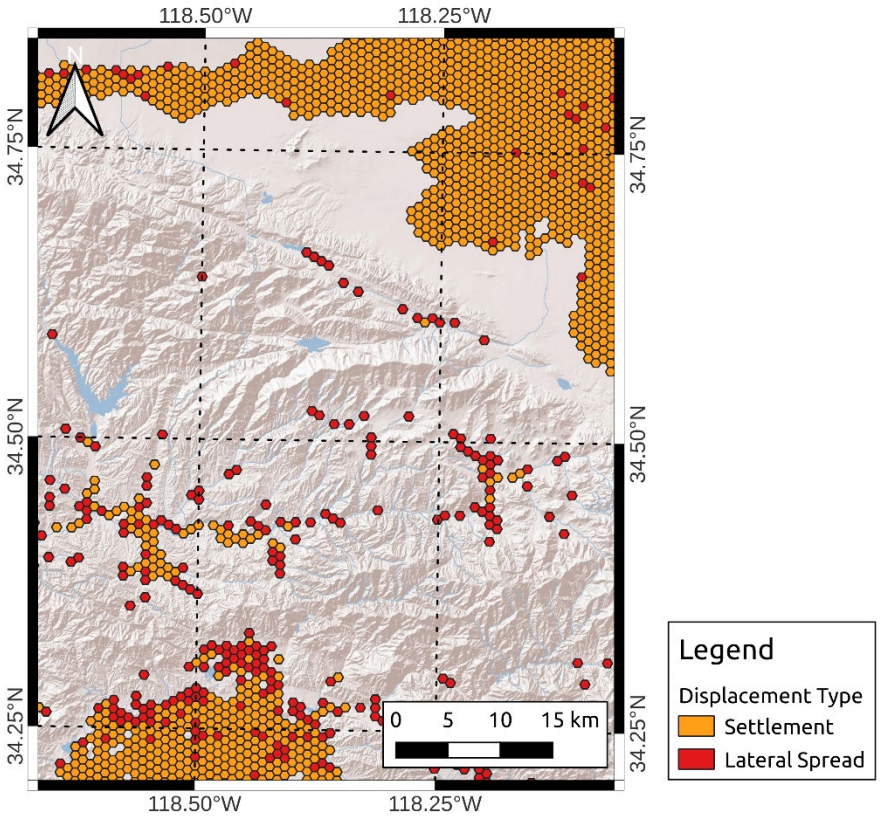

Figure 5.8. Map of zones affected by liquefaction induced settlements versus lateral spread for earthquake scenario No. 5

5.2 Format of Results Provided for Risk Analysis

The final outputs of both the landslide and liquefaction analyses are presented in tabular format compatible with pipeline fragility models.

For the landslide analysis, each generated landslide zone polygon is assigned a unique landslide zone ID and discretized at 10-m grid level to allow for integration with the location of the pipelines. Table 5.1 shows an example of the unique IDs of six landslide zone polygons and the geospatial references (latitude and longitude) of the center of each grid associated with the landslide zone polygon. The probability mass functions for discrete bins of pipeline exposure length, direction of movement, and amount of movement are tabulated for each landslide zone polygon, as shown in Table 5.2, using the unique ID as a cross reference. The 5 bins for pipeline exposure length are 10, 50, 100, 200, and 500 m, the 72 bins for direction are 5° intervals between 0° and 360°, and the 5 bins for landslide movement are 0 - 30, 150 - 300, 300 - 600, 600 - 900, and > 900 cm.

Table 5.1. Locations of landslide zone polygons discretized into 10-m grids

Landslide Zone ID	Latitude	Longitude
1	35.063683	-118.330775
1	35.063593	-118.330774
1	35.063594	-118.330664
1	35.063503	-118.330772
1	35.063504	-118.330662
1	35.063414	-118.330661
2	35.053908	-118.334235
2	35.053909	-118.334125
3	35.039083	-118.377955
3	35.039084	-118.377845
3	35.039085	-118.377736
4	35.032635	-118.389905
4	35.032545	-118.389903
5	35.020144	-118.378295
5	35.020054	-118.378293
6	35.018843	-118.373779
6	35.018750	-118.373997
6	35.018751	-118.373887
6	35.018753	-118.373778
6	35.018659	-118.374105
6	35.018660	-118.373995
6	35.018661	-118.373886

Table 5.2. Landslide zone polygons and probability mass functions of pipeline exposure length, landslide direction and amount of movement.

Landslide Zone ID	PMF of pipeline exposure length	PMF of direction	PMF of movement
1	[0.032 0.968 0. 0. 0.]	[0. 0. 0. 0. 0. 0. 0. 0. 0. 0. 0. 0. 0. 0. 0.167 0. 0.5 0.333 0. 0. 0. 0. 0. 0. 0. 0. 0. 0. 0. 0. 0. 0. 0. 0. 0. 0. 0. 0. 0. 0. 0. 0. 0. 0. 0. 0. 0. 0. 0. 0. 0. 0. 0. 0. 0. 0. 0. 0. 0. 0. 0. 0. 0. 0. 0. 0. 0. 0. 0. 0. 0. 0.]	[0.483 0.256 0.097 0.068 0.053 0.045]
2	[0.208 0.792 0. 0. 0.]	[0. 0. 0. 0. 0. 1. 0. 0. 0. 0. 0. 0. 0. 0. 0. 0. 0. 0. 0. 0. 0. 0. 0. 0. 0. 0. 0. 0. 0. 0. 0. 0. 0. 0. 0. 0. 0. 0. 0. 0. 0. 0. 0. 0. 0. 0. 0. 0. 0. 0. 0. 0. 0. 0. 0. 0. 0. 0. 0. 0. 0. 0. 0. 0. 0. 0. 0. 0. 0. 0. 0. 0.]	[0.490 0.233 0.102 0.072 0.056 0.047]
3	[0.092 0.908 0. 0. 0.]	[0. 0. 0. 0. 0. 0. 0. 0. 0. 0. 0. 0. 0. 0. 0. 0. 0. 0. 0. 0. 0. 0. 0. 0. 0. 0. 0. 0. 0. 0. 0. 0. 0. 0. 0. 0. 0. 0. 0. 0. 0. 0. 0. 0. 0. 0. 0. 0. 0. 0. 0. 0. 0. 0. 0. 0. 0. 0. 0. 0. 0. 0. 0. 0. 0. 0.333 0.667 0. 0. 0. 0. 0.]	[0.483 0.216 0.111 0.078 0.061 0.051]
4	[0.208 0.792 0. 0. 0.]	[0. 0. 0. 0. 0. 0. 0. 0. 0. 0. 0. 0. 0. 0. 0. 0. 0. 0. 0.5 0.5 0. 0. 0. 0. 0. 0. 0. 0. 0. 0. 0. 0. 0. 0. 0. 0. 0. 0. 0. 0. 0. 0. 0. 0. 0. 0. 0. 0. 0. 0. 0. 0. 0. 0. 0. 0. 0. 0. 0. 0. 0. 0. 0. 0. 0. 0. 0. 0. 0. 0. 0. 0.]	[0.495 0.229 0.102 0.072 0.056 0.047]
5	[0.208 0.792 0. 0. 0.]	[0. 0. 0. 0. 0. 0. 0. 0. 0. 0. 0. 0. 0. 0. 0. 1. 0. 0. 0. 0. 0. 0. 0. 0. 0. 0. 0. 0. 0. 0. 0. 0. 0. 0. 0. 0. 0. 0. 0. 0. 0. 0. 0. 0. 0. 0. 0. 0. 0. 0. 0. 0. 0. 0. 0. 0. 0. 0. 0. 0. 0. 0. 0. 0. 0. 0. 0. 0. 0. 0. 0. 0.]	[0.490 0.238 0.100 0.07 0.055 0.046]
6	[0.028 0.972 0. 0. 0.]	[0. 0. 0. 0. 0. 0. 0. 0. 0. 0. 0. 0. 0. 0. 0. 0. 0. 0. 0. 0. 0. 0. 0. 0.167 0.667 0.167 0. 0. 0. 0. 0. 0. 0. 0. 0. 0. 0. 0. 0. 0. 0. 0. 0. 0. 0. 0. 0. 0. 0. 0. 0. 0. 0. 0. 0. 0. 0. 0. 0. 0. 0. 0. 0. 0. 0. 0. 0. 0. 0. 0. 0. 0.]	[0.464 0.246 0.107 0.075 0.059 0.050]

6 Limitations

In this report, an analysis framework is presented for the estimation of spatially distributed seismic ground failure hazards, consisting of features having particular sizes, as well as amounts and directions of displacement. The framework uses readily available geo-spatial information, and as such can be used without site-specific geotechnical data, which is essential for practical application at a large, regional scale. Uncertainties in the presence of these features and the amounts of displacement are evaluated using a logic tree framework in which parametric and modeling uncertainties are considered.

The work presented here has many substantial innovations, but also limitations that could be overcome with additional research. Some of these limitations are:

1. A limited number of scenario earthquake events was considered, meaning that that scenarios have large magnitudes that are not very representative of hazard controlling conditions at most locations.
2. The shear strength parameters for landslide analysis have not been validated with respect to the levels of landslide risk they provide. Future work could validate, and as needed calibrate, these parameters using seismic or non-seismic case history data.
3. The point-based liquefaction modelling approach using CPT data to predict liquefaction susceptibility and triggering could be validated using spatial observations from past earthquakes where such information is available from post-event reconnaissance. Such work would be useful to evaluate the percentage of an area that is indicated as liquefiable is realistic and if the clustering algorithm is effective in different geological environments.
4. The products provided to the risk team are derived based on general data sources (from Chapter 2) that are available statewide. Modularity in the output is not yet provided, whereby results of site-specific studies could be implemented. Longterm, this should be enabled, so that higher-resolution site-specific information can be utilized to reduce uncertainties.

References

Al Atik L, Gregor N, and Bozorgnia Y (2023) Probabilistic seismic hazard analysis for the state of California, Natural Hazards Risk & Resiliency Research Center B. John Institute for the Risk Sciences.

Adler, R. F., Sapiano, M. R., Huffman, G. J., Wang, J.-J., Gu, G., Bolvin, D., Chiu, L., Schneider, U., Becker, A., Nelkin, E., et al. (2018). The Global Precipitation Climatology Project (GPCP) monthly analysis (new version 2.3) and a review of 2017 global precipitation. Atmosphere, 9(4):138.

Ahdi, S. K., Stewart, J. P., Ancheta, T. D., Kwak, D. Y., and Mitra, D. (2017). Development of vs profile database and proxy-based models for vS,30 prediction in the Pacific Northwest region of North America. Bulletin of the Seismological Society of America, 107(4):1781–1801.

Allen, T., Wald, D., Hotovec, A., Lin, K., Earle, P., and Marano, K. (2008). An atlas of shakemaps for selected global earthquakes. Technical Report 1236, United States Geological Survey.

Allstadt, K. E., Thompson, E. M., Jibson, R. W., Wald, D. J., Hearne, M., Hunter, E. J., Fee, J., Schovanec, H., Slosky, D., and Haynie, K. L. (2021). The US Geological Survey ground failure product: Near-real-time estimates of earthquake-triggered landslides and liquefaction. Earthquake Spectra

Alvioli, M., Guzzetti, F., & Marchesini, I. (2020). Parameter-free delineation of slope units and terrain subdivision of Italy. Geomorphology, 358, 107124. doi: 10.1016/j.geomorph.2020.107124

Alvioli, M., Marchesini, I., Reichenbach, P., Rossi, M., Ardizzone, F., Fiorucci, F., & Guzzetti, F. (2016). Automatic delineation of geomorphological slope units with r.slopeunits v1.0 and their optimization for landslide susceptibility modeling. Geoscientific Model Development, 9(11), 3975-3991. doi: 10.5194/gmd-9-3975-2016

Anderson, J. G. and Brune, J. N. (1999). Probabilistic seismic hazard analysis without the ergodic assumption. Seismological Research Letters, 70(1):19–28.

Baise, L. G., Higgins, R. B., and Brankman, C. M. (2006). Liquefaction hazard mapping—statistical and spatial characterization of susceptible units. Journal of Geotechnical and Geoenvironmental Engineering, 132(6):705–715.

Baker, JW, Bradley BA and Stafford PJ. 2021. Seismic Hazard and Risk Analysis. Cambridge University Press, Cambridge, England.

Befus, K., Barnard, P. L., Hoover, D. J., Hart, J. F., and Voss, C. I. (2020). Increasing threat of coastal groundwater hazards from sea-level rise in california. Nature Climate Change, 10(10):946–952.

Beyzaei, C. Z., Bray, J. D., Cubrinovski, M., Bastin, S., Stringer, M., Jacka, M., van Ballegooy, S., Riemer, M., and Wentz, R. (2020). Characterization of silty soil thin layering and groundwater conditions for liquefaction assessment. Canadian Geotechnical Journal, 57(2):263–276.

Blake TF, Hollingsworth RA, Stewart JP, editors (2002). Recommended procedures for implementation of DMG Special Publication 117 Guidelines for analyzing and mitigating landslide hazards in California, Southern California Earthquake Center, University of Southern California, Los Angeles, California, 130 pgs.

Boore, D. M., Stewart, J. P., Seyhan, E., and Atkinson, G. M. (2014). NGA-West2 equations for predicting PGA, PGV, and 5% damped PSA for shallow crustal earthquakes. Earthquake Spectra, 30(3):1057–1085.

Boulanger, R. W., & Idriss, I. M. (2016). CPT-based liquefaction triggering procedure. Journal of Geotechnical and Geoenvironmental Engineering, 142(2), 04015065.

Brandenberg, S. J., Wang, P., Nweke, C. C., Hudson, K., Mazzoni, S., Bozorgnia, Y., Hudnut, K. W., Davis, C. A., Ahdi, S. K., Zareian, F., et al. (2019). Preliminary report on engineering and geological effects of the July 2019 Ridgecrest earthquake sequence. Technical report, Geotechnical Extreme Event Reconnaissance Association.

Bray, J. D., Sancio, R. B., Kammerer, A. M., Merry, S., Rodriquez-Marek, A., Khazai, B., Chang, S., Hausler, E., Dreger, D., Perkins, W., and Nykamp, M. (2001). Some observations of geotechnical aspects of the February 28, 2001, Nisqually earthquake in Olympia, South Seattle, and Tacoma, Washington. Technical report.

Bray, J., Cubrinovski, M., Zupan, J., and Taylor, M. (2014). Liquefaction effects on buildings in the central business district of Christchurch. Earthquake Spectra, 30(1):85–109.

Bullock, Z., Zimmaro, P., Lavrentiadis, G., Wang, P., Ojomo, O., Asimaki, D., Rathje, E. M., & Stewart, J. P. (2023). A latent Gaussian process model for the spatial distribution of liquefaction manifestation. Earthquake Spectra, 39(2): 1189-1213.

California Water Board. (2020). Groundwater Ambient Monitoring and Assessment Program (GAMA). Accessed at: https://gamagroundwater.waterboards.ca.gov/gama/datadownload. Last accessed: March 15th 2020.

Campbell, K. W. and Bozorgnia, Y. (2014). NGA-West2 ground motion model for the average horizontal components of PGA, PGV, and 5% damped linear acceleration response spectra. Earthquake Spectra, 30(3):1087–1115.

Cao, Z., Hou, L., Xu, H., and Yuan, X. (2010). Distribution and characteristics of gravelly soil liquefaction in the Wenchuan m s 8.0 earthquake. Earthquake Engineering and Engineering Vibration, 9(2):167–175.

Casella, G. and Berger, R. L. (2021). Statistical inference. Cengage Learning.

Cetin, K. O., Bilge, H. T., Wu, J., Kammerer, A. M., & Seed, R. B. (2009). Probabilistic model for the assessment of cyclically induced reconsolidation (volumetric) settlements. Journal of Geotechnical and Geoenvironmental Engineering, 135(3), 387-398.

Cetin, K. O., Seed, R. B., Kayen, R. E., Moss, R. E., Bilge, H. T., Ilgac, M., and Chowdhury, K. (2018). SPT-based probabilistic and deterministic assessment of seismic soil liquefaction triggering hazard. Soil Dynamics and Earthquake Engineering, 115:698–709.

Chiles, J.-P. and Delfiner, P. (2009). Geostatistics: modeling spatial uncertainty, volume 497. John Wiley & Sons.

Chleborad, A. F. and Schuster, R. L. (1998). Ground failure associated with the Puget Sound region earthquakes of April 13, 1949, and April 29, 1965. Assessing earthquake hazards and reducing risk in the Pacific Northwest: US Geological Survey Professional Paper, 1560:373–440.

Chu, D. B., Stewart, J. P., Lee, S., Tsai, J.-S., Lin, P., Chu, B., Seed, R. B., Hsu, S., Yu, M., and Wang, M. C. (2004). Documentation of soil conditions at liquefaction and non- liquefaction sites from 1999 Chi–Chi (Taiwan) earthquake. Soil Dynamics and Earthquake Engineering, 24(9-10):647– 657.

Cubrinovski, M., Rhodes, A., Ntritsos, N., and Van Ballegooy, S. (2019). System response of liquefiable deposits. Soil Dynamics and Earthquake Engineering, 124:212–229.

Daly, C., Taylor, G., and Gibson, W. (1997). The PRISM approach to mapping precipitation and temperature. In Proc., 10th AMS Conf. on Applied Climatology, pages 20–23.

Detweiler ST and Wein AM 2017. The HayWired earthquake scenario: U.S. Geological Survey Scientific Investigations Report 2017–5013A-H. Version 1.2: December 2018 https://doi.org/10.3133/sir20175013v1

Dreyfus DK, Rathje EM and Jibson RW. 2013. The Influence of Different Simplified Sliding-Block Models and Input Parameters on Regional Predictions of Seismic Landslides Triggered by the Northridge Earthquake. Engineering Geology 163 (August): 41–54. https://doi.org/10.1016/j.enggeo.2013.05.015.

Dudley, R. (1967). The sizes of compact subsets of Hilbert space and continuity of gaussian processes. Journal of Functional Analysis, 1(3):290–330.

Fan Y, Li H, and Miguez-Macho G. (2013). Global patterns of groundwater table depth. *Science*, 339(6122), 940-943.

Fanelli G, Salciarini D, and Tamagnini C. 2015. Reliable Soil Property Maps Over Large Areas: A Case Study in Central Italy. Environmental & Engineering Geoscience, no. October 2016: 1078-7275.EEG – 1709. https://doi.org/10.2113/eeg-1709.

Foster, K. M., Bradley, B. A., McGann, C. R., and Wotherspoon, L. M. (2019). A VS,30 map for New Zealand based on geologic and terrain proxy variables and field measurements. Earthquake Spectra, 35(4):1865–1897.

Geyin, M., Maurer, B., Bradley, B. A., Green, R., and van Ballegooy, S. (2020). Cpt-based liquefaction case histories resulting from the 2010-2016 canterbury, new Zealand, earthquakes: A curated digital dataset (version 2).

Greenfield, M. W. and Grant, A. (2020). Probabilistic regional- scale liquefaction triggering modeling using 3D gaussian processes. Soil Dynamics and Earthquake Engineering, 134:106159.

Guzzetti F, Reichenbach P, Cardinali M, Galli M and Ardizzone F. 2005. Probabilistic Landslide Hazard Assessment at the Basin Scale. Geomorphology Issues 1-4, Vol. 72, pg 272-299. 10.1016/j.geomorph.2005.06.002

Hamada, M., Isoyama, R., and Wakamatsu, K. (1996). Liquefaction-induced ground displacement and its related damage to lifeline facilities. Soils and foundations, 36:81–97.

Holzer, T. L., Bennett, M. J., Noce, T. E., Padovani, A. C., and Tinsley III, J. C. (2006). Liquefaction hazard mapping with lpi in the greater oakland, california, area. Earthquake Spectra, 22(3):693–708.

Holzer, T. L., Noce, T. E., Bennett, M. J., Tinsley III, J. C., and Rosenberg, L. I. (2005). Liquefaction at oceano, california, during the 2003 san simeon earthquake. Bulletin of the Seismological Society of America, 95(6):2396–2411.

Isaaks, E. H. and Srivastava, M. R. (1989). Applied Geostatistics. Oxford University Press.

Iwasaki, T., Tatsuoka, F., Tokida, K.-i., and Yasuda, S. (1978). A practical method for assessing soil liquefaction potential based on case studies at various sites in japan. In Proc. Second Int. Conf. Microzonation Safer Construction Research Application, 1978, volume 2, pages 885–896.

Jibson RW and Michael JA. 2009. Maps Showing Seismic Landslide Hazards in Anchorage, Alaska: U.S. Geo- Logical Survey Scientific Investigations Map 3077, scale 1:25,000, 11-p. pamphlet. http://pubs. usgs.gov/sim/3077.

Jibson RW. 2007. Regression Models for Estimating Coseismic Landslide Displacement. Engineering Geology 91 (2–4): 209–18. https://doi.org/10.1016/j.enggeo.2007.01.013.

Jibson RW, Harp EL and Michael JA. 2000. A Method for Producing Digital Probabilistic Seismic Landslide Hazard Maps. Engineering Geology. Vol. 58. https://doi.org/10.1016/S0013-7952(00)00039-9.

Journel, A. G. and Huijbregts, C. J. (1978). Mining Geostatistics, volume 600. Academic press.

Juang, C. H., Ching, J., Wang, L., Khoshnevisan, S., & Ku, C. S. (2013). Simplified procedure for estimation of liquefaction-induced settlement and site-specific probabilistic settlement exceedance curve using cone penetration test (CPT). Canadian Geotechnical Journal, 50(10), 1055-1066.

Keefer DK. 2013. Landslides Generated by Earthquakes: Immediate and Long-Term Effects. In Treatise on Geomorphology, 5:250–66. https://doi.org/10.1016/B978-0-12-374739-6.00091-9.

Kubota, T., Shige, S., Hashizume, H., Aonashi, K., Takahashi, N., Seto, S., Hirose, M., Takayabu, Y. N., Ushio, T., Nakagawa, K., et al. (2007). Global precipitation map using satellite-borne microwave radiometers by the GSMaP project: Production and validation. IEEE Transactions on Geoscience and Remote Sensing, 45(7):2259–2275.

Kwok, O. L. A., Stewart, J. P., Kwak, D. Y., and Sun, P.- L. (2018). Taiwan-specific model forVS,30 prediction considering between-proxy correlations. Earthquake Spectra, 34(4):1973–1993.

Lavrentiadis, G., Abrahamson, N. A., Nicolas, K. M., Bozorgnia, Y., Goulet, C. A., Babîc, A., Macedo, J., Dolšek, M., Gregor, N., Kottke, A. R., et al. (2022). Overview and introduction to

development of non-ergodic earthquake ground-motion models. Bulletin of Earthquake Engineering, pages 1–30.

Lewis, M., Arango, I., Kimball, J., and Ross, T. (1999). Liquefaction resistance of old sand deposits. In Proc., 11th Panamerican Conf. on Soil Mechanics and Geotechnical Engineering, pages 821–829. ABMS San Paulo, Brazil.

Lilliefors, H. W. (1967). On the kolmogorov-smirnov test for normality with mean and variance unknown. Journal of the American statistical Association, 62(318):399–402.

Malamud BD, Turcotte DL, Guzzetti F and Reichenbach P. 2004. Landslide Inventories and their Statistical Properties. Earth Surface Processes and Landforms, 29(6), 687–711. https://doi.org/10.1002/esp.1064

Markhvida, M., Ceferino, L., and Baker, J. W. (2018). Modeling spatially correlated spectral accelerations at multiple periods using principal component analysis and geostatistics. Earthquake Engineering & Structural Dynamics, 47(5):1107–1123.

Maurer, B. W. (2017). Assessing liquefaction susceptibility using the CPT soil behavior type index. In Proc. 3rd Intern. Conf. on Performance-Based Design in Earthquake Geotechnical Engineering (PBDIII).

Maurer BW, Green RA, Cubrinovski M, Bradley B. Evaluation of the liquefaction potential index for assessing liquefaction hazard in Christchurch, New Zealand. *J Geotech Geoenviron Eng* 2014; **140**(7), 04014032.

Maurer BW, Green RA, Cubrinovski M, Bradley B. Moving towards an improved index for assessing liquefaction hazard: lessons from historical data. *Soils and Foundations* 2015a; *In Press,* doi:10.1016/j.sandf.2015.06.010*.*

Maurer BW, Green RA, Cubrinovski M, Bradley B. Assessment of CPT-based methods for liquefaction evaluation in a liquefaction potential index (LPI) framework. *Geotechnique* 2015b; **65**(5): 328-336.

Maurer BW, Green RA, Cubrinovski M, Bradley B. Fines-content effects on liquefaction hazard evaluation for infrastructure during the 2010-2011 Canterbury, New Zealand earthquake sequence. *Soil Dynamics and Earthquake Engineering* 2015c; **76***:* 58-68.

McCrink, T. P., Pridmore, C. L., Tinsley III, J. C., Sickler, R. R., Brandenberg, S. J., and Stewart, J. P. (2011). Liquefaction and other ground failures in imperial county, california, from the april 4, 2010, el mayor-cucapah earthquake. Technical Report, US Geological Survey.

Miller AC and Rice TR. 1983. Discrete Approximations of Probability Distributions. Management Science, 29, 352-362.

Moss, R. E., Seed, R. B., Kayen, R. E., Stewart, J. P., Der Kiureghian, A., & Cetin, K. O. (2006). CPT-based probabilistic and deterministic assessment of in situ seismic soil liquefaction potential. Journal of Geotechnical and Geoenvironmental Engineering, 132(8), 1032-1051.

Moss, R. E., Thompson, E. M., Scott Kieffer, D., Tiwari, B., Hashash, Y. M., Acharya, I., Adhikari, B. R., Asimaki, D., Clahan, K. B., Collins, B. D., et al. (2015). Geotechnical effects of

the 2015 magnitude 7.8 Gorkha, Nepal, earthquake and aftershocks. Seismological Research Letters, 86(6):1514–1523.

Moss, R., Seed, R. B., Kayen, R. E., Stewart, J. P., Der Kiureghian, A., and Cetin, K. O. (2006). Cpt-based probabilistic and deterministic assessment of in situ seismic soil liquefaction potential. Journal of Geotechnical and Geoenvironmental Engineering, 132(8):1032–1051.

Nichols MD, Davis G and Young D. 1997. Seismic Hazard Zone Report for the Oat Mountain 7.5-Minute Quadrangle, Los Angeles County, California. Department of Conservation – Division of Mines and Geology. SHZR 05.

Obermeier, S. F., Jacobson, R. B., Smoot, J. P., Weems, R. E., Gohn, G. S., Monroe, J. E., and Powars, D. S. (1990). Earthquake-induced liquefaction features in the coastal setting of south carolina and in the fluvial setting of the New Madrid seismic zone. Technical report.

Ojomo, O., Rathje, E. M., Bullock, Z., Wang, P., Asimaki, D., Stewart, J. P., and Zimmaro, P. (2022). Regional Earthquake-Induced Landslide Mapping for California using a Data-Informed Probabilistic Approach. In Proceedings of the 12th National Conference on Earthquake Engineering. Earthquake Engineering Research Institute, Salt Lake City, UT, 2022.

Petersen, M. D., Shumway, A. M., Powers, P. M., Mueller, C. S., Moschetti, M. P., Frankel, A. D., Rezaeian, S., McNamara, D. E., Luco, N., Boyd, O. S., and Rukstales, K. (2020). The 2018 update of the us national seismic hazard model: Overview of model and implications. Earthquake Spectra, 36(1):5–41.

Quigley, M. C., Bastin, S., and Bradley, B. A. (2013). Recurrent liquefaction in Christchurch, New Zealand, during the Canterbury earthquake sequence. Geology, 41(4):419–422.

Rashidian, V. and Baise, L. G. (2020). Regional efficacy of a global geospatial liquefaction model. Engineering Geology, 272:105644.

Rathje EM and Saygili G. 2008. Probabilistic Seismic Hazard Analysis for the Sliding Displacement of Slopes: Scalar and Vector Approaches. Journal of Geotechnical and Geoenvironmental Engineering, ASCE, 134(6), 804-814.

Rathje EM and Saygili G. 2009. Probabilistic Assessment of Earthquake-Induced Sliding Displacements of Natural Slopes. Bulletin of the New Zealand Society of Earthquake Engineering, 42, 18-27.

Robertson, P. K. (2009). Interpretation of cone penetration tests—a unified approach. Canadian Geotechnical Journal, 46(11), 1337-1355.

Robertson, P. K., & Wride, C. E. (1998). Evaluating cyclic liquefaction potential using the cone penetration test. Canadian Geotechnical Journal, 35(3), 442-459.

Schmitt, R., Tanyas, H., Nowicki Jessee, M. A., Zhu, J., Biegel, K. M., Allstadt, K. E., Jibson, R. W., Thompson, E. M., van Westen, C. J., Sato, H. P., Wald, D. J., Godt, J. W., Gorum, T., Xu, C., Rathje, E. M., and Knudsen, K. L. (2017). An open repository of earthquake-triggered ground-failure inventories (ver 3.0, september 2020).

Skrondal, A. and Rabe-Hesketh, S. (2007). Latent variable modelling: a survey. Scandinavian Journal of Statistics, 34(4):712–745.

Stewart, J. P., Asimaki, D., Rathje, E. M., Bullock, Z., Ojomo, O., Wang, P., and Zimmaro, P. (2022). Framework for Regional Analysis of Spatially Distributed Ground Failure Displacement Hazards. In Proceedings of the 12th National Conference on Earthquake Engineering. Earthquake Engineering Research Institute, Salt Lake City, UT, 2022.

Stewart, J. P., Seed, R. B., and Bray, J. D. (1996). Incidents of ground failure from the 1994 Northridge earthquake. Bulletin of the Seismological Society of America, 86(1B):S300–S318.

Thompson, E., Wald, D. J., and Worden, C. (2014). A VS,30 map for California with geologic and topographic constraints. Bulletin of the Seismological Society of America, 104(5):2313–2321.

Tinsley III, J. C., Egan, J. A., Kayen, R. E., and Bennett, M. J. (1998). Liquefaction and associated effects. US Geological Survey professional paper, 1551:287.

USGS (2018). The National Elevation Dataset 10-Meter Resolution Digital Elevation Model. https://www.usgs.gov/the-national-map-data-delivery, last accessed on 23 February 2023.

USGS (2020). U.S. Geological Survey ShakeMap Version 4.0 http://earthquake.usgs.gov/data/shakemap/ (2020). Last accessed: December 17th, 2021.

USGS. (2020). Table of CPT Data, available at: https://earthquake.usgs.gov/research/cpt/data/table/ (last accessed on July 15, 2020).

Van Ballegooy, S., Malan, P., Lacrosse, V., Jacka, M., Cubrinovski, M., Bray, J., O'Rourke, T., Crawford, S., and Cowan, H. (2014). Assessment of liquefaction-induced land damage for residential Christchurch. Earthquake Spectra, 30(1):31–55.

Wald, D. J. and Allen, T. I. (2007). Topographic slope as a proxy for seismic site conditions and amplification. Bulletin of the Seismological Society of America, 97(5):1379–1395.

Wang P, Al Atik L, Gregor N, Kottke AR, Kuehn N, Liu Z, Walling MA, Zimmaro P, Bozorgnia Y, Brandenberg SJ, Stewart JP (2023). Hazard-Consistent Scenario-Based Correlated Ground Motions for California Gas Pipeline Infrastructure, Draft Report. Garrick Institute for Risk Sciences, UCLA.

Wang P, Liu Z, Brandenberg SJ, Zimmaro P, Stewart JP. Regression-based event selection for hazard-consistent seismic risk assessment. Proceedings of the 12th National Conference in Earthquake Engineering, Earthquake Engineering Research Institute, Salt Lake City, UT. 2022.

Wang, C., Chen, Q., Shen, M., and Juang, C. H. (2017). On the spatial variability of CPT-based geotechnical parameters for regional liquefaction evaluation. Soil Dynamics and Earthquake Engineering, 95:153–166

Westerhoff, R., White, P., and Miguez-Macho, G. (2018). Application of an improved global-scale groundwater model for water table estimation across new Zealand. Hydrology and Earth System Sciences, 22(12):6449–6472.

Wills CJ and Clahan KB. 2006. Developing a Map of Geologically Defined Site-Condition Categories for California. Bulletin of the Seismological Society of America, 96(4A), 1483–1501. https://doi.org/10.1785/0120050179

Wills CJ, Gutierrez CI, Perez FG, and Branum DM. 2015. A Next Generation V_S30 Map for California Based on Geology and Topography. Bulletin of the Seismological Society of America. 105 (6): 3083–3091, https://doi.org/10.1785/0120150105.

Youd TL and 20 other authors (2001). Liquefaction resistance of soils: summary report from the 1996 NCEER and 1998 NCEER/NSF workshops on evaluation of liquefaction resistance of soils. *J. Geotech. & Geoenv. Engrg.*, 27(10), 817-833.

Youd, T. L. and Hoose, S. N. (1978). Historic ground failures in Northern California triggered by earthquakes, volume 993. US Government Printing Office.

Youd, T. L. and Perkins, D. M. (1978). Mapping liquefaction- induced ground failure potential. Journal of the Soil Mechanics and Foundations Division, 104(4):433–446.

Youd, T. L., Hansen, C. M., & Bartlett, S. F. (2002). Revised multilinear regression equations for prediction of lateral spread displacement. Journal of Geotechnical and Geoenvironmental Engineering, 128(12), 1007-1017.

Zhang, G., Robertson, P. K., & Brachman, R. W. (2002). Estimating liquefaction-induced ground settlements from CPT for level ground. Canadian Geotechnical Journal, 39(5), 1168-1180.

Zhang, G., Robertson, P. K., & Brachman, R. W. I. (2004). Estimating liquefaction-induced lateral displacements using the standard penetration test or cone penetration test. Journal of Geotechnical and Geoenvironmental Engineering, 130(8), 861-871.

Zhu H, Zhang LM, and Xiao T. 2019. Evaluating Stability of Anisotropically Deposited Soil Slopes. Canadian Geotechnical Journal. https://doi.org/10.1139/cgj-2018-0210.

Zhu, J., Baise, L. G., & Thompson, E. M. (2017). An updated geospatial liquefaction model for global application. Bulletin of the Seismological Society of America, 107(3), 1365-1385

Zhu, J., Daley, D., Baise, L. G., Thompson, E. M., Wald, D. J., and Knudsen, K. L. (2015). A geospatial liquefaction model for rapid response and loss estimation. Earthquake Spectra, 31(3):1813–1837.

Zimmaro, P., Nweke, C. C., Hernandez, J. L., Hudson, K. S., Hudson, M. B., Ahdi, S. K., Boggs, M. L., Davis, C. A., Goulet, C. A., Brandenberg, S. J., Hudnut, K. W., and Stewart, J. P. (2020). Liquefaction and Related Ground Failure from July 2019 Ridgecrest Earthquake Sequence. Bulletin of the Seismological Society of America, 110(4):1549–1566.

Zimmaro, P., Stewart, J. P., Brandenberg, S. J., Kwak, D. Y., and Jongejan, R. (2019). Multi-hazard system reliability of flood control levees. Soil Dynamics and Earthquake Engineering, 124:345–353.